RIGA TECHNICAL UNIVERSITY

Nikolajs Toropovs

EVALUATION OF HIGH-PERFORMANCE CONCRETE EXPOSED TO ELEVATED TEMPERATURES

Doctoral Thesis

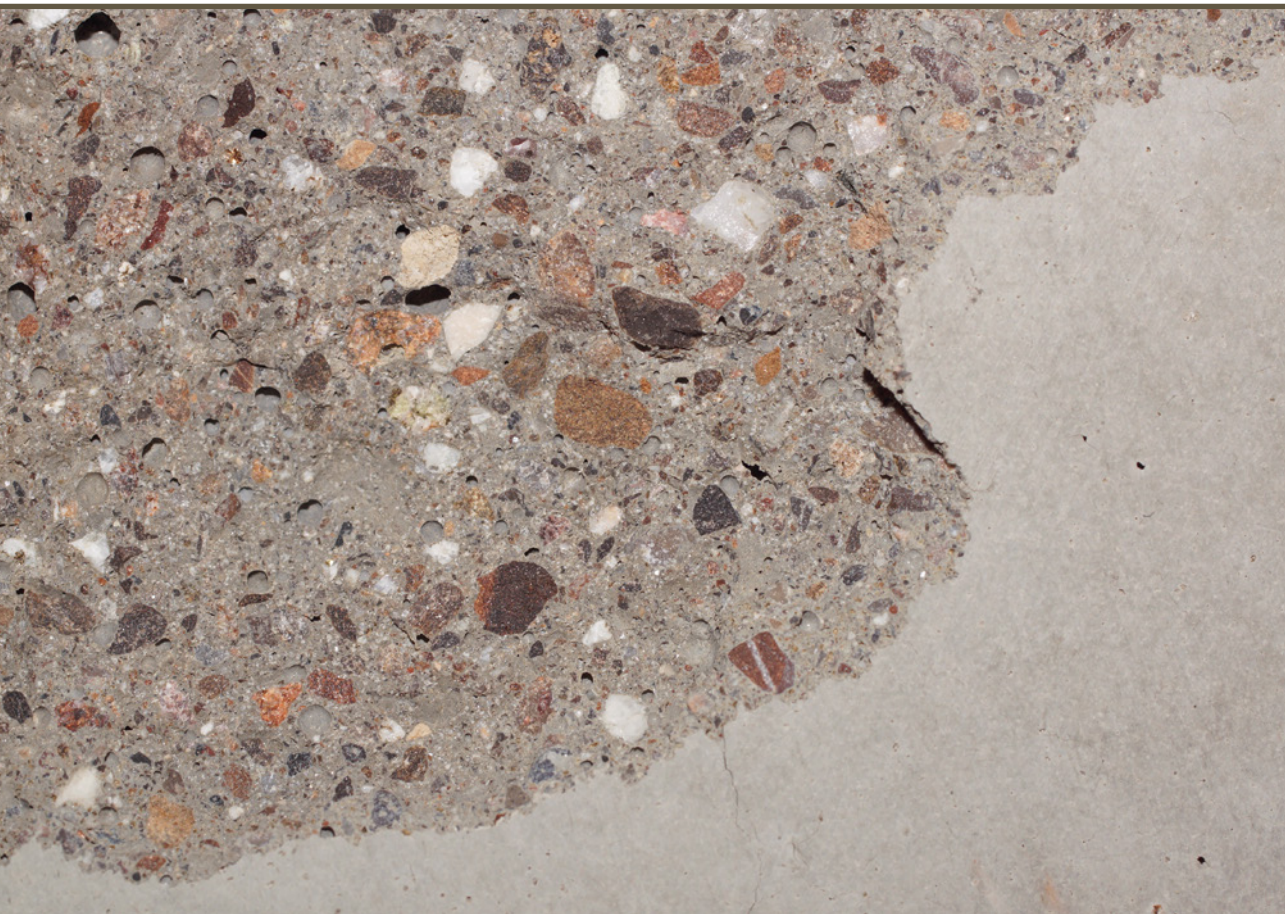

RTU Press
Riga 2026

RIGA TECHNICAL UNIVERSITY
Faculty of Civil and Mechanical Engineering
Institute of Sustainable Building Materials and Engineering Systems

Nikolajs Toropovs
Doctoral student of the Study programme „Civil engineering”

EVALUATION OF HIGH PERFORMANCE CONCRETE EXPOSED TO ELEVATED TEMPERATURES

Doctoral Thesis

Scientific supervisor
Associate Professor Dr. sc. ing
GENĀDIJS ŠAHMENKO

Riga 2026

ANOTĀCIJA

Promocijas darba ietvaros ir apskatīta betona termiskās atslāņošanās problēma. Darba nosaukums ir "Augstas veikstspējas betonu novērtējums pēc augstu temperatūru iedarbes". Promocijas darbs ietver sevī izverstu literatūras apskatu koncentrējoties uz ugunsgrēku vēsturisko apskatu, testēšanas metožu apkopojumu ar ieskatu dažādos uguns slogojuma protokolos. Ir apkopotas pamatteorijas, kas apraksta termiskās noslogošanas mehānismus un betona īpašības pēc augsto temepratūru ietekmes.

Literatūras aprakstam seko darba prakstiskā daļa. Praktiskajā daļā tiek pamatota sastāvu izvēle un vispirms tiek pārbaudīta to nosliece uz termisko atslāņošanos. Tālāk tiek pētītas mehānisko īpašību un mikrostruktūras izmaiņas pēc augstu temperatūru iedarbes. Tiek pētītas paliekošas izmaiņas struktūrā pēc atdzesēšanas līdz istabas temperatūrai.

Viena no darba galvenajām novitātēm ir kompleksie mērījumi reālajā laikā, kombinējot termisko slogojumu ar vienlaicīgiem temperatūras profilu un ūdens tvaika spiediena mērījumiem, papildinot to ar ūdens kustības vizualizāciju izmantojot neitrona radiogrāfiju. Pirmi reizi tika vizualizēta betona termiskā atslāņošanās reāllaikā vienlaicīgi kvalitatīvi novērtējot mitruma migrāciju.

Negraujošās pārbaudes ļauj pētīt betona stāvokli dažādās tā attīstības vai degradācijas stadijās izmantojot fiziski tos pašus paraugus, samazinot mērījumu neprecizitāti kas varētu būt saistīta ar dažādu paraugu izmantošanu un to neviendabību. Četru dažādu negraujošo pārbaužu metožu kombinācija vienotā mērījumu sērijā, pētot betona degradāciju vienas konsekventas matricas ietvaros ļauj izvirzīt teoriju par kopējo dehidratāciju cementa pastā, un iespējamu lokālo hidrotācijas attīstību ITZ (Interfacial Transition Zone) zonā un rukuma izraisītajās mikro plaisās. Lineārās ultraskaņas metodes vizualizē materiāla fiziskos bojājumus un dehidratāciju, kamēr nelineārās ultraskaņas metodes ļauj izvirzīt teoriju par lokālo hidrotāciju iepriekš vajākajās mikrostruktūras vietās. Rezultātus papildina mikro datortomogrāfijas, vizualizējot radiālās plaisas un plaisas ap mazāk blīvām pildvielām.

ANNOTATION

This work explores the problem of explosive thermal spalling of concrete. Title of the work "Evaluation of high performance concrete exposed to elevated temperatures". The Thesis includes a comprehensive review of the literature focusing on the historical review of fires, a summary of testing methods with insight into various fire load protocols. The basic theories describing the mechanisms of thermal loading and the properties of concrete under the influence of high temperatures are summarized. The description of the literature is followed by the practical part of the work. In the practical part, the choice of compositions is justified and their tendency to thermal spalling is first tested. Changes in mechanical properties and microstructure after exposure to high temperatures are further investigated. Permanent changes in structure after cooling to room temperature are studied. One of the main novelties of the work is complex real-time measurements, combining thermal loading with simultaneous temperature profile and water vapor pressure measurements, supplemented by visualization of water movement using neutron radiography. Real-time thermal spalling of concrete and its relationship to moisture migration was visualized for the first time. Non-destructive testing allows the condition of concrete to be studied at different stages of its development or degradation using physically the same samples, reducing measurement inaccuracies that may be associated with the use of different samples and their heterogeneity. The combination of four different non-destructive testing methods in one measurement company, studying the degradation of concrete in one consistent matrix, allows to put forward the theory of general dehydration in cement paste, and possible local development of hydration in the ITZ (Interfacial Transition Zone) zone and shrinkage-induced micro-cracks. Linear ultrasound methods visualize the physical damage and dehydration of the material, while nonlinear ultrasound methods allow the theory of local hydration at previously weakened microstructural sites. The results are complemented by micro-computed tomography imaging of radial cracks and crevices around less dense aggregates.

CONTENTS

This study was partially funded by the Scientific Exchange Program Sciex NMS-CH under the project 12.305 “FRESCO-Fire spalling of High Performance and Ultra-High Performance Concrete”.

Acknowledgments

Slow long walks give you more time to observe and enjoy the nature. To be fancy, I would like to quote FN here: "All truly great thoughts are conceived while walking". And I took my time.

I would like to express my sincere gratitude to my supervisors, who inspired me and led by example with true dedication and enthusiasm: Genādijs Šahmenko, Pietro Lura, Mateusz Wyrzykowski, Michele Griffa and Benedikt Weber.

I am also grateful to reviewers and members of my Promotion Council for their constructive feedback and thoughtful suggestions.

I would like to thank my colleagues and collaborations for being involved in great projects beyond what I could imagine at the start of my Lab expedition as a bachelor student.

This has been a remarkable journey through the decades, shaped by the many people I have met along the way. Thank you, Alex, Aleksandrs, Alessio, Alina, Andrejs, Andreas, Barbara, Dani, Daniele, Davide, Diana, Ellina, Emilie, Fei, Frank, Gabi, Grazia, Guntis, Iuri, Jānis, Köbi, Lauris, Latina, Malene, Marcel, Martin, Martiņš, Nadine, Paulina, Petra, Raphael, Robert, Roman, Rupert, Sarah, Sebi, Sepp, Serena,Vincent, Vitālijs, Walter, Zhangli.

I have had enough time to observe and reflect – an experience that has been a true blessing.

Finally, I would like to thank my family for their constant support.

INTRODUCTION

Through the long history of research, development and application, concrete has become the most used manmade material in the world[1–3]. It has found applications both as a simple road barrier block to organize the traffic and as structural material to reach heights and spans hard to imagine decades ago. Call for concrete with superior strength and durability properties compared to traditional concrete came along with industrial development in second half of 20th century. Concrete has undergone changes to ensure better performance overall and greater specialization to meet requirements in field of application. This involved optimization of grain size distribution, use of fine particles with pozzolanic activity, use of aggregates with certain properties, etc[4]. However, most important was decrease of water to cement ratio and introduction of water reducing admixtures. Water reducing admixtures were introduced in 1930s and affected the concrete industry; however, it was in 1980s, when the new type of polycarboxylate plasticizers led to revolution in concrete properties[5]. Concrete with superior properties compared to Ordinary Concrete (OC) is often called High Performance Concrete (HPC) and the plasticizers that revolutionized the market are referred to as superplasticizers. HPC is characterized by high compressive and tensile strengths, high modulus of elasticity, good durability, low permeability and high resistance to abrasion. By reducing the construction dead weight, fewer raw materials are consumed and slender, elegant constructions with lower embodied energy become possible. Changes in concrete compositions and performance happened gradually, thereby there is no clear single borderline between OC and HPC, variety of applications and availability of raw materials allows co-existence of unlimited mix designs worldwide. Special and at the same time very diverse applications, such as tunnels, high-rise buildings, nuclear power plants, long span bridges, led to high diversity in types of concrete and new challenges that were not in the spotlight years ago. All this allows coexistence of "new" mix designs without running "old" concepts completely out of date. Discussing the significant development in concrete industry over the 20th century, Neville and Aitcin compared it to telecommunication and car industry, as "nevertheless, the changes are nowhere near as revolutionary as the changes in telecommunication and even in motor cars"[6].

It is necessary to ensure long-time durability of structures both from labor efficiency point of view and from sustainable development of society in a world of limited mineral/fossil resources. Manufacturing of cement is responsible for up to 8 – 9 % share of global man produced CO_2[3], reaching 163 million tons of cement products in EU28 countries alone in 2016, with its maximum at 268 million tons in 2007[7]. As for year 2015, 167 million tons of cement were produced in EU28 countries, representing 4% of global production, making EU third largest producer of cement worldwide, after India with its 270 million tons and China dominating the market with 2350 million tons of cement, that corresponds to 51% of global production in 2015[7]. Calcination of limestone and fuel combustion to produce cement, combined, release approximately 1 ton of CO_2 per 1 ton of cement[3].

Despite rapid development of concrete properties and large volume of material produced, emphasizing the importance of concrete to modern society, one of the major limitations to worldwide spread of HPC comes from its performance under fire, namely a poor resistance of HPC when exposed to high temperatures. This is because of the violent damage mode referred to as explosive spalling[4,8]. Explosive spalling at high temperature can lead to gradual loss of protective concrete layer of reinforcement, exposing it to environment, and ultimately to failure

of reinforced structural concrete member. It is important to distinguish spalling as a complex, structure related phenomena, and changes that concrete undergoes at different temperatures as material. The difference is discussed in the following 1.1 and 1.2 chapters of this Thesis, from point of view of the structure and as for material correspondingly.

The more HPC comes in application, the higher the concerns of HPC performance are under fire. With increased use of HPC in high-rise buildings and tunnels it becomes necessary to study the nature of explosive spalling under fire to address those concerns and to find a reliable solution to protect new and existing structures from spalling. The high interest of research and industry communities in spalling was triggered in part by large scale fire disasters that shook the public. In 90s of the last century, number of large fires happen in tunnels (Great Belt tunnel in 1994, Channel tunnel[9] in 1996 and Mont Blanc tunnel in 1999), causing serious and expensive damage; those three fires were summarized and discussed by Khoury[10].

On November 18, 1996, fire occurred in railroad tunnel connecting France and England, known as the Channel tunnel. Locomotive with 10 train wagons and 9 trucks burned for about 10 hours resulting in severe structural damage and 8 people injured. The costs due to damage of vehicles and tunnel alongside with costs related to disruption of services were as high as £50 million according to Kodur[11]. Maximal temperatures reached varied from 700°C[9,12] to 1000°C[11]. Ulm[9,12] reported economical loses alone reaching around $1.5 million per day over 6 months of repairs when the tunnel was closed. Tunnel was formed of 45 cm thick precast reinforced concrete rings, hundreds of meters of tunnel were damaged as result of fire, with average depth of spalling from 10 to 20 cm. At some parts of the tunnel, concrete rings were destroyed up to the chalk substratum[11]. This indicates significance of damage caused by fire and need for deeper understanding of mechanisms of spalling.

There are number of methods that have been proved capable of preventing or decreasing explosive spalling, e.g. addition of fibers. However, due to lack of clear guidelines and single fire scenario, there is no general protective method validated by fire test. To facilitate wide and safe application of HPC, fire safety design and protective methods must be based on deep understanding of processes underlying explosive spalling and evolution of material properties in case of fire.

The new imaging and characterization methods developed in recent years applied together on unified set of materials enable us to deliver new insight into the fundamental mechanisms of fire spalling, with the overall goal of eventually improving the fire resistance of HPC.

GOALS OF THE THESIS

The goal of the Thesis is to validate complex non-destructive measuring technics from other fields to evaluate thermal damage of concrete.

OBJECT OF THE THESIS

This work gives the qualitative and quantitative evaluation of SAP (superabsorbent polymer) as admixture to limit damage induced by elevated temperatures. The nonlinearity of the samples accessed by means of nonlinear resonance ultrasound spectroscopy highlights the combined effect of SAP and PP (polypropylene) fibers on state of the material both before the thermal loads and after.

The new imaging and characterization methods developed in recent years put all together on unified set of materials enables me to deliver new insight into the fundamental mechanisms of fire spalling, with the overall goal of eventually improving the fire safety of HPC.

OBJECTIVES OF THIS THESIS

To reach the goals, the following objectives are set:

- Summarize effect of elevated temperatures on concrete from literature, with focus on residual properties of concrete;
- Identify the fundamental parameters that facilitate or prevent spalling by means of studying Ordinary Concrete (OC) mix that would never experience explosive thermal spalling and plain High Performance Concrete (HPC) matrix, that would experience spalling under the same conditions;
- Modify the HPC matrix with admixtures to limit or eliminate spalling;
- Investigate residual structure and residual mechanical properties of all the mixes over time and due to thermal treatment at elevated temperatures;
- Investigate thermal damage of concrete by means of non-destructive methods; establish methods for quantitative evaluation of the damage.

SCIENTIFIC NOVELTY OF THE STUDY

This Thesis provides a systematic study of a broad set of concrete properties under well controlled, unified conditions.

To the best of the author's knowledge, for the first time an actual spalling was recorded during Neutron radiography measurements. Owing to a high attenuation of neutron beam by hydrogen, neutron imaging allows to study distribution of water in cement-based materials. The neutron radiography was carried out on samples of mortar while exposed to high temperatures. To this end, the samples were placed on a heating plate with specially designed protective shields to protect the delicate neutron imaging setup (in particular scintillator) from explosive debris. In this way, a unique result could be obtained: a live movie of the distribution of moisture in the sample on the onset of spalling.

To the best of the author's knowledge, for the first time complex real-time measurements of vapor pressure in the pores, temperature gradients in material, neutron radiography and the thermal loading of the sample were simultaneously combined.

For the very first time effect of SAP on thermal damage of concrete was evaluated by non-destructive methods.

For the very first time three ultrasonic methods were used to evaluate thermal damage of concrete, and the obtained ultrasonic data is supported by micro Computed Tomography (uCT) of the very same specimens before and after thermal damage.

STRUCTURE OF THE THESIS

The Thesis consists of annotation, introduction, 4 main chapters that are divided into subsections, conclusions, list of literature and appendix.

The Thesis consists of 120 pages and 2 appendices, including 84 figures and 14 tables. 144 literature sources were used in the literature review, to describe the methodology, to support discussions and conclusions driven.

First chapter of the Thesis is the literature review where effect of high temperatures on structures and concrete as material is described. It includes the definition of fire curves and testing parameters used to evaluate mechanical properties of concrete and changes of microstructure. Chapter 1 includes review on the main theories of explosive fire spalling due to elevated temperatures, the factors associated with the spalling and techniques to prevent the spalling.

Chapter 2 focuses on materials and the mix composition as an object of this study. The criteria for mix designs are put forward. Mix designs are justified by their performance under normal conditions and susceptibility to explosive thermal spalling.

Chapter 3 contains detailed description of material, evaluation of mechanical properties and microstructure. The evolution of residual properties after exposure to high temperatures at different load levels is presented. Beside conventional properties, microstructure is studied by means of mercury intrusion porosimetry on large number of samples, the evolution of residual breakthrough radius over wide range of temperatures is evaluated.

Chapter 4 visualizes the processes that takes place in concrete under high temperatures by means of non-destructive methods. For the very first time the actual explosive thermal spalling was visualized by means of Neutron radiography. Temperature, vapor pore pressure and moisture profiles were measured simultaneously during thermal heating from one side, to ensure 1D mass transport. Linear and non-linear ultrasonic methods were performed on the very same samples before and after thermal loading. The very same samples were used for μCT, qualitative evaluation of thermal cracks is provided and discussed.

APPROBATION OF RESULTS AND PUBLICATIONS

The main journal articles are listed below:

1. Toropovs, N., Monte, F. L., Wyrzykowski, M., Weber, B., Sahmenko, G., Vontobel, P., Felicetti, R & Lura, P. (2015). Real-time measurements of temperature, pressure and moisture profiles in High-Performance Concrete exposed to high temperatures during neutron radiography imaging. *Cement and Concrete Research*, *68*, 166-173.
2. Zhu, P., Brunner, S., Zhao, S., Griffa, M., Leemann, A., Toropovs, N., Malekos, A., Koebel, M. & Lura, P. (2019). Study of physical properties and microstructure of aerogel-cement mortars for improving the fire safety of high-performance concrete linings in tunnels. *Cement and Concrete Composites*, *104*, 103414.
3. Dauti, D., Tengattini, A., Dal Pont, S., Toropovs, N., Briffaut, M., & Weber, B. (2018). Analysis of moisture migration in concrete at high temperature through in-situ neutron tomography. *Cement and Concrete Research*, *111*, 41-55.
4. Dauti, D., Tengattini, A., Pont, S. D., Toropovs, N., Briffaut, M., & Weber, B. (2020). Some observations on testing conditions of high-temperature experiments on concrete: an insight from neutron tomography. *Transport in Porous Media*, *132*(2), 299-310.

5. Dauti, D., Dal Pont, S., Weber, B., Briffaut, M., Toropovs, N., Wyrzykowski, M., & Sciumé, G. (2018). Modeling concrete exposed to high temperature: Impact of dehydration and retention curves on moisture migration. *International Journal for Numerical and Analytical Methods in Geomechanics, 42(13)*, 1516-1530.
6. Zhong, P., Wyrzykowski, M., Toropovs, N., Li, L., Liu, J., & Lura, P. (2019). Internal curing with superabsorbent polymers of different chemical structures. *Cement and Concrete Research, 123*, 105789.
7. Boshoff, W., Mechtcherine, V., Snoeck, D., Schröfl, C., De Belie, N., Ribeiro, A. B., ... & Lura, P. (2020). The effect of superabsorbent polymers on the mitigation of plastic shrinkage cracking of conventional concrete, results of an inter-laboratory test by RILEM TC 260-RSC. *Materials and structures, 53*, 1-16.
8. Waldvogel, M., Zurbriggen, R., Toropovs, N., Berger, A., & Herwegh, M. (2023). Distribution and evolution of (micro) strain and stresses in flexible, waterproofing membranes using digital image correlation and finite element modelling. *Cement and Concrete Composites, 138*, 104982.
9. Bernard, E., Jenni, A., Toropovs, N., & Mäder, U. (2023). Percolation experiment across a 10-year-old interface between Opalinus Clay and Portland concrete. *Cement and Concrete Research, 170*, 107180.
10. Hu, Z., Cajuhi, T., Toropovs, N., Griffa, M., Wyrzykowski, M., Kaestner, A., ... & Lura, P. (2023). A neutron radiography study on the drying of cement mortars: effect of mixture composition and crack length. *Cement and Concrete Research, 172*, 107245.
11. Wyrzykowski, M., Toropovs, N., Winnefeld, F., & Lura, P. (2024). Cold-bonded biochar-rich lightweight aggregates for net-zero concrete. *Journal of Cleaner Production, 434*, 140008.
12. Wyrzykowski, M., Schroefl, C., Toropovs, N., Lura, P., Snoeck, D., Bettencourt Ribeiro, A., ... & Mechtcherine, V. (2024). Verification of the presence of superabsorbent polymers (SAP) in fresh concrete: results of an interlaboratory study of RILEM TC 260-RSC. *Materials and Structures, 57(4)*, 69.

1. CONCRETE SUBJECTED TO HIGH TEMPERATURES. LITERATURE STUDY.

1.1. EFFECT OF HIGH TEMPERATURES ON STRUCTURES

Performance of structure under fire depends on number of factors. Attempts to summarize these factors and develop regulations to test structures exposed to fire comes back to 1903, when the first testing standard of fire resistance was introduced[13] during Fire Prevention Congress in London 1903.

Failure of structures could occur due to deterioration of mechanical properties of concrete or the reinforcing steel, loss of bond with reinforcing steel, or spalling of concrete. Structural element has to be designed to fulfil its load-bearing functions for a required time in a given fire scenario. According to EN 1992-1-2[14], both nominal fire scenario and parametric fire approach can be used to ensure safety of the structure. Structural Eurocodes deals with passive fire protection of structures in terms of designing structures and members. Both active measures for concrete as material and passive measures for structures are discussed in part 1.4 of this work.

As the most straightforward and obvious effect of fire on any material or structure is the direct exposure to flame, it is generally known that concrete and its steel reinforcement do not burn. They do not emit toxic fumes, do not produce dangerous smoke and do not lose molten particles. Yet, during fire, the structures are at risk of failure because the mechanical properties (strength) of concrete and even more so, of steel, reduce significantly. The spalling is dangerous because: i) it exposes the steel reinforcement to high temperatures and hence leads to its faster thermal deterioration; ii) leads to the loss of bond with the reinforcement locally; iii) in extreme cases leads to a decrease of the cross-section area of the concrete members.

As any material, concrete and concrete structures would have thermal expansion in the case of fire, where linear coefficient of thermal expansion of concrete is around 10×10^{-6}/°C and corresponding coefficient for steel reinforcement is around 13×10^{-6}/°C.

Explosive spalling as a resulting effect of high temperatures on concrete structures is in spotlight of this study. Spalling, as a case, is more structure related characteristic than property of material. Khoury[10] summarized forms and characteristics of spalling (see Figure 1.1).

Spalling	Time of occurrence (min)	Nature	Sound	Influence	Main influences
Aggregate	7–30	Splitting	Popping	Superficial	H, A, S, D, W
Corner	30–90	Non-violent	None	Can be serious	T, A, F_t, R
Surface	7–30	Violent	Cracking	Can be serious	H, W, P, F_t
Explosive	7–30	Violent	Loud bang	Serious	H, A, S, F_s, G, L, O, P, Q, R, S, W, Z

A = aggregate thermal expansion, D = aggregate thermal diffusivity, F_s = shear strength of concrete, F_t = tensile strength of concrete, G = age of concrete, H = heating rate, L = loading/restraint, O = heating profile, P = permeability, Q = section shape, R = reinforcement, S = aggregate size, T = maximum temperature, W = moisture content, Z = section size

Figure 1.1 Forms of spalling, summarized by Khoury[10].

While effect of temperature on material can be characterized on small samples in well-defined thermal conditions created in ovens, effect of high temperatures and fire on structural

elements is described under temperature conditions defined by standard fire curves. To define curves, data was recorded both from controlled real fires in closed (e.g. disused tunnels) and opened environment, as well from laboratory tests. As result of data obtained in these tests, number of curves were developed to describe dependence of temperature to time.

Two main types of Fire load curves are Cellulosic fire curve and Hydrocarbon (HC) fire curve. The main difference is the time it takes to reach its maximum temperature, where burning rate in cellulosic fires is comparably slower due to "fuel" for fire are building materials and content of building, while temperature rise in hydrocarbon fires is significantly faster as "fuel" for fire are hydrocarbons in petrochemical facilities or actual fuel in the cars, as for fire in tunnels and parking facilities. Less tests are performed applying Jet fuel fire scenario curve, where maximal temperature rise is instant.

One of most used in practice is Cellulosic fire curve defined in ISO 834 and number of other national standards (for example, DIN 4102, EN 1363-1 and BS 476); it is described by following Equation 1.1:

Equation 1.1

$$T = 20 + 345 \log_{10}(8t + 1)$$

where T is the gas temperature in the fire compartment (°C) and t – time (min).

As mentioned above, Hydrocarbon curve describes rapid rise of temperatures, reaching 1100 °C in about 30 minutes (see), while for Cellulosic fire curve it takes 3 hours to reach its maximum temperature. With progress in industrial development, it became obvious, that Cellulosic curve does not describe fire scenario in petrochemical industry. This resulted in Hydrocarbon curve described by Equation 1.2.

Equation 1.2.

$$T = 20 + 1080(1 - 0.325e^{-0.167t} - 0.675e^{-2.5t})$$

where T is the gas temperature in the fire compartment (°C) and t – time (min).

Over time and devastating fire cases, maximal temperature of 1100 °C appeared not to be the limit for many Hydrocarbon fires and a new curve, following the same temperature gradient was implemented. So called Hydrocarbon Modified (HCM) fire curve derives from normal Hydrocarbon curve and is described by Equation 1.3:

Equation 1.3.

$$T = 20 + 1280(1 - 0.325e^{-0.167t} - 0.675e^{-2.5t})$$

where T is the gas temperature in the fire compartment (°C) and t – time (min).

Both HC and HCM curves reach their maximal temperatures around 30 minutes from the start, with maximums at 1100 °C and 1300 °C correspondingly with total duration of the load set at 3 hours. More rapid temperature increase scenario was proposed and applied in Germany, resulting in two curves (RABT-ZTV, see Table 1.1) for transport related fires with sudden increase to 1200 °C within 5 minutes, hold of maximal temperature for 25 minutes for car

related fires and 55 minutes at the maximal temperature for train fires and uniform decrease of the temperature down to 15 °C for 110 minutes.

Table 1.1.

Time-temperature program of RABT-ZTV curves

Temperature, °C	Time, min	
	Cars	Trains
15	0	0
1200	5	5
1200	30	60
15	140	170

Fire curves described above would either form a plato at maximal temperature after rapid increase of temperature (HC, HCM and RABT), or are described by temperature increase over time, where each next point of the curve has higher temperature, meanwhile, yet another curve was developed in Netherlands by Ministry of Transport, the RWS (Rijkswaterstaat) curve.

RWS fire curve combines instant increase of temperature with gradual development of temperature in already very high ranges, slight decrease and a plato between 2 and 3 hours from the start. Curve describes the case of Hydrocarbon fire event, reaching the highest maximal temperature from all the curves described above, standing at 1350 °C after one hour after the start of the fire. This curve describes in some way the worst single event fire, where a petrol tanker of 50 m^3 in volume would set on fire, producing fire load of 300 MW in relatively closed environment (e.g. tunnel). Similar as other curves it was developed as result of large-scale field-test that took place in Netherlands in 1979.

Table 1.2.

Temperature development in RWS curve

Time, min	Temperature, °C
0	20
3	890
5	1140
10	1200
30	1300
60	1350
90	1300
120	1200
180	1200

While ISO 834 standard Cellulosic fire curve is the most common for testing overall structures, national standards often have higher criteria for transport infrastructure and use HC or HCM type curves, while often despite local legislation that would allow Cellulosic or Hydrocarbon curve, project of high importance and expenses would still specify RWS curve as criteria. So, it was for Kallanga-Paya Lebar Expressway (KPE) in Singapore and The Palm Jumeirah tunnel in Dubai, UAE.

Complex large-scale fire test was carried out in 2003 in Norway; unused Runehamar tunnel became a testing facility, where five large-scale fire tests were carried out. Large amount of data was obtained[15–18] and described in details, e.g. gas temperature[16], fire spread and flame length[17] and heat release rates[18]. Tests made a significant impact and highlighted extreme conditions of fire in tunnels. During test T1[15], maximal temperature of 1359.6 °C was recorded, it is to note, that the fire load was generated by HGV trailer mock-up made of 360 wood pallets ($1200 \times 800 \times 150$ mm^3 in size), 20 wood pallets ($1200 \times 1000 \times 150$ mm^3 in size), 74 PE plastic pallets ($1200 \times 800 \times 150$ mm^3 in size) and 122 m^2 polyester tarpaulin. This temperature significantly exceed temperatures of Cellulosic fire curve that was expected from wooden pallets, and was still higher then HC curve. International Tunneling Association take into account the data obtained in Runehamar tunnel fire test in their guidelines[19] and recommended to follow RWS curve scenario for road tunnels. While an actual fire test in the tunnel is a very special case, smaller scale tests of tunnel elements has practical meaning and results in valuable data to predict an actual behavior of the tunnel lining in the case of fire, recently Alhawat *et al*.[20] proposed design of the fire test on tunnel lining elements. Fire load during proposed by Alhawat *et al*. test design aimed to follow RABT time-temperature curve[20].

Some of fire accidents in the tunnels are summarized below in Table 1.3.

Table 1.3.

Few fire cases in tunnels, adapted from ITA guidelines[19]

1949	Holland 2550 m	New York USA	Lorry with 11 tons of carbondisulfide	Load falling off lorry leading to explosion	4 h	66 Injured due to smoke inhalation	10 lorries and 13 cars	Over 200 m of tunnel had serious damage
1974	Mont Blanc 11600 m	France-Italy	Lorry with 11 tons of carbondisulfide	Motor	15 min	1 injured		
1976	Crossing BP-A6 430 m	Paris, France	Lorry with drums of 16 tons polyester film	High speed	1 h	12 injured due to smoke inhalation	1 lorry	Over 150 m of tunnel had serious damage
1978	Velsen 770 m	Velsen, Netherlands	4 lorries, 2 cars	Front rear collision	1 h 20 min	5 dead and 5 injured	4 lorries and 2 cars	Over 30 m of tunnel had serious damage
1979	Nihonzaka 2045 m	Shitzuoka, Japan	4 lorries and 2 cars	Front-rear collision	160 h	7 dead and 1 injured	127 lorries and 46 cars	Over 1100 m of tunnel had serious damage
1980	Kajiwara 740 m	Japan	1 truck with 3600 liters of paint	Collision with side wall and overturning	n/a	1 dead	2 trucks	Over 280 m of tunnel had serious damage

1982	Caldecott 1028 m	Oakland, USA	1 car, 1 coach, 1 lorry with 33000 liters of petrol	Front-rear collision	2 h 40 min	7 dead and 2 injured	3 lorries, 1 coach and 4 cars	Over 580 m of tunnel had serious damage
1982	Salng 2700 m	Mazar-e-Sharif-Kabul, Afganistan	Soviet militarz column with at least 1 petrol truck	Most likely, military activities	n/a	more then 200 dead	n/a	n/a
1983	Pecorila Galleria 662 m	Genoa, Italy	Lorry with fish	Front-rear collision		9 dead and 22 injured	10 cars	No severe damage
1986	L'Arme 1105 m	Nice, France	Lorry with trailer	Braking after high speed	n/a	3 dead and 5 injured	1 lorry and 4 cars	Equipment destroyed
1987	Gumefens 343 m	Bern, Switzerland	1 lorry	Front-rear collision	2 h	2 dead	2 lorries and 1 van	No severe damage
1990	Røldal 4,656 m	RØldal, Norway	Van with trailer	n/a	50 min	1 injured	n/a	No severe damage
1990	Mont Blanc 11600 m	France-Italy	Lorry with 20 tons of cotton	Motor issue	n/a	2 injured	1 lorry	Equipment destroyed
1993	Serra Ripoli 442 m	Bologne, Italy	1 lorry and 1 car	Collision with side wall and overturning	2.5 h	4 dead and 4 injured	5 lorries and 11 cars	No severe damage
1993	Hovden 1290 m	HØyanger Norway	Motor cycle 2 cars	Front-rear collision	1 h	5 injured	1 motorcycle and 2 cars	111 m insulation material destroyed
1994	Huguenot 3914 m	South-Afrika	Bus with 45 passengers	Electrical fault	1 h	1 dead and 28 injured		Serious damage
1995	Pfander 6719 m	Austria	Lorry with trailer	Collision with side wall and overturning	1 h	3 dead, 4 injured		Serious damage
1996	Isola Delle Femmine 148 m	Palermo, Italy	1 tanker with liquid gas and 1 bus	Front-rear collision	n/a	5 dead and 20 injured	1 tanker, 1 bus, 18 cars	Serious damage

1999	Mont Blanc, 11600m	France-Italy	Lorry with flour and margarine	Motor defect	n/a	39 dead	23 lorries, 10 cars, 1 motorcycle, 2 fire engines	Severe damage, tunnel closed for 2.5 years
1999	Taure, 6401 m	Salzburg, Austria	Lorry with paint	Front-rear collision	n/a	12 dead and 49 injured	26 cars	Severe damage
2000	Seljestad 1272 m	Drammen, Norway	Diesel fire in the engine room	Front-rear collision	45 min	6 injured	1 lorry, 6 cars and 1 motorcycle	Serious damage, 1 mill NOK estimated costs
2001	Prapontin 4409 m	Torino, Italy	Lorry truck	Track had technical problems	n/a	19 injured due to smoke inhalation	n/a	Closed for 8 days in one way

The examples given above highlight diversity and severity of the accidents. Large scale severe fire accidents cause casualties and material loss, same time leading to changes in codes. As example, fire in Tauern that eventually led to number of changes in the guidelines, see Table 1.4.

Table 1.4.

Changes in Austrian Life Safety guidelines for tunnel design, summarized by Leitner[21].

	Before fire accident	Changes in guidelines after the fire
Pavement	Asphalt or concrete.	If tunnel is longer then 1km, only concrete pavement
Caps of cable duct	No requirement.	Up to 1 meter in length.
Support for ceiling	Console.	Reinforced console.
Vehicle cross passages	Every 2nd lay-by-niche.	Every lay-by-niche.
Water supply	In single-tube tunnels, operation from one portal possible. In twin-tube tunnels, ring required.	In single-tube tunnels, operation from both portals. In twin-tube tunnels, ring required.
Distance of first emergency niche from portal	Maximal distance of 500 m.	Maximal distance decreased to 250 m.
Signalization of escape direction	At cross passages.	Every 150 m with lighting at 1 m height.

Based on previous experience and extreme fire cases that led to multiscale damage, more and more sophisticated and extreme fire tests are performed to increase the safety of the important structures, the large-scale testing objects are built to achieve realistic fire conditions in order to improve the safety of the actual structure. A great example is Honk Kong-Zhuhai-Macao immersed tunnel built in scale 1/5, where external load and fire from two sides were ensured[22]. As result of this large scale test, Dong et al.[22] observed almost 100 % spalling of interior area of the tunnel, with maximum depth up to 142.2 mm.

This being said, the effect of concrete structures being exposed to sever fire leads to not only serious damage and high expenses, but it stresses the nesesity to study the nature of damage and implement changes in building codes.

1.2. EFFECT OF HIGH TEMPERATURES ON MATERIALS

The spalling is a structurally related damage mechanism in a sense that it depends upon geometrical, external load and kinetics factors, occurring on the top of the material changes being a static function of temperature only. In this chapter only the later aspect, which is residual effect of temperature on material properties is considered. It should be stressed that it is not always possible to fully decouple the other factors (e.g. geometry or kinetics) from the net effect of temperature. This is usually done by studying possibly slow temperature changes and small sample sizes.

Concrete is non-flammable. However, increased temperatures affect the material. Already at moderate temperatures above the room temperature, mass loss due to increased drying/evaporation rate is observed. At higher temperatures (already starting from 50 – 100 ° C, depending on the chemical composition), a loss of chemo-physically bound water from the hydrated phases (i.e. dehydration) takes place. At still higher temperatures decomposition of carbonates takes place, and at extreme temperatures melting takes place. These changes are schematically summarized in Figure 1.2 by Khoury[10]. Changes above melting point are not relevant, as material is no longer solid. In this study, properties of concrete are determined, mostly, at temperatures not exceeding 600°C, because at higher temperatures the failure is expected in any case that excludes further service of concrete as safe structural material (see Figure 1.2 and Khoury[10]).

Here it is important to distinguish temperature of fire and an actual temperature at any point of material. While fire curves determine temperature of fire/gases, gradient of temperatures is expected in real structure changing in time. Within Chapter 3 of this study, I aimed to achieve uniform distribution of maximal temperature within volume of samples in all test conditions, to determine exact properties of material at each temperature step. The difference between tests at cold and hot state is discussed below in parts 1.2. and 1.5.

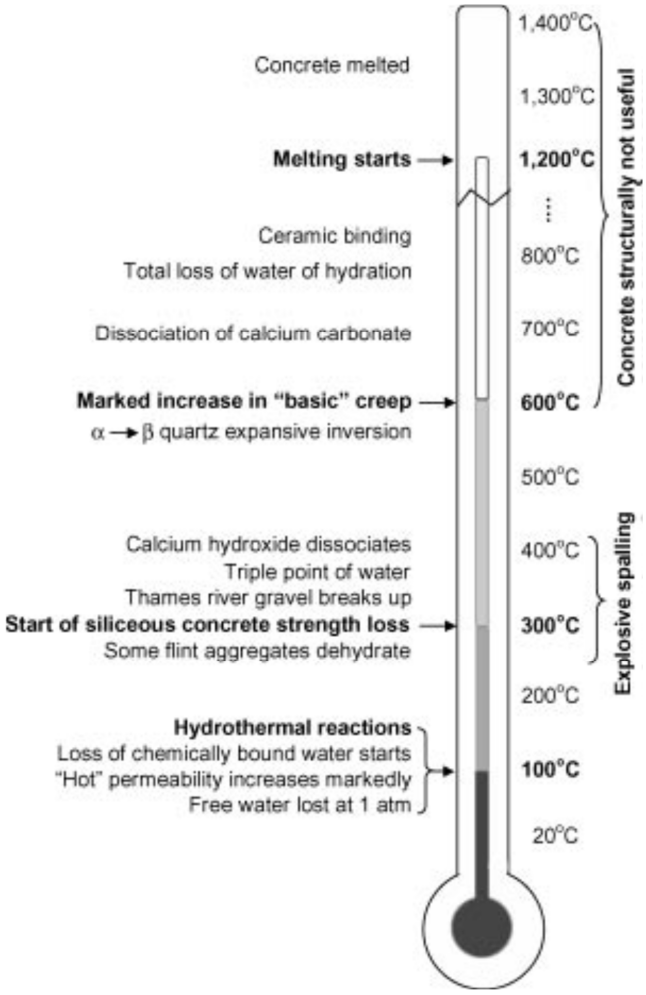

Figure 1.2. Processes in Portland cement concrete, summarized by Khoury[10], where temperatures are for the concrete material and not temperatures of fire or surface of concrete only.

Obtaining the most exact and wide, complimentary properties of concrete as it overcomes changes caused by fire load at each time/temperature step is not an easy challenge. Spalling phenomena discussed in this Thesis is related to performance of the structure at high temperatures, which means, that material itself expiriences mechanical and thermal loads at the same time. From testing point of view, this means, that samples used to measure mechanical, transport or other properties have to be simultaniusly mechanically and thermally loaded, which is not a safe working/testing environment in most of the cases. As for example, in part 0 of this study, pore structure of material after being exposed to high temperatures is characterized in a residual state by means of Mercury Intrusion Porosimetry (MIP) after possible water left in the pores was removed by solvent exchange method using flammable solvents as Isopropanol and Petroleum ether. Combination of mercury, higly flammable solvents, mechanical loads and high temperatures at the same time is virtually impossible to carry out. However number of groups focused their research on testing properties of concrete at high temperatures in real time.

Regarding the hot tests, there are two main test approchies do determine mechanical properties. One, when the samples undergo thermal loading first and then, after reaching the designed temperature are taken out of the furnace and are tested in hot state. Second, is more complex and demanding to testing conditions: simultanious thermal and mechanical loading; when the samples are loaded to designed workload of the structure and then, after the designed temperature is reached, samples are loaded to obtain ultimate mechanical properties in the hot state. Lo Monte[23] measured indirect tensile strength with the first approach, where the time between the thermal loading and mechanical loading was just about 2 minutes, however the focus of this particular study is the effect of a certain pore pressure combination on tensile capasity at hot state, which makes the test even more complex. Same group from Polimi designed a test setup, where spalling of concrete can be studied while thermal load is provided simultaneusly with mechanical load of the actual service state, the designe is provided[24].

Most common assessment of effect of high temperatures on material is done by presenting the data of mechanical properties over range of temperatures and describing changes of microstructure due to thermal loads, some of the properties described in literature are summarized below. It is important to notice that most of mechanical properties summarized below are obtained after cooling down of the samples, i.e. in residual state.

Compressive strength

Data summarized below is adapted from number of studies[25–46] and is presented as a ratio of residual properties to the same property before thermal treatment; data is recalculated from the tables as well from the figures, and might have a slight deflection from the raw data of those studies (see Figure 1.3.). As for example, evolution of residual compressive strength over temperatures is presented for 101 mixes of concrete. In most of the papers temperature of the thermally non-treated samples is defined as 20, 25 or 30 °C, where initial temperature is not defined numerically and is stated as "room temperature", for the matter of plotting the data, "room temperature" is assumed 20 °C, as for example data from paper by Irshidat[33].

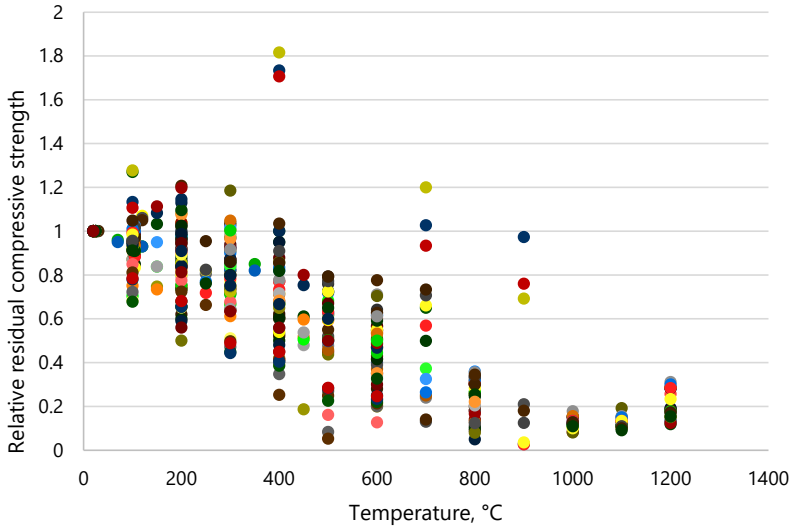

Figure 1.3. Relative residual compressive strength, data adapted from[25–46].

Data summarized above contains different types of concrete, treated at different state and residual properties are presented, as the final state of the samples is the same (after cooling down to room temperature). Residual compressive strength reported by Lau and Anson[46] is a part of the figure as well, but explicitly, they report changes of residual strength of steel fiber reinforced concrete depending on level of saturation of samples before thermal treatment (however, all the thermally loaded specimens were initially treated at 105 °C according to saturation methodology of the study). Samples at saturation levels 20, 60 and 100% were loaded at 9 different temperatures, up to 1200 °C. Three different concrete mixes were produced as references to same mixes with steel fibers, resulting in total of 6 mixes. Mixes with w/c of 0.66, 0.56 and 0.32 resulted respectively in 39, 53 and 99 MPa 28 day compressive strength for reference mixes. Below, the data from all 6 mixes per saturation level is averaged in one curve (see Figure 1.4).

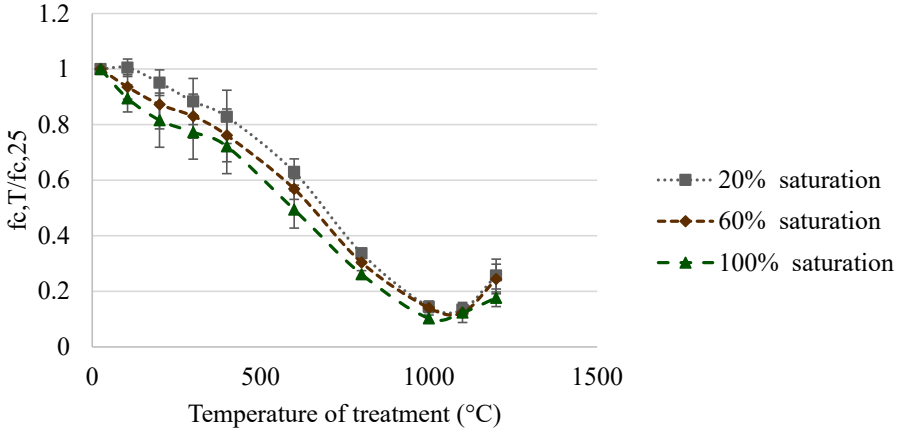

Figure 1.4. Changes of compressive strength of concrete at different saturation levels over high temperatures, data adapted from Lau and Anson[46]

As seen above, more rapid decrease of compressive strength is observed with increase in saturation of the samples.

As in general, sharp decrease of compressive strength at temperatures higher than 400 °C is observed and Choe *et al*.[47] reports higher degradation of compressive strength for high strength concrete than for one with a normal strength described by Eurocode. In studies summarized above, the residual strength was measured soon after thermal exposure, on a longer distance changes of residual properties over time are studied by Papayianni[37] (see Figure 1.5) where recovery of compressive strength is reported.

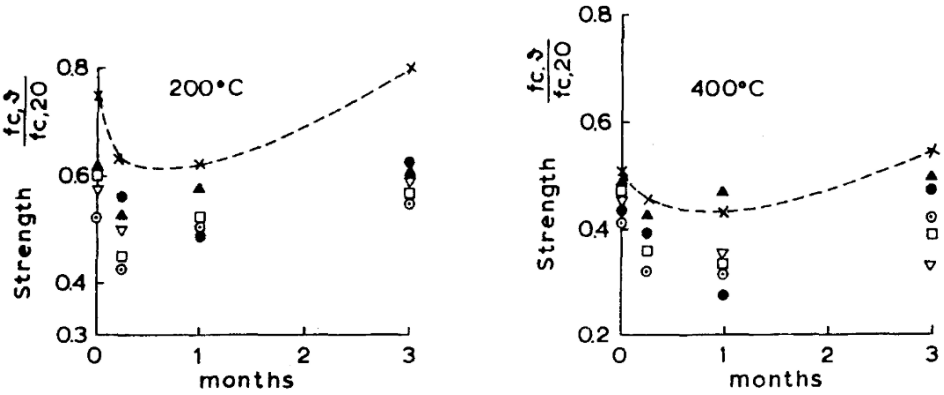

Figure 1.5. Strength recovery of concretes heated at 200 °C and 400 °C, as reported by Papayianni[37].

Flexural strength

Similarly to other summarized properties, results of residual flexural strength are adapted from number of studies[27,28,30,33,35,36,46]; including normal strength concrete, reactive powder

concrete, high strength concrete, both with fibers and without. Each color of the dot represents a single mix from one of the studies (see Figure 1.6).

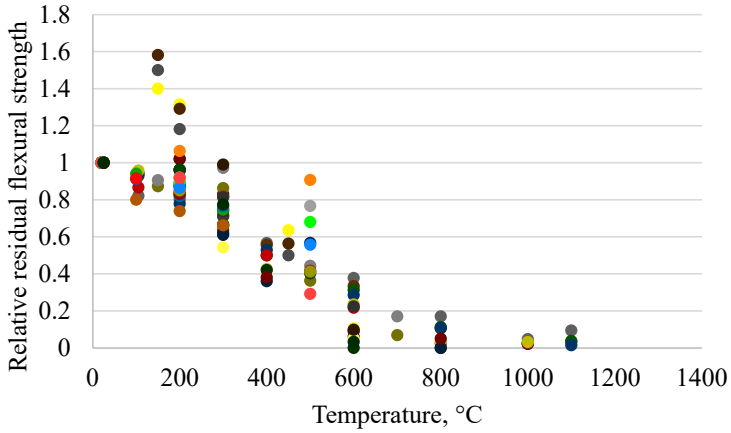

Figure 1.6. Relative residual flexural strength, adapted from[27,28,30,33,35,36,46].

Compressive stress-strain diagrams

Stress-strain diagrams are reported less often than results of compressive strength, while being part of the same loading procedure, here it is important to keep in mind that initial slope/increase and the maximal value of stress is the correct data, while part of the graph after reaching the maximal stress is related to non-homogenous sample with decreased cross-section.

Felicetti and Gambarova[25] reported stress-strain diagrams (see Figure 1.7) for two types of concrete (compressive strength 72 MPa and 95 MPa) with maximal temperature at 500 °C.

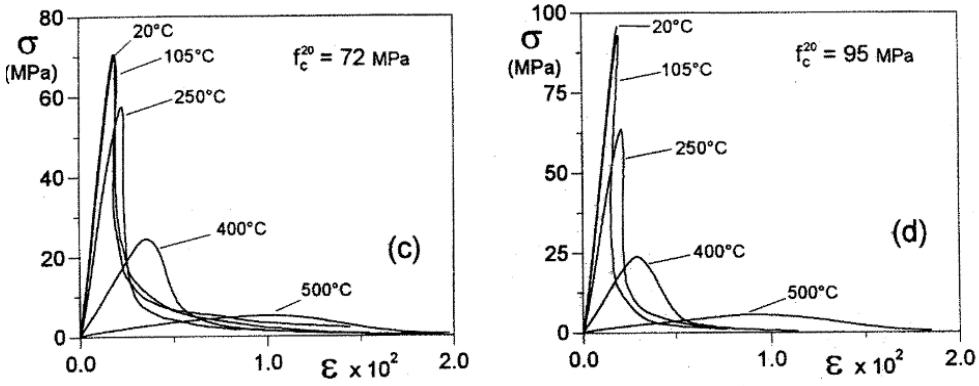

Figure 1.7. Stress-strain diagrams by Felicetti[25].

While Chang et al.[40] presented strain-stress diagrams for concrete cylinders of 150 mm in diameter and 300 mm in height, with initial compressive strength at 40 MPa (see Figure 1.8) and with thermal loading up to 800 °C. According to Chang et al.[40], shape of the curves for

loading temperatures higher than 600 °C are influenced by possible closing of the cracks (caused by thermal loading) at low steps of mechanical loading. This effect can be seen for the three highest temperatures at strain values at around 2×10^{-3} strains (see Figure 1.8). Smooth curves and no spalling of samples during thermal loading were achieved both by studying performance of normal strength concrete (40 MPa) and long storage of samples before thermal loading (18 month) to have lower moisture content.

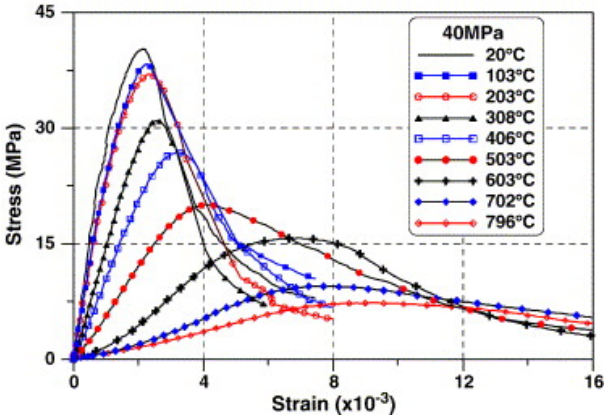

Figure 1.8. Stress-strain diagrams reported by Chang et al.[40].

Both studies conducted on samples in unstressed conditions during single high-temperature cycle of thermal loading and tests were performed after cooling down to room temperature in uniaxial compression. It was observed that with increase of temperature, stress-strain curves become flatter, peak stress value shifts down and rightwards, that is an indication of decrease of modulus of elasticity, the next property to take a closer look at.

Lately Huang et al.[48] studied coupled effect of high temperatures (200 °C and 400 °C) and strain rate on compressive strength of steel fiber reinforced concrete (SFRC). As in normal conditions, SFRC has a strain rate hardening effect; for thermally treated SFRC samples authors observed strain rate threshold, where if the strain rate is lower than the strain rate threshold, temperature softening effect was observed, and opposite, if strain rate was higher than a threshold, temperature hardening took place.

Liu and Tan[32,49] studied performance of strain hardening UHPC reinforced with fiber cocktails containing PE[32] and PVA[49] fibers together with steel fibers, they found that strain hardening performance was gone at temperatures above 300 °C and severe cracking and spalling was observed at temperatures above 400 °C for larger samples with PE fibers[32].

Modulus of elasticity

Examples of stress-strain diagrams in Figure 1.7. and Figure 1.8. indicate the evolution of Modulus of elasticity over high temperatures. As peak stress levels are decreasing and corresponding strain values are increasing, it is to expect decrease of the Young modulus, roughly speaking; softening of material is observed due to degradation of the structure and loss of water.

Below, Figure 1.9. summarizes research data on residual Young's modulus adapted from studies[29,31,33,37,40,43,45,46] conducted on different types of concrete, to represent a general trend of evolution of elasticity after treatment at high temperatures.

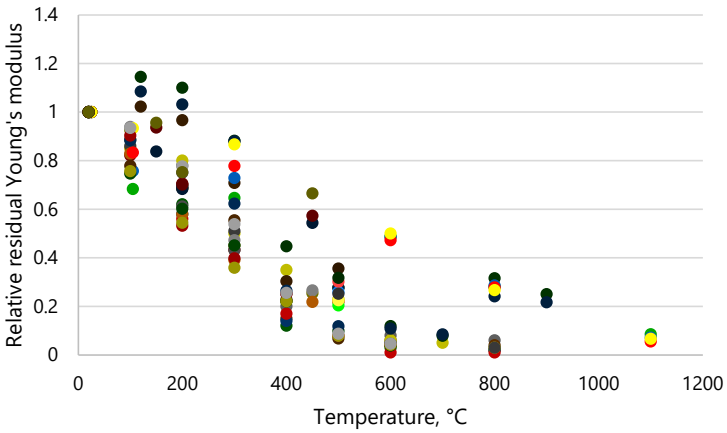

Figure 1.9. Relative residual Young's modulus, data adapted from[29,31,33,37,40,43,45,46].

Slightly higher relative residual Young's modulus is observed for reactive powder concretes studied by Zheng[43] who reports an increase of Young's modulus at temperature 200 °C and below (see Figure 1.9).

Lau and Anson[46] studied effect of steel fibers on number of properties of concrete after exposure to high temperatures, mixes with steel fibers showed higher modulus of elasticity than reference mixes with no fibers at all temperatures (study was conducted within 25-1100 °C range).

Splitting tensile strength

Values of relative residual splitting tensile strength over range of temperatures are adapted from literature[27,29,30,37,38,40,44].

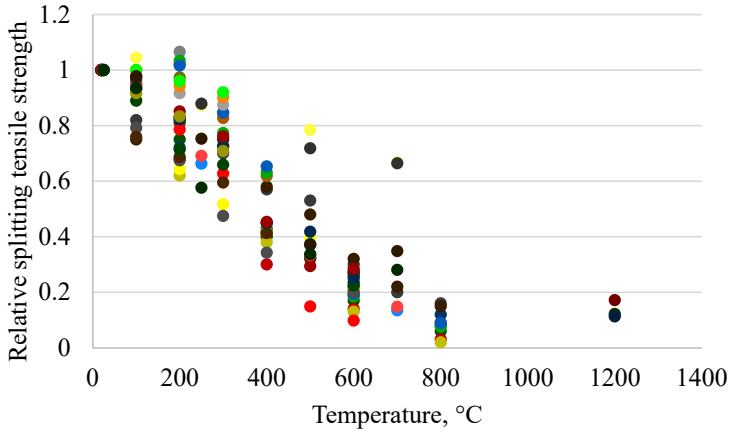

Figure 1.10. Relative residual splitting tensile strength, data adapted from[27,29,30,37,38,40,44].

Porosity

Brief summary of residual changes of porosity at high temperatures is presented below (see Figure 1.11). Mercury intrusion porosimetry (MIP) was used in all the studies[39,41,44,46,50], similarly to this Thesis (see part 3.3).

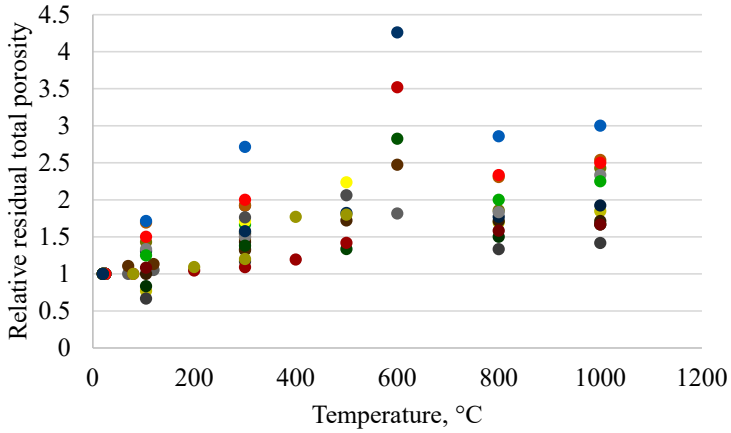

Figure 1.11. Relative residual total porosity, data adapted from[39,41,44,46,50].

Similarly to other properties summarized above, Lau and Anson[46] studied effect of saturation of samples prior to thermal loads as well by means of MIP. They summarized changes of total porosity and average pore diameter at high temperatures[46]. In Figure 1.12. we pivot the data; averaging relative changes of total porosity over all the mixes used in their study and separate them by level of saturation.

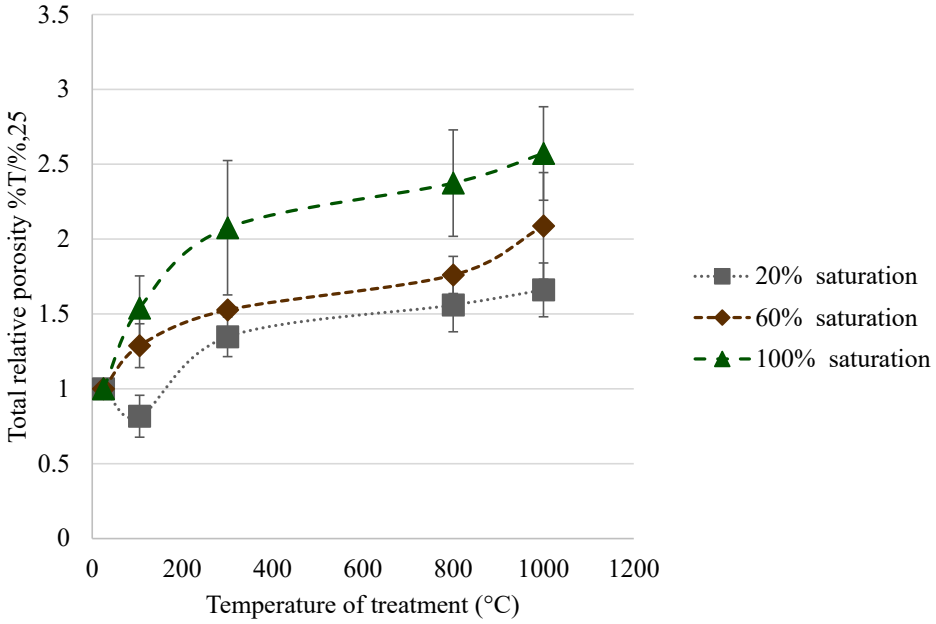

Figure 1.12. Relative changes of total residual porosity over high temperatures at different states of sample saturation before thermal loading, data adapted from Lau and Anson[46].

As it is seen from Figure 1.12 and is concluded by Lau and Anson[46], in general, higher initial saturation of the samples before thermal loading leads to a higher porosity. This indicates that higher saturation levels may lead to higher vapor pressure causing cracking and higher degrees of damage. While at lower temperatures with moderate heating rate higher saturation level could even contribute to further hydration and decrease of porosity.

Changes in hydration products

Exposure of concrete to high temperatures results not only in physical damage, but first it causes moisture movement and dehydration of hydrates. Collection of thermal analysis data on decomposition of phases at temperature 0 °C to 800 °C is provided by Collier[51]. While decomposition of pure phases can be measured with methods of Thermogravimetric Analysis (TGA), in real life structure the processes are more complex, as structural element has temperature gradients in case of fire and pressure build up is very likely, affecting temperature of decomposition of hydrates. Same time, as the nature of phase changes, like dehydration or decarbonation, is an endothermic reaction; this means decrease of the temperature if no new energy input is there.

General reactions of dehydration are provided in cement chemist's nomenclature below:

Equation 1.4.

$$C_8AFS_2H_{22} \xrightarrow{T_{onset}=40\,^{\circ}C} C_4AF + 2CH + 2CS + 22H$$

Equation 1.5.

$$C_3S_2H_3 \xrightarrow{T_{onset}=110\,^{\circ}C} C_3S_2 + 3H$$

Equation 1.6.

$$CH \xrightarrow{T_{onset} = 430\ °C} C + H$$

As seen from Equation 1.4. and Equation 1.6., the products of decomposition can further decompose at higher temperatures.

While straightforward composition and decomposition of pure phases is a well-studied topic, the dynamic phase composition during decomposition of other phases in conditions of elevated temperatures is rather complicated. A complex model predicting dynamic phase composition at temperatures up to 1200 °C is proposed by Jiang *et al.*[52]. The authors stress the importance of heating rates on instantaneous formation of phases. While the heating rates are described by fire curves, as discussed earlier, they describe the gas temperature next to surface of the structure; the actual distribution of temperatures at a single point over time is much different.

In this study, I perform TGA analysis on residual state of material, after treatment at elevated temperatures. Where samples are crushed before thermal loading to avoid thermal and moisture gradients. The concept of thermal moisture gradient when the samples of larger size are exposed to thermal load is investigated as well in part 3.2., methods, to substantiate the protocol chosen here.

Integrity of material evaluated with non-destructive methods: ultrasound-based measurements.

Most common ultrasonic method to evaluate state of concrete material is to measure Ultrasound Pulse Velocity (UPV). It is discussed further in part 4.2. Overall effect of high temperatures on integrity of the material is presented here as relative residual ultrasound pulse velocity. Ultrasound pulse velocity is a linear single pulse method; it gives us information on overall state of material, as it is sensitive to macro cracks and less sensitive to micro damage.

Figure 1.13. represents relative UPV measured on the samples at residual state, after being exposed to high temperature, where initial UPV (value = 1) measured on the samples before exposure to high temperatures, data summarized from number of papers[27,29,31,36].

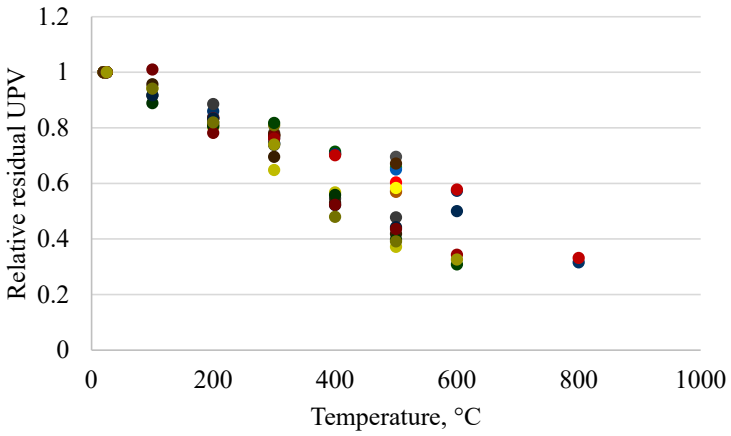

Figure 1.13. Relative residual UPV, data adapted from[27,29,31,36].

General trend seen in Figure 1.13. shows decrease of ultrasound pulse velocity over temperatures. Alongside possible damage due to high temperatures, at the moderated high temperatures concrete loses all the free water. UPV method is sensitive to moisture content in concrete, however, this can explain only initial drop in UPV, and the decrease of pulse velocity at temperatures higher than 200 °C is purely associated with effect of high temperatures. Talking about effect of moisture and temperatures in general, in conditions opposite to ones of interest in this Thesis, Lencis[53] observed significant increase of UPV for samples with high water content and at temperature down to -20 °C, as water solidifies and fill up pores, increasing propagation of waves.

Properties of concrete measured during hot tests

Properties summarized above correspond to residual state of samples after being exposed to high temperatures and cooling back down. Performance of structures during fire is related to properties of material at an actual hot state and has to do with dynamic processes of heating. Less data is available for this type of measurements, as well, not all the common methods to measure residual properties can be transferred to hot tests safely.

Compressive strength measured at the hot state is summarized in Figure 1.14., where data is adapted from[54–56].

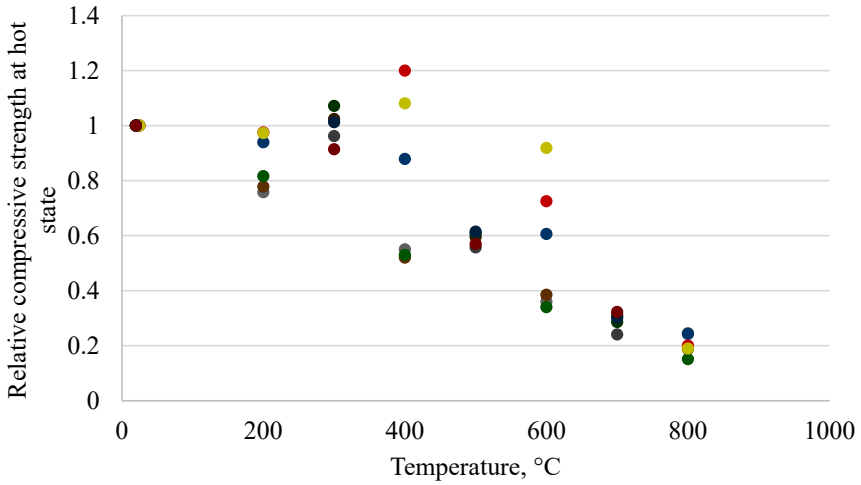

Figure 1.14. Relative compressive strength at hot state, data adapted from[54–56].

One can see that all the data indicates some sort of degradation at high temperatures. It is valid for hot and residual state of samples during compressive strength tests. Some slight increase in compressive strength in the range below 400 °C is observed for both states of the samples, however, the general trend at the higher temperatures is similar and the compressive strength drops down to 20 % of initial one when concrete is exposed to 800 °C.

1.3. FACTORS AND MECHANISMS OF EXPLOSIVE SPALLING IN CONCRETE STRUCTURES

The first theories on spalling mechanisms go back to the 1960's[57,58], see also historical overview prepared by Jansson[13], where spalling of concrete under fire as independent phenomena rising interest in research society goes back to 1854[13]. According to the pressure build-up theory[57], water accumulates behind the drying front because vapor produced at the drying front migrates towards the colder inner region, where it condenses. The condensed vapor reduces the gas permeability and may cause liquid water saturation of the pores, referred to as the moisture clog[4,59]. At the same time, the high rate of vaporization on the hot side of the moisture clog, together with the thermal dilation of vapor and air due to heating, induces gas pressure build-up in the pores. This process may lead to spalling if the solid pressure acting on the concrete stiff skeleton due to the gas pressure exceeds the tensile strength of the concrete (which at high temperatures is reduced by cracking and dehydration)[60]. Vapor pressure build-up concept is visualized by Ozawa and adapted here in Figure 1.15.

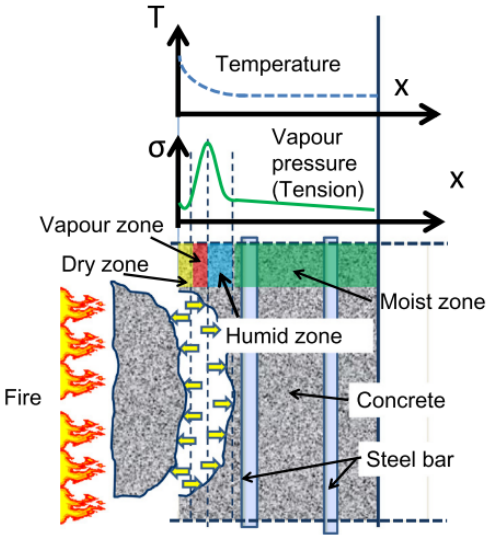

Figure 1.15. Vapor pressure build-up concept, adapted from Ozawa[61].

Another possible mechanism of spalling is described by the *thermal stresses theory*[58]. Since the temperature at the moisture clog is close to 100 °C and the surface temperature increases rapidly while the depth of the dry layer is still small, a steep thermal gradient develops between the heated surface and the moisture clog, which induces high thermal stresses. According to Saito[58], spalling is due to compression failure near the heated surface. Based on a detailed analysis of pore pressure and thermal stresses, Sertmehmetoglu[62] proposed that the compressive stresses near the heated surface result in tensile cracks parallel to the surface. The pressure developing in these cracks induces explosive spalling. Failure is further eased by stress concentration at the crack tips and by buckling due to compression. Sertmehmetoglu in his thesis[62] reproduces spalling of concrete at the room temperature by creating overpressure in artificially created cracks that are parallel to the surface of specimen. Cracks were created by

embedding metal discs at different distances, parallel to the investigated surface. Pressure was created around the disc and resulted in spalling. It is to notice that, as long as mechanism of spalling is not well defined, and an actual spalling can occur both due to gas pressure and due to water pressure, i. e. actual crack parallel to the surface can occur both in dry and wet zzonesof the concrete. Sertmehmetoglu designed his tests to create both gas pressure and water pressure at the level of artificial crack. At the same time, samples were in compression, load was applied parallel to artificial cracks[62]. Tests showed that occurrence of spalling increases with combination of compressive stress and gas/water caused pressure in the pores.

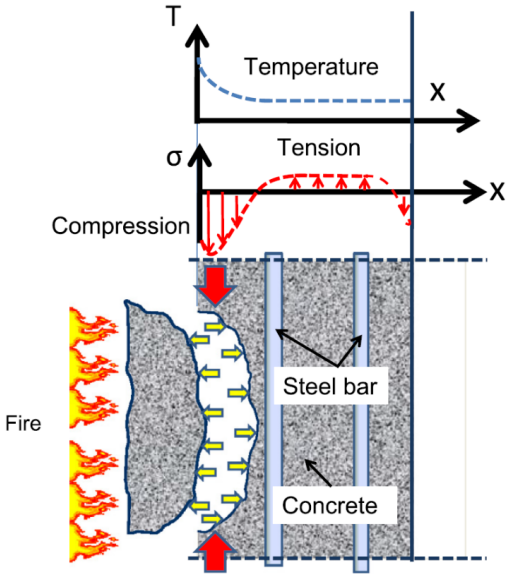

Figure 1.16. Thermal tension concept, adapted from Ozawa[61].

It needs to be underlined that the mechanisms proposed by the two theories (pressure build-up and thermal stress) are strongly coupled and both dependent upon the moisture distribution (and upon the formation of the moisture clog) during fire. Both processes progress at the same time and may influence boundary conditions of each other, affecting transport and mechanical properties of the material. Bažant sees the pore pressure as a "trigger of the explosive thermal spalling of high strength concrete", while the state of material that leads to the failure is driven by "amount of the energy stored due to thermal stresses"[63]. Idea of a trigger and a corresponding threshold value for spalling to occur is discussed by Lo Monte[23], where he describes it as a link between decay of apparent tensile strength and pore pressure.

Along with the moisture clog theory, the BLEVE (Boiling liquid expanding vapor explosion) phenomena that occurs at slow heating rates should be mentioned. When no sharp temperature gradient is formed, the conditions in the two nearby regions/pores are very similar. Hence, because of the similar pressures and temperature in the neighboring pores there is no driving force for the mass or energy exchange between them. This is valid for ideal case, two same shape and size pores. As before heating pore contains air, water and water vapor, at higher temperatures water evaporates, however, as conditions in the pore nearby are the same, vapor stays in the same pore, increasing the pressure. At increased pressure, the boiling point of water is increasing leading to condensation and presence of water in the liquid state within the pore.

Liquid water occupies less space than vapor, however when cracks appear, the sudden release of the pressure takes place resulting in instantaneous evaporation of superheated water, as boiling point drops down to 100 °C. This can lead to explosive spalling because of sharp volume change and high-energy release due to the phase change[64].

Focusing on the moisture clog, the risk of fire spalling increases when the internal relative humidity (RH) and the water saturation of pores are high, since a higher amount of moisture in the pores may lead to faster clogging. On the other hand, maintaining high RH in HPC is beneficial for reducing self-desiccation shrinkage and early-age cracks. Due to its low water-to-binder ratio (w/b), HPC can experience a considerable decrease of internal RH when the pores are partially emptied of water by the hydration process[65]. As a result, excessive self-desiccation shrinkage may lead both to macroscopic cracking in concrete members and to microcracking within the cementitious matrix. An efficient method for reducing self-desiccation shrinkage and at the same time promoting cement hydration is internal curing. Internal curing is based upon introducing into concrete, at the stage of mixing, of small (usually up to few-millimeters) reservoirs of water. The water is released from the reservoirs upon hydration to counteract self-desiccation and early age shrinkage. One of the recently introduced materials for internal curing reservoirs are superabsorbent polymers (SAP)[66]. SAP are polymers that have enormous water absorption capacity[67]. The particles of SAP swell upon absorption and form so-called hydrogel. The SAP suitable for concrete application can absorb pore fluid in amounts of about 20-30 times their own mass, while absorption of water is much higher[67]. The method is based on adding to the mixture dry SAP, that absorb water upon mixing and form small (100–200 μm across) water reservoirs uniformly distributed in the matrix[66]. When the hydration process binds mixing water and empties the capillary pores, water migrates from these water reservoirs and allows maintaining a high internal RH in the concrete, thereby reducing or eliminating self-desiccation shrinkage[66]. Thereby, increased risks of spalling under fire due to higher initial moisture content in HPC has to be balanced with long term service life of concrete structures affected by micro cracks from self-desiccation shrinkage, if no internal curing was used.

A brief description of the factors affecting appearance and severity of spalling is listed below:

- *Maximal temperature* might be one of the most straightforward factors to imagine, as if service temperature stays low, no spalling due to high temperatures will appear. Temperature at the point of spalling is often reported to be in the range between 200 and 300 °C[68,69]. Maximal temperature within the material is a combination of type of fire and duration of the fire, i.e. the thermal load of the fire on the structural element. Temperature level has an important effect on development of transient strains, that become more pronounced at temperatures above 400 °C[70];
- *Heating rate*s set a speed at which the structure has to react to the thermal loads. Very low heating rate (e.g. 0.5 °C/min) will leave enough time for the vapor to evacuate without generating high vapor pressure, however in the real case scenario (as discussed above on examples of standard fire curves), temperature of the gas can exceed 1000 °C in just under 5 minutes (e.g. RABT-ZTV fire curve). At the same time Tao et al. reports no obvious effect of heating rate on transient strain[70]. Same time very slow heating rate can lead to BLEVE phenomena[64]. Moreira et al.

observed increased moisture accumulation ahead of the drying front for samples with higher heating rate[71], this study provides quantitative explanation to the concept of slower heating rates to avoid explosive spalling;

- *Heating profile* is a complex set of time-temperature data, not always it can be predicted or directly described by a single fire curve, as discussed before. Sharp rises and falls of temperature can lead to critical combinations of stress and result in structural instability or spalling. Beside the heat propagation from the surface to the inner parts of the structure, which is a classic case of fire, effort has been done to study the temperature/heating profiles where the peak temperature is reached in the inner part of the structure; this special case can be generated with microwaves[72] and the heating profiles are determined as Power vs Exposure time, defining the effective energy in kW/t;
- *Duration of fire* is one of the key components defining the total produced thermal load. The longer fire can both result in higher temperatures of the gas next to the interface and in overall higher temperatures within the structural elements, increasing probability of spalling due to higher temperatures or a larger time window for the event to occur;
- *Section size* – to the first approximation the larger is the structural element, the higher and more severe spalling can be expected. This has to do both with the total volume within which water will migrate to a colder region of the structure eventually accumulating larger mass leading to vapor clogg and rise of vapor pressure, as well the total way that vapor has to travel in HPC with limited permeability due to a dense structure. Boström performed spalling tests on the plates of 100 mm and 400 mm in thickness, while the weight loss of both plates was comparable, large plates had much higher depth of spalling[73]. This size effect can be associated with both with total volume and with a longer pass for the vapor to complete in the larger plates before releasing the pressure. Another aspect here is the pass for a crack to complete before reaching the colder surface, thus creating an easier escape pass for the vapor. The stress release by a crack that reached the boundaries is higher likely for the smaller samples[74]. Same time, the size of the section directly affects heat capacity of the element affecting the deterioration of mechanical properties[47]. Larger cross sections leads to larger temperature gradients;
- *Shape of the heated elements* is responsible for the concentration of the local stress, while the load bearing capacity can be the same for the elements of different shape. Cross sections of the simpler shape can lead to decrease of spalling; Meyer-Ottens in his PhD Thesis[75] discusses the influence of C-section on spalling and gives examples of additional fire protection installed directly on the concrete beams if C-section cannot be simplified (e.g. it already exists), as well design of the rounded corners for load bearing elements is advised;
- *Moisture content* is an actual volume of water that has to be transferred through the solid matrix in the case of fire. At early age moisture concrete is higher than later as hydration and drying from the surface progresses, thus decreasing this factor of probability of spalling. Paying actual attention to drying of concrete before installation of precast elements is one of strategies to decrease risks[75];

- *Pore pressure* plays a big role in modern theories of spalling, so big that it even describes the whole mechanisms of spalling itself, as discussed above. However, most likely, it is one of the components of actual processes happening and can be just a trigger[63] of spalling, responsible for it's explosivity, severity of an each spalling event. In the case of fire, the pore pressure gradually rises reaching it's peak and same gradually decreases, as the moisture front passes the point of measurements, the bell-shape pressure curve[76] is consistent with spalling mechanisms where pressure plays a role. Du and Zhang[76] reports close connection of pore pressure to strength, compactness and pore structure of concrete and actual spalling;
- *Permeability* is a key factor of pressure build-up and clogg formation; one may say that the lower the permeability of the matrix is, the higher is risk of explosive fire spalling. However, at the same time this has to be balanced with larger mass transfer at higher permeability, thus leading to accumulation of higher vapor volume near the zones where clogg formation may occur;
- *Age of concrete* is a factor that governs many variables that affect spalling. At the early age, moisture content is higher and tensile strength if lower, this should increase probability of spalling, and in general, it is agreed that early age concrete is more prone to spall at high temperatures. However, as concrete ages, denser microstructure is formed with late formation of ettringite and as pozzolanic reaction of supplementary cementitious materials progresses. Denser structure decreases pore neck radius, this is decreasing permeability of the system. Decrease of permeability itself is a factor that increases spalling. With age, spalling time increases, or spalling can be eliminated at all; however, denser structure and later spalling means deeper and much severe single spalling event;
- *Strength of concrete* is the property that should have a major factor of mechanical performance, as spalling is eventually a type of cracking. However, in general, tensile strength of concrete varies less than permeability or types of fire load scenarios, or shapes of structures mentioned before. Scaling down to a single property of tensile strength, the higher tensile strength would mean lower spalling risks. This is valid for the mixes that tend to spall under certain thermal loads and excluding spalling of aggregates. While, despite C20/25 concrete having lower tensile strength than C90/105, it is more likely that spalling will occur for C90/105 concrete, as permeability of C20/25 is much higher. There is no single straightforward property responsible for spalling phenomena. However, it is strength of concrete that is often used as a proxy in simple tests to represent also other microstructural features, e.g. for high strength we expect low permeability and higher spalling. Because strength is governed by the gel/space ratio and permeability too, although, of course, not linearly;
- *Compressive stress and restraint*. Higher stresses during service life of the structure are expected to increase risk and severity of spalling during fire event. Higher initial level of stresses increase transient strains, this correlation becomes more prone at temperatures above 200 °C[70], where the actual spalling happens. Same time permeability of the material is changing under the loads, this was studied by Lu[77] in

his Thesis, where permeability of OC and HPC had a slight decrease under low loads;

- *Type of aggregates*. Performance of aggregates at high temperatures plays significant role in performance of the whole structure. Kodur[78] found that presence of carbonate aggregates increases fire resistance of high strength concrete columns. First studies of spalling were focused on choice of right type of aggregate that would eliminate spalling, while back then spalling of concrete was mostly driven by actual spalling of aggregates due to high temperatures, as mortar part of the concrete had high w/c ratio and had no problems with vapor permeability;
- *Type of fine fillers* affect density and permeability of the whole matrix as some fine powders are pozzolans. Beyond the actual spalling, residual mechanical properties are important for performance of the structure after the fire accident, substitution of silica fume with fine zeolite powder can decrease drop of mechanical properties at the temperatures above 400 °C[79];
- *Aggregate size* affects performance of the structure under fire in number of ways. Lately study showed faster movement of vapor in sample with larger aggregates[80], same time the larger are the aggregates, the larger a single local strains as aggregate expands and can spall itself at high temperatures;
- *Cracks* in concrete influence long-term performance of the structure increasing penetration of water that can bring sulfates, CO_2 and other unfavorable substances that influence condition of the structure negatively, leading to evolution of cracks, decrease of pH and corrosion of reinforcement. However, in the case of fire some cracks can have a beneficial effect on mass transport, as vapor is able to escape from structure faster without generating critical stresses;
- *Reinforcement* and its high thermal conductivity and thermal expansion, with corrosion and physical changes[81] at high temperatures often lead to a spalling pattern following the actual contour of steel reinforcement even for types of concrete mixes that without steel would not spall. At the same time, steel reinforcement can hold together the spalled elements, thus keeping the next layers of concrete protected from direct fire exposure;
- *Cover of reinforcement* is an important factor in the overall good long-term performance of the structure. Close location of the reinforcement to the surface subjected to high temperatures can lead to a very fast spalling, not leaving much of time to put out the fire before damage is done to the structure.
- *Supplementary metal elements* like anchors can cause local spalling around them at early time of fire and become the driving force of the integral cracking[82];
- *Steel fibers* are common in modern concrete. Zheng[54] investigated influence of concentration of steel fibers on stress-strain diagrams of reactive powder concrete. So-called Hot tests were performed, Zheng concluded, that steel fibers cannot increase compressive strength of concrete at high temperatures, however, steel fibers can change failure mode of the samples and increase ductility. Steel fibers decrease severity of spalling, but does not prevent it completely[83]. Layers of concrete that are damaged and without steel fibers would spall away, can be still in place, not contributing to mechanical performance of the structure, however,

protecting deeper layers of concrete from direct exposure to fire. Kodur[78] found combination of steel and polypropylene fibers to improve the ductility of the HSC columns exposed to high temperatures. Lau and Anson[46] report positive effect of steel fibers on compressive strength, both at virgin and residual state. Meanwhile Klingsch[84] found that presence of steel fibers has only minor effect on reduction of spalling. Sultan[27] reports contribution of the steel fibers to increase tensile strength, thou limiting cracking at high temperatures, and Li summarized that addition of steel fibers alone has limited effect on pressure build-up[85];

- *Polypropylene fibers*. As number[56,86–88] of research including this work[69] showed, that polypropylene fibers decreases spalling. In general, melting of fibers increases connectivity of the pores and enhances vapor evacuation and dissipation of vapor pressure;
- *Natural fibers* similar to polypropylene fibers can decrease spalling[89] due to high temperatures, as they create channels for vapor to escape and contributing to relaxation of the stresses. After natural fibers are burned out, connectivity of the pore is increased. Increase of permeability in mixes with natural fibers reduces pressure build-up in the pores at elevated temperatures[85];
- *Air-entrainment agents* (AEA) increase macro porosity of the concrete, generating extra space for vapor to escape thus decreasing the vapor pressure, Akca and Zihnioglu[86] found positive effect of AEA on residual strength of HPC in temperatures below 300 °C. D'Aloia[90] explored effect of AEA testing 10 cm thick slabs subjected to ISO standard fire curve from one side and found positive results. Addition of AEA to a normal strength concrete below 40 MPa is not bringing any new effect as same total porosity can be generated by simple increase of w/c ratio, while AEA is beneficious for higher strength concretes, where w/c ratio has to be kept low[90].

The long list of factors affecting performance of concrete structures under fire indicates complexity of the spalling phenomena and challenges in accurate qualitative prediction of its appearance, and more important, quantitative estimation of the damage. Number of factors are very closely linked and have direct impact on each other; however, they do not mean the same.

A number of key parameters influencing spalling have been singled out and extensively studied[13,70,74]. However, despite the large body of research, predicting the occurrence of spalling has proven to be an elusive task and current explanations of spalling behavior are mostly empirical and qualitative. It is commonly accepted, however, that high moisture content favors the formation of the moisture clog, slowing down the drying front and increasing the temperature gradient[13]. Presence of polypropylene fibers and other fibers that would burn out at high temperatures, increases permeability and moisture transport during fire[69], thus decreasing probability of moisture clog. High heating rate also increases the gradient, while external loads or confinement contribute to increase of the stress[13].

1.4. PREVENTION OF EXPLOSIVE SPALLING IN CONCRETE STRUCTURES

To ensure safety, alongside fire detection, fire extinguishing systems and design of safe evacuation routes, number of methods can be applied to the concrete structure itself to decrease or prevent fire spalling. Some methods can be implemented at the stage of mix design of the concrete or design of geometry and reinforcement of concrete elements; however, this is not applicable to already existing structures. Meanwhile other methods are the only choice left for existing structures where additional protection is required. Methods are summarized below in Table 1.5.

Table 1.5.

Methods to protect from spalling

Approach	Method	Mechanism behind	Comments
Design of elements (limited application on existing structures)	Reinforcement	Physically holds element together, reducing progressive spalling after reinforcement is reached	Reinforcement elements can increase probability of explosive spalling. However, alongside positive examples, appearance of spalling itself often follows pattern of reinforcement.
	Supplementary reinforcement	Supplementary reinforcement can delay exposure of main reinforcement to direct fire. Supplementary reinforcement is applicable to existing structures.	Supplementary reinforcement, that targets integrity of the structure in the case of fire loads and not designed for static loads can limit intensity of progressive spalling and give extra time for evacuation or other safety measures.
	Shape design	Thicker sections reduce spalling damage[10], same time if spalling still appears at a later state, thicker sections can lead to higher depth of a single spalling event[73] as it takes vapor longer distance to escape from the structure. Angularity of the shape increases probability of spalling[75].	Meyer-Ottens suggests to simplify shapes and round up the corners of load bearing elements[75].
Mix composition (not	Polypropylene and other	Detailed mechanism and sub effects are widely	The most popular approach, widely proven by tests. Alongside with

applicable to existing structures)	synthetic polymer fibers	studied now[91–93] and in this thesis[69]. Straightforward mechanism is related to melting polypropylene fibers at high temperatures, thus creating channels for vapor to escape, decreasing chance of moisture clog.	traditional polymer fibers, performance of the recycled products is of interest, e.g. fibers obtained from recycled industrial carpets[50].
	Natural fibers	Similarly as polypropylene fibers, natural fibers burn out at high temperatures[61,89,94]. In addition, natural fibers are permeable to vapor and at higher temperatures shrink due to drying thus creating channels for vapor to escape even before burning out.	Mechanisms are similar to PP fibers.
	Metal and other non-burning fibers	This type of fibers has higher mechanical properties than polymer and natural fibers, they do not directly create channels for vapor to escape by burning out. However, regions along the fibers are still expected to be more vapor permeable and in case of propagation of spalling related cracks, fibers would not allow rapid progressive explosive spalling[83], thus, inner layers of structure would not be exposed to fire directly.	This class of fibers is in different sections as mechanism and results differs from fibers listed above. Sultan[27] discusses difference in spalling prevention mechanisms between steel fibers and PP fibers. Effect of steel fibers on fire spalling is unclear, in general delay and decrease of the spalling is reported, however, not an effective prevention of the spalling event.
	Air-entraining agent (AEA)	Larger pore volume is available for the same amount of vapor, thus alleviating vapor pressure.	Coupled effect of AEA and PP fibers is studied by Akca and Zihnioğlu[86], where AEA decreased spalling of samples with lower content of PP fibers. Samples with the same load of PP fibers

			and no AEA spalled under designed conditions.
	SAP	Similarly to air-entraining agent, voids created by SAP decrease saturation of pores, thus alleviating vapor pressure. SAP in combination with PP fibers can reduce or eliminate spalling, where mechanism is based on percolation of voids created by empty SAP and melted PP fibers[69,95].	At early age, presence of SAP can lead to a higher moisture content, resulting in spalling[69].
	Choice of aggregates	The lower is thermal expansion of aggregates, the lower are generated stresses and likelihood of spalling.	
State of structure	Moisture control	The higher is moisture content, the higher is probability of moisture clogs and vice versa.	
	Control of stress generated by loads	Load generated stresses increases rate of spalling[62],	
Physical protection	Thermal barriers	Use of thermal barriers is one of few solutions that can be applied to existing structures. Thermal barriers will protect concrete structures from direct and sudden action of fire. Delay propagation of temperatures and smooth temperature profile, resulting in more uniform thermal expansion.	
	Cement based renders	Cement based renders can delay or eliminate[96] spalling, similarly as other thermal barriers.	Cement based renders are compatible with a main concrete structure and can be

			applied directly on the concrete, e.g. spray concrete.

1.5.SUMMARY

Review of the topic presented above highlights the complexity of the problem both from point of view of the material and of the structural elements, multiplied by the fire conditions.

The actual fire tests of large-scale structures are very challenging for interpretation, beside obvious spalling/no-spalling visual observation, and very expensive. However, the possible damage caused to structure justifies the research efforts

The data summarized from the literature indicates:

- Deterioration of mechanical properties at high temperatures;
- Risk to integrity of the structure due to explosive spalling;
- Complexity of physical and chemical changes that concrete undergoes in extreme temperature conditions;
- Challenges in accessing the actual real time state of material due to complexity and safety challenges during the hot tests;
- Combination of boundary conditions and the actual fire scenario can be very unpredictable;
- Explosive spalling of concrete due to fire is not a property of material, but rather complex combination of factors strongly linked with each other;
- Various protection methods to limit or exclude occurrence of explosive fire spalling, where layers of fire protection material is a common solution for existing structures and addition of natural and PP fibers has proved its performance for new structures.

While the general deterioration of mechanical properties is widely described in literature and are obvious when are summarized down to a single static measurement, the non-linear properties (e.g. dynamic Young's modulus) and mass transfer other than temperature is rarely studied. One must look for methods outside of those that are common for construction materials, that leads to the goal of the Thesis: to validate complex non-destructive measuring technics from other fields to evaluate thermal damage of concrete. First, one must validate the thermal damage with common methods to prove that the materials and conditions used in this work are comparable to state of art from literature and then to expand the evaluation of thermal damage and processes to a methods widely used in other fields.

2. MATERIALS AND MIX COMPOSITIONS AS OBJECTS OF THIS STUDY

2.1. MATERIALS

Work described in this study focuses on evaluation of effect of high temperatures on microstructure of concrete with Portland cement as a binder, and applicability of different methods to investigate changes that concrete overcomes due to thermal loading.

To decrease uncertainty stemming from the complex composition of the blended binders, I chose ordinary Portland cement Jura CEM I 52.5 R. The oxide composition of cement is presented in Table 2.1 below.

Table 2.1.

Oxide composition of Jura CEM I 52.5 R

Oxide composition	mass-%
SiO_2	19.64
Al_2O_3	5.26
Fe_2O_3	3.13
Cr_2O_3	0.009
MnO	0.057
TiO_2	0.290
P_2O_5	0.179
CaO	63.18
MgO	2.00
K_2O	1.01
Na_2O	0.16
SO_3	2.94
L.O.I.	1.87
total	99.72

L.O.I. - loss on ignition

Deionized water was used for mixing, to exclude traces of materials not related to this study. Locally widely available alluvial sand and gravel were used as aggregates. With aggregate sizes 0-1, 1-4, 4-8 and 8-16 mm, granulometric curves are given below in Figure 2.1. and compared to requirements of SN 670.

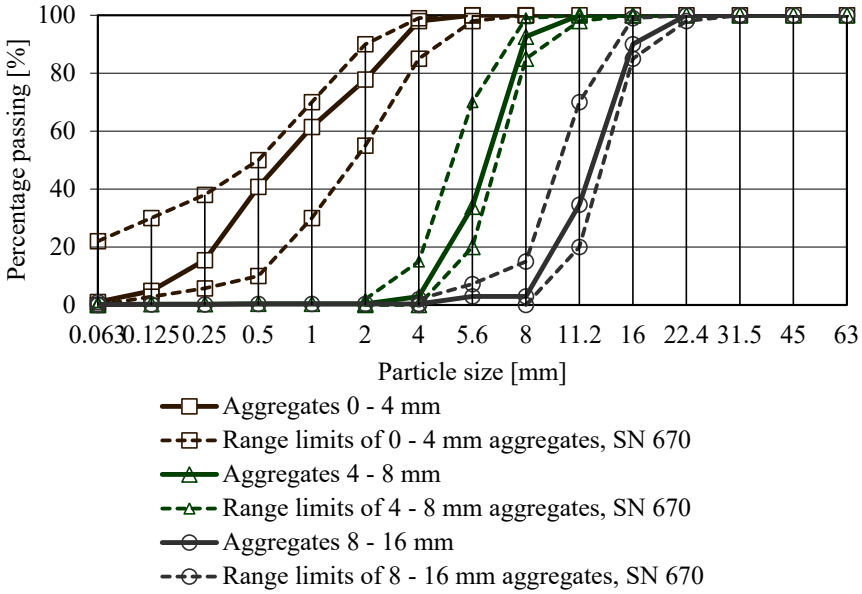

Figure 2.1. Granulometry of aggregates.

To obtain denser and well-packed structure, Silica fume Elkem U968 was used. To reduce w/c ratio and maintain good workability, polycarboxylate based Superplasticizer Sika-56 was used. Polypropylene fibers Fibermesh 150-3 from Propex with specific gravity 0.91 and fiber length of 3 mm were used. Melting point of Fibermesh 150-3 is 162 °C, temperature of ignition 593 °C. SAP VP300 from BASF was used to ensure internal curing[97] of HPC samples.

2.2.MIX COMPOSITIONS

As described above, phenomena of explosive spalling occur in dense and less permeable concrete, like High Performance and Ultra-High Performance Concrete (HPC and UHPC). To evaluate, which combination of properties leads to spalling and which does not, we need both: a mix that would spall virtually always and a mix that would virtually never spall under the same conditions. Both should have practical application and reasonable strength properties, to have potentially wide use in load bearing structures. Most mix formulations are mortars with maximal aggregate size up to 4mm. This limit was set to be able to perform microstructural studies with different methods on samples from the same mix as samples used to determine mechanical properties and sensitivity to spalling.

In this study, I have chosen concrete with 370 kg of cement per m^3 and water to cement ratio of 0.5 to represent ordinary concrete (OC) which is not expected to spall under chosen protocol of thermal loading.

As concrete that is expected to spall, I have chosen HPC with rather low amount of cement and Silica fume to keep it realistic to currently used typical industrial HPC mixes, with 488 kg of cement per m3 of concrete and w/c ratio at 0.31, this mix is designated as HPC-ref.

Wide number of studies[61,87,89,91,92,98–101] report that different fibers can affect occurrence and severity of the spalling, the most popular type of fibers to reduce explosive spalling are polypropylene fibers. Polypropylene fibers were added to previously developed HPC mix and amount of superplasticizer was adjusted to achieve the same workability as reference HPC mix, this mix is designated as HPC+PP.

Alongside explosive spalling under fire, HPC is also known for stresses induced by self-desiccation, which can lead to severe cracking and thus significantly lower performance of material. To control autogenous shrinkage of HPC and severe cracking as result, internal curing by superabsorbent polymers (SAP) is used[97]. Self-desiccation that occur in low w/c concrete leads to another problem, that is increase in coefficient of thermal expansion at early age, SAP are also able to control increase in CTE[102]. To solve issues mentioned above, SAP were added to HPC-ref mix, adjusting amount of superplasticizer and water. This mix is designated as HPC+SAP.

In the mix design of the HPC mixes with SAP, extra water is introduced to compensate for SAP sorption[103,104], this water is later used for internal curing of cement paste, thus, volume, previously occupied by saturated SAP particles empties with time. In case of fire, this volume, when it is free of liquid, becomes available to accumulate vapor and decrease vapor pressure, as the volume of a given amount of gas is proportional to temperature-to-pressure ratio, if total amount of vapor and temperature gradient is the same as in system without SAP. However, at early age, use of SAP leads to increase of total amount of water in the volume of concrete. Higher content of water with the same permeability of the concrete would increase amount of water vapor to transfer through the matrix in case of thermal loads, this would increase probability of vapor clog[4,59] and induce explosive spalling phenomena. At later age, formation of hydration products is observed within voids.

Combination of both, SAP and polypropylene fibers is described by Lura and Terrasi[95], this study reports, that percolation of emptied voids created by SAP with PP fibers decreased spalling. To study this effect, it's influence on structure of material and mechanical properties after exposure to a range of temperatures up to 600 °C, concrete mix both with SAP and PP fibers was designed based on HPC-ref and adjusted for workability, corresponding mix is designated as HPC+PP+SAP.

Most of the study described in this thesis was performed on mortars. To link results described here to more common concretes with larger aggregates, HPC_16mm mix was designed. Where total volume of paste and its w/c ratio was the same as in all HPC mixes, but granulometry of filler was adjusted to include aggregates up to 16 mm. HPC-ref and HPC_16mm mixes were compared by matter of Oxygen diffusion to describe transport properties, and by spalling/no-spalling evaluation designed and described below.

All the mixes are presented in Table 2.2 below.

Table 2.2.

Mix compositions investigated in this study

Mortar type	OC	HPC-ref	HPC+PP	HPC+SAP	HPC+PP+SAP	HPC_16mm
Cement CEM I 52.5 R	370	488	488	464	464	488
Silica fume	0	122	122	116	116	122
Aggregates 0-1mm	740	633	633	633	633	253
Aggregate 1-4 mm	1110	949	949	949	949	380
Aggregates 4-8	0	0	0	0	0	396
Aggregates 8-16mm	0	0	0	0	0	554
Superplasticizer	5.18	8.54	8.54	8.12	14.5	8.54
PP fibers	0	0	2	0	2	0
SAP	0	0	0	1.93	1.93	0
Water	185	189.1	189.1	197.2	197.2	189.1
w/b total	0.5	0.31	0.31	0.34	0.34	0.31

As you can see from the table above, the amount of aggregates was kept the same for all HPC mixes, however mass of cement per m^3 is changing. This is due to increase in total water volume, to keep the total volume of aggregates and volume of paste the same. This ratio ensures compatibility in volumes that govern mass transport, e.g. aggregates and paste.

2.3. EVALUATION OF MIXES BY SPALLING/NO-SPALLING CRITERIA

In order to study explosive spalling of concrete and investigate evolution of properties over age and temperatures, here one has to ensure that mix compositions presented above in Table 2.2 would include both, spalling and no-spalling performance. Where OC mix should not spall, HPC-ref mix would spall. Next, by adding spalling preventive additives to the original HPC-ref mix, new mixes would be obtained that experience less sever or no spalling (HPC+PP, HPC+SAP and HPC+PP+SAP).

There are different approaches to report severity of spalling. The most common are to report area of spalling, mass of lost fragments and depth. However, it is difficult to limit explosive spalling to a single spalling event, when external layer of concrete is removed by spalling, next layers of material are directly subjected to the source of heat. In laboratory environment one can remove the source of heat after first spalling, however, here we must consider the safety issues as even with no additional generated heat, the sample is still at high temperatures and mass transfer of heat and vapor is in progress. Thus, another event of explosive spalling is possible.

Samples to evaluate fire-spalling performance

Samples of two geometries were cast to evaluate fire-spalling performance of the mixes: two cubes of 150 × 150 × 150 mm^3 and one plate sample of 25 × 100 × 100 mm^3 for each mix except HPC_16mm, where only cubes were produced. While standard cube samples are more

often used in studies of concrete, plates with thickness of 25 mm were additionally tested to complement neutron radiography study described in part 4.1 of this Thesis. Mortars were cast in steel moulds on a vibrating table during 2 minutes. After casting, samples were cured at >95%RH and 20 ± 0.3 °C for 1 day, at which age they were demoulded and stored in the same climatic room until the day of testing.

Alongside with evaluation of spalling performance, evolution of temperature front from one–sided heating was measured. K-type thermocouples were welded and fixed in steel moulds before casting to ensure a fixed position of the temperature-measuring tips in the hardened samples. Welding of thermocouples allows to ensure that the measurement is produced at a single point over the testing time and allows to limit risk of oxidation affecting the measurement. The exact position of thermocouple during spalling/no-spalling campaign is assumed as where they were installed before casting, while during the Neutron radiography tests described later in this Thesis, the position of the thermocouples was controlled by additional x-ray radiography, this allowed to visualize the welding point and significantly increase the precision of the temperature fronts.

Methods to evaluate fire-spalling performance

To decrease temperature and moisture exchange boundary effects of the samples and hence simulate a larger volume of concrete, both cubes and plates were insulated with a thermal and moisture insulation, respectively. To this end, a self-adhesive aluminum tape was glued from all sides but the heated one in direct contact with heating plate. The lateral sides were next insulated from the heat loss with 2-3 cm thick plates of temperature-resistant foam glass. In general, insulation is similar to one described in neutron radiography tests[69], to minimize the difference.

Samples were placed on a heating device with non-insulated side down, in direct contact with the heating plate. Wires of thermocouples were placed between thermal insulation and vapor insulation, fixed on the top of the samples and away from the heating plate to exclude any direct contact with the heating plate. Metal cage with extra weight on the top was placed on the heating plate to shield the sample and protect environment (e.g. equipment like electric controller plate and the user) in case of spalling.

The thermal load protocol was as follows: an increase from room temperature to the maximal temperature of 600 °C in 30 minutes and a temperature plateau at 600 °C for two hours, followed by a free cooling down (see Figure 2.2). The tests were performed either till protocol of thermal load was executed or until first significant explosive thermal spalling. As often explosive spalling would cause change of boundary conditions, moving the sample and losing proper contact with the heating plate or as for the plate samples, they would fall on the side, causing a total loss of contact with the heating plate.

During the test, temperature fronts were followed with K-type thermocouples and video data recorded to follow severity of spalling and time of spalling. Here I define spalling time as a case of spalling that moved the sample from its initial position (e.g. full explosion, a jump, a fall on a side), as definition of spalling by recorded sound is less clear, insignificant "popcorn popping" sound can be produced both by equipment and damage of thermal insulation foam glass plates.

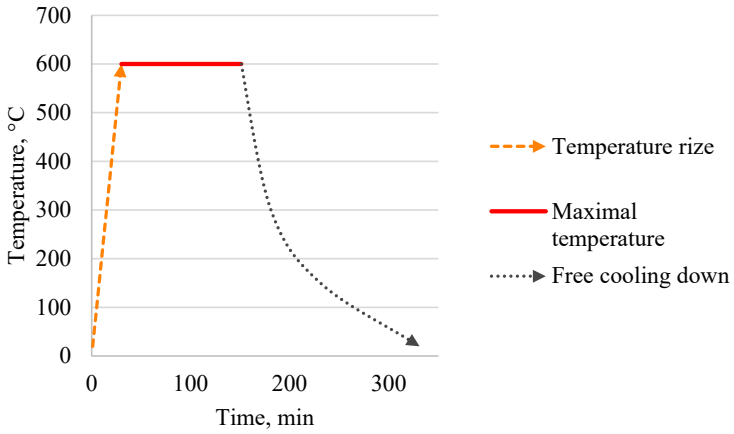

Figure 2.2. Temperature protocol of heating plate.

Results of fire-spalling performance

Results are summarized as spalling/no-spalling in Table 2.3, where C corresponds to Cubes; P – plates. Number next to sample indications corresponds to number of samples where spalling was observed, out of total number of samples tested, e.g. 0/2 means that no samples spalled out of 2 samples tested, 2/2 means that spalling was observed on 2 out of 2 samples.

Table 2.3.

Summary of spalling tests

Age	OC	HPC-ref	HPC+PP	HPC+SAP	HPC+PP+SAP	HPC_16mm
1d	C 0/2; P 0/1	C 2/2; P 1/1	C 0/2; P 0/1	C 2/2; P 1/1	C 2/2; P 0/1	C 2/2
3d	C 0/2; P 0/1	C 2/2; P 1/1	C 0/2; P 0/1	C 2/2; P 1/1	C 0[1]/2; P 0/1	C 2/2
7d	C 0/2; P 0/1	C 2/2; P 1/1	C 0/2; P 0/1	C 2/2; P 1/1	C 1/2; P 0/1	C 2/2
21d	C 0/2; P 0/1	C 2/2; P 1/1	C 0/2; P 0/1	C 2/2; P 1/1	C 0/2; P 0/1	C 2/2
28d	C 0/2; P 0/1	C 2/2; P 1/1	C 0/2; P 0/1	C 2/2; P 1/1	C 0/2; P 0/1	C 2/2
35d	C 0/2; P 0/1	C 2/2; P 1/1	C 0/2; P 0/1	C 2/2; P 1/1	C 0/2; P 0/1	C 2/2

Alongside with a general evaluation of spalling/no-spalling criteria, time of spalling was recorded. Effect of size of the samples, where time of spalling of HPC+SAP 150×150×150 mm3 cubes is compared to smaller plates of the same mix is presented in Figure 2.3. Figure 2.4

[1] One of cube specimens spalled 30 minutes after end of thermal loading, out of assumed test time.

visualizes time of spalling as average of two samples for HPC-ref and HPC_16mm large cubes over age, from 1 to 35 days.

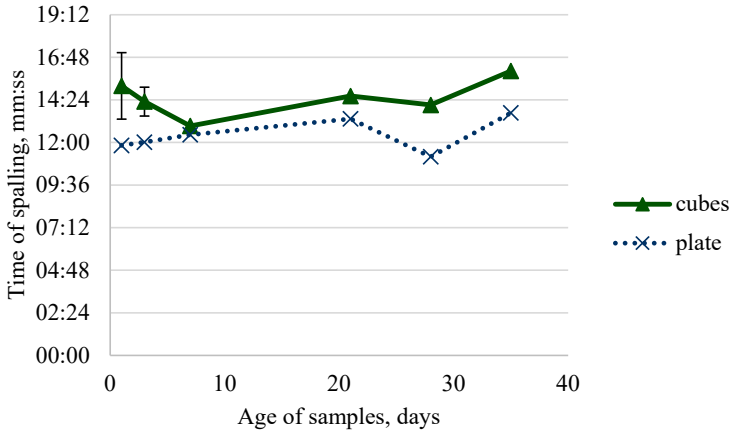

Figure 2.3. Time of spalling of HPC+SAP samples, size effect.

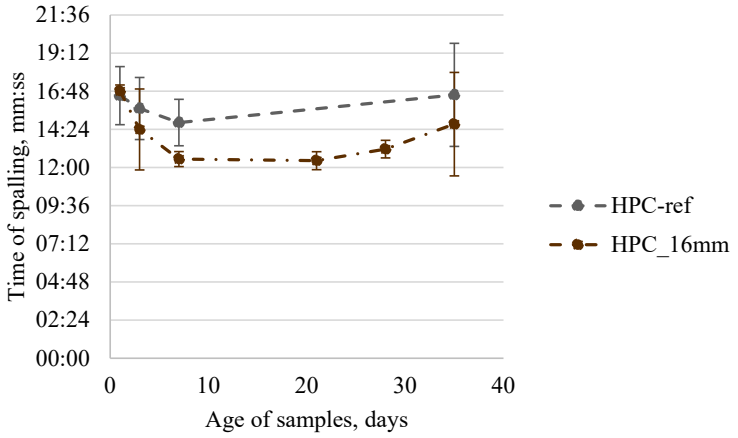

Figure 2.4. Time of spalling depending on the size of aggregates over age.

Introduction of SAP to HPC mix comes along with higher volume of water and decrease of spalling time, see Figure 2.5, where spalling time over age is presented for cubical samples.

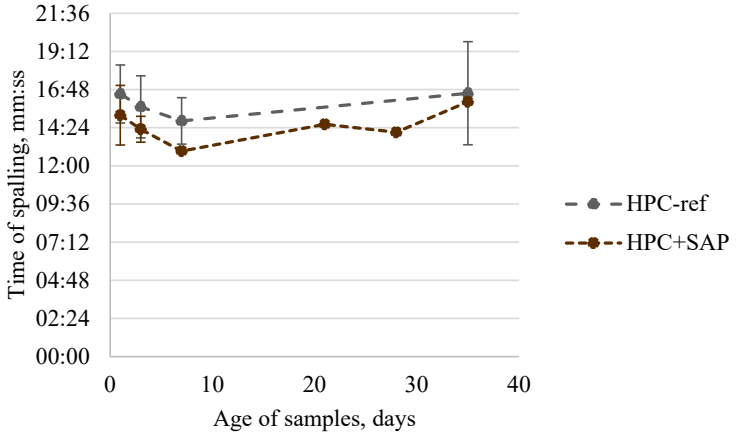

Figure 2.5. Effect of SAP on time of spalling over age.

One out of two cube samples and each plate sample had 4 K-type thermocouples installed and temperature fronts were recorded at depth of 5, 15, 25 and 35 mm from the surface subjected to high temperature. Temperature fronts recorded for HPC-ref samples at the age of 7 days are presented below, where Figure 2.6 represents the larger cube specimen and Figure 2.7 are temperature fronts of corresponding plate specimen.

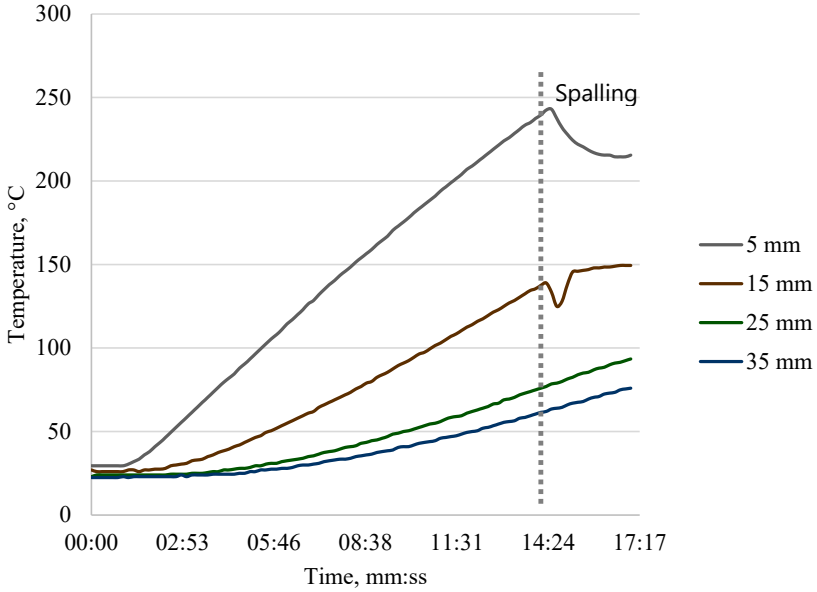

Figure 2.6. Temperature fronts of HPC-ref 7d cube sample.

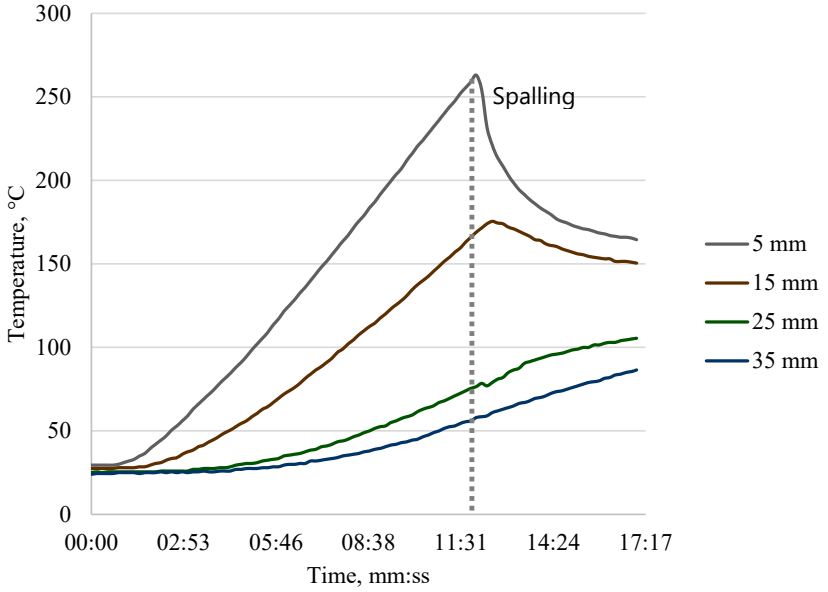

Figure 2.7. Temperature fronts of HPC-ref 7d plate sample.

Discussion

While preparing mix designs for this study, it was important to produce OC mix that would have no spalling and HPC-ref mix that would have spalling behavior under thermal loads. As it is seen from Table 2.3, proposed designs follow this criterion. Use of polypropylene fibers eliminates spalling for HPC+PP mixes under designed test conditions in all the cases, in line with results of other studies[87,89,105].

It was of interest to obtain a mix design that would spall at early age and spalling behavior would not be there at later ages due to development of microstructure and consumption of water, mix design HPC+PP+SAP satisfies this criterion. Spalling was still observed on larger cube samples at 1, 3 and 7 days of age, but no spalling damage at 21, 28 and 35 days of age.

Spalling was observed for all samples of HPC+SAP mix under designed test conditions, this is likely due to higher water content in the samples.

Spalling was observed for all HPC_16 mm samples similar as for HPC-ref, thus linking results obtained in this study to behavior of similar mixes with larger aggregates that are more common in use by industry. Recent study on HPC-ref mix under similar conditions of thermal loading (setting of thermal loading were chosen to complement results described in this Thesis) evaluates effect of aggregate grain size on moisture transport, it shows that larger grains increase mass transfer of moisture[80]. Increased transport can both lead to decrease of spalling risks, as will be described below in details[69], and earlier spalling, as indicated in Figure 2.4 and explained by in-situ tests[80] done on very same HPC-ref mix and intermediate step to HPC-16mm mix; which is limiting maximal size of aggregates to 8 mm instead of 16 mm. Which was a compromise between maximal grain size and maximal thickness of the sample that neutron beam could penetrate with reasonable quality.

In general, spalling of smaller plate samples was observed less often than spalling on the larger cubes of the same mix (see Table 2.3). At the same time, as seen from, if both geometries experienced spalling, spalling of the smaller sample would always occur earlier than spalling of corresponding larger samples (see Table 2.3 and Figure 2.3). Figure 2.6 and Figure 2.7 highlights both earlier spalling of plate samples and faster propagation of high temperatures into deeper regions of the sample that can be an explanation, as less of "buffer zones" are available in the smaller samples. Another explanation of difference in temperature rise can be linked to a contact quality with a heating plate, as smaller samples have lower contact area and thus are more subject to possible surface/boundaries defects.

Earlier spalling presented in Figure 2.5 cannot be explained alone by the higher volumetric content of water compared to HPC-ref, as OC mix has even higher volumetric content of water and no spalling was observed. Similar earlier spalling is presented in Figure 2.4, which is driven by the larger size of aggregates in HPC_16mm mix compared to HPC-ref that can be associated to higher transport properties[80]. In general, the use of PP[92,99] and natural[61] fibers decrease the probability of spalling, most likely due to the increase of transport properties[69]. Increase of transport properties can lead to moisture clogs, as large volumes of vapor are transferred faster to a colder region. This has to be even more prominent, when higher local volume of water was there initially, as in case of HPC+SAP samples.

Another important result highlighted by temperature fronts (Figure 2.6 and Figure 2.7) is behavior of samples after spalling. In both cases, sudden drop of temperature was observed at the time instant of spalling, however, for a larger sample temperatures inside the bulk volume continue to rise at two thermocouples that are positioned deeper in the sample (25 and 35 mm). This type of behavior can lead to a series of severe spalling events even when the initial source of heat is not delivering anymore heat, similar as the spalling reported in Table 2.3 of this study and by Zhu[96], where spalling occurred at the end of the designed 2 hour test protocol.

3. EFFECT OF ELEVATED TEMPERATURES ON PROPERTIES AND MICROSTRUCTURE OF CONCRETE

3.1. INTRODUCTION

In the previous part, the results of concrete exposed to high temperatures from one side are summarized as simple spalling/non-spalling criteria. Here, the complexity of the processes resulting in either spalling or non-spalling is tracked through the changes in properties and microstructure of material after exposure to elevated temperatures. As mentioned in Part 1.2, due to safety reasons and to acquire a wide range of data on unified set of materials, the residual state is investigated. This enables me to deliver new insight into the fundamental mechanisms of fire spalling. The data provided below was partially used to improve a numerical model describing behavior of concrete exposed to high temperatures[106].

Rate of temperature increase was approximately 16 °C/min. The reason for the fixed heating rate in the oven is to bring it to the same heating rate as heating plate used for spalling/no-spalling evaluation and neutron radiography study that is described below in part 4.1. This way all the data is more uniform and compatible.

3.2. METHODS

Mechanical properties

The mechanical properties of the mortars were determined on 40 × 40 × 160 mm^3 prismatic specimens. The mortars were cast in steel moulds on a vibrating table during 2 minutes. After casting, samples were cured at >95 %RH and 20 ± 0.3 °C for 1 day, at which age they were demoulded and stored in the same climatic room until the day of testing or thermal loading.

Thermal loading was performed at the age of 28 days, by bringing the specimens to temperatures of 120 °C, 200 °C, 400 °C and 600 °C, followed by 8 h at the maximum temperature and then free cooling down in the furnace.

Young's modulus, flexural strength and compressive strength were determined at the ages of 1, 3, 7, 21, 28 and 35 days on samples stored in parallel at room temperature (further referred to as the virgin state). The static Young's modulus in compression was determined on two separate samples, using a procedure based on the Swiss standard SIA 262-1 (similar to the European EN 12390-13 standard), with the compressive load equal to 25 % of compressive strength; two extensometers were used to measure the displacement while the sample underwent the loading cycles. The procedure for strength measurements was based on the European standard EN 196-1. The flexural strength was measured on three prismatic samples, while the compressive strength was measured on the six half-prisms that were the result of the bending tests, on which the load was applied on a 40 × 40 mm^2 area. Results are summarized in part 3.3.

To determine compressive strength, a hydraulic testing machine D-300-D designed by Walter + Bai AG with the maximal load of 300 kN was used, with the loading speed of 1.5 MPa/s. To determine flexural strength, the 10 PBZ 1106 hydraulic loading machine designed by Empa was used, with the maximal load of 10 kN and loading speed of 0.05 kN/s. The electrically driven DIGIWIN 2000 universal testing machine with the maximal load of

50 kN was used to determine modulus of elasticity. Preload of 0.250 kN was used to fix the sample in the testing machine before adjusting the extensometers. After that, the samples went through three loading-unloading cycles with loading rate of 0.6 MPa/s, where the third loading cycle was the actual measurement.

Hydration and dehydration of concrete (TGA)

In order to study initial bound water content and dehydration at high temperatures thermogravimetric analysis (TGA) tests were performed. Samples of all mortar mixes (Table 2.2) were tested at 1, 3, 7, 21, 28 and 35 days of age. In addition, as described above, measurements were performed on samples that underwent thermal treatment at 28 days of age at temperatures 120 °C, 200 °C, 400 °C and 600 °C for 8 hours at maximal temperature with rate of heat 16 °C/min and free cooling down.

Samples for TGA were mixed in Hobart N50 mixer and cast alongside with MIP samples in 50 ml plastic containers. Containers were sealed and stored in climatic chamber with controlled conditions of 97 %RH and temperature of 20 °C up to a chosen ages when they were demoulded and crushed in smaller chunks of 5 – 10 mm. Thermal treatment was performed on chunks to ensure that whole volume of sample reaches designed temperature. Stop of hydration was performed with solvent replacement method[107,108] on both, thermally treated samples and samples at a certain age in virgin state.

In addition, to evaluate possible re-hydration of specimens (possibly accelerated at elevated temperatures) during cooling down and before final sample preparation, three samples of HPC-ref were taken out of the furnace at the end of maximal temperature and manually ground into powder using pestle. No significant difference in TGA results was observed compared to free cooling regime, which allows to assume that no significant further hydration took place upon cooling down. This was most likely due to the dry conditions maintained in the oven

Stop of hydration was performed for TGA and MIP specimens; it was important not to cause additional damage to MIP samples and to empty pore structure from water. Collier[108] provides comparison of water removal techniques for cement pastes and describes their effect on microstructure. He found solvent replacement method suitable for both MIP and TGA samples.

Equipment to prepare TGA samples is seen in Figure 3.1. Where mortar and pestle (A) are used to grind chunks of material into fine powder, GVS Magna nylon membrane filters Ø 47 mm and NY 0.45 μm (B) are placed in column (C). About 1 g of grinded material is placed in filtration column and flashed with isopropanol (E) for 10 minutes. Isopropanol is removed by filtration under vacuum produced by vacuum pump (F). Leftovers of isopropanol are flushed with ether (D). Two cycles of solvent exchange using isopropanol and flushing with ether were performed. To remove traces of ether, samples were subjected to drying for 15 - 20 minutes at 40 °C.

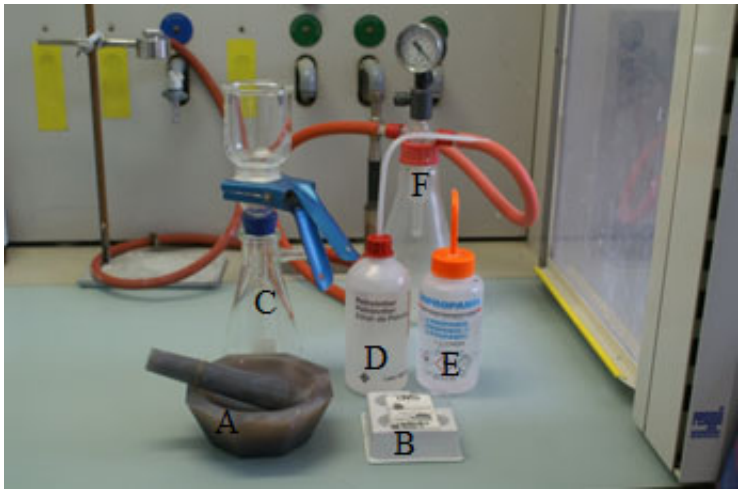

Figure 3.1 Equipment to stop hydration of TGA samples

Thermogravimetric analysis was performed on powder samples of about 50 mg with Mettler Toledo TGA/SDTA851 setup, monitoring the weight while heating up from 30 °C to 980 °C at 20 °C/min and purging with N_2. Data was processed to DTA and peaks from derivative curves are presented and compared in Part 3.3.

As for verification of chosen test protocols, both for TGA measurements described above and MIP measurements that are described in the following chapter, here I want to mention the effect that was observed for thermally treated samples prepared for mechanical properties.

Samples to obtain mechanical properties and for TGA and MIP were thermally treated at the age of 28 days for 8 hours at maximal temperatures, however, different volumes were subjected to high temperatures. In the case of mechanical properties, I used 40 × 40 × 160 mm^3 prismatic specimens and for TGA and MIP – chunks of materials 5-10 mm in size. As mentioned before, motivation to perform TGA and MIP on chunks was to ensure that the whole volume of sample reaches designed maximal temperature. As seen from Figure 3.2, when thermal loading was performed on larger samples, gradient of moisture formed. This particular sample seen on Figure 3.2 is HPC+SAP sample treated at 120 °C after 3-point bending test. Darker region in the center and lighter contour on outer part indicates higher water content in the central part of the sample. 3-point bending tests is followed by testing same halves in compression (procedure is described above and results are presented in 3.3). To evaluate the effect of higher moisture content in the center, after testing mechanical properties, chunks of material were taken from inner and outer part of the sample. After grinding and solvent exchange, TGA was carried out. Because solvent replacement method eliminates possible "free" water, thus, difference in color seen in Figure 3.2 will be evaluated only from point of view of difference in hydration products.

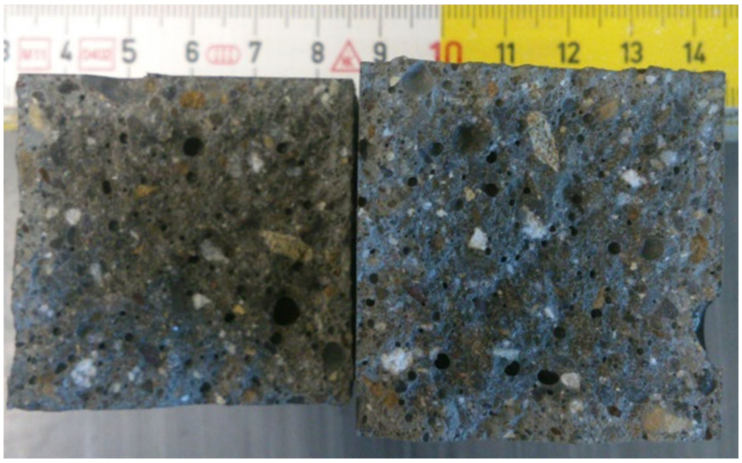

Figure 3.2 Cross-section of HPC+SAP sample thermally treated at 120 °C, right after 3-point bending test.

Results of TGA are presented in Figure 3.3, as seen, mortar samples from inner part of 40 × 40 × 160 mm^3 prismatic specimen had by 0.5 % (from total mass of the sample) more bound water than outer part of the same specimen. This particular data is valid only for HPC+SAP sample at 28 days of age, treated at 120 °C for 8 hours with free cooling down, however, both Figure 3.2 and Figure 3.3 represents size effect and the reason behind performing TGA and MIP on chunks that underwent thermal treatment and not larger specimens. Each curve presented in Figure 3.3 is an average of 3 separate measurements. As long as TGA study is performed on mortar samples, this decreases the effect of cherry-picking, as one or another sample could contain more or less of aggregates. While only 50 mg of sample is used for an actual TGA test, about 2-3 grams are grinded initially. Each sample is from separate grinding as well.

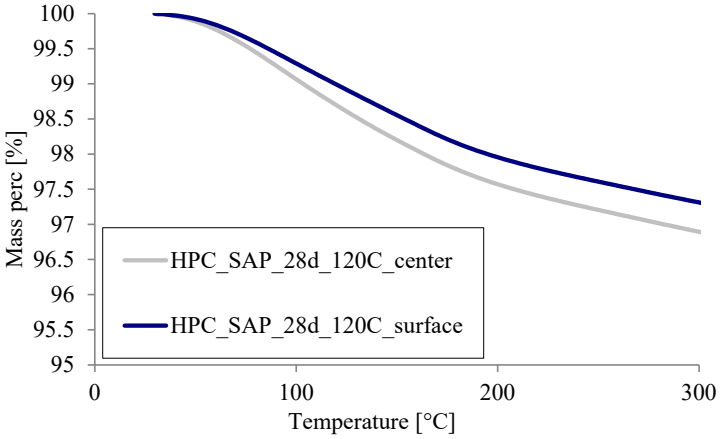

Figure 3.3. Comparison of TGA curves of inner and outer part of larger sample.

Effect of temperature on pore structure

Limitations of Mercury Intrusion Porosimetry (MIP) measurements to quantify the actual pore size distribution of cementitious materials were discussed by Diamond[109]. To overcome some of these limitations, Kaufmann et al. [110] developed multi-cycle MIP, which allows estimating the volume of ink-bottle pores. The first intrusion of mercury allows resolving the total porosity (therefore, both interconnected matrix and ink-bottle porosity) and as an outcome the total porosity volume is obtained as a function of the equivalent sizes of pore entrances [110]. After extrusion of mercury, all ink-bottle pores are assumed to remain filled with mercury. Consequently, in the second cycle, only the interconnected porosity is resolved.

In this study, multi-cycle MIP was performed on specimens of ages 3, 7 and 28 days, with or without thermal loading. Samples were cast in 50 ml plastic containers alongside with TGA samples, sealed and stayed closed in climatic chamber with controlled 97 %RH and 20 ± 0.3 °C temperature up to a certain age (3, 7 and 28 days of age) when they were demoulded and crushed in smaller pieces of 5 - 10 mm. To stop hydration and remove the water from the pore structure before the MIP measurements, samples were subjected to solvent replacement[108] by isopropanol for 2 days (corresponding chunks of mortars were placed into plastic containers and fully immerged in isopropanol). Containers were sealed and placed in laboratory fume cupboard for safety. This procedure was followed by drying in the ventilated oven at 50 °C for another 2 days. The solvent exchange technique is less damaging to the pore structure compared to direct drying [108].

To evaluate the effect of thermal loading on porosity, similarly to procedure described above, 50 ml samples were demoulded at 28 days and crushed, corresponding chunks were subjected to designed thermal loads at 120 °C, 200 °C, 400 °C and 600 °C. Thermal loading was performed on already crushed samples instead of samples of larger size (50 ml cylinders) right after demoulding, to eliminate thermal gradients, moisture clog and pressure buildup in larger samples. Thus exposing all volume of material to similar thermal conditions, resulting in residual state of material, excluding size effect.

Despite this range of temperatures would already ensure pores free of liquid and even dehydration of material, after samples cooled down, they still follow the same procedure of solvent exchange described above (2 days in isopropanol followed by 2 days of drying at 50 °C), to ensure similar sample preparation procedure.

Each test was carried out on about 1 g of mortar cut with pincers into small pieces of about 2 – 3 mm, 0.1 – 0.15 g each. The sample holder containing a sample was first filled with mercury at pressures up to 200 kPa in a low-pressure porosimeter (Pascal 140 by Thermo Fisher Scientific Inc.). At this pressure range, the mercury filled mainly the intergranular spaces. The sample was then moved to a high-pressure porosimeter (Pascal 440) and two intrusion-extrusion cycles were performed at pressures up to 200 MPa.

The raw data from mercury intrusion (volume of mercury versus applied pressure) was analyzed using the Washburn equation[111] for cylindrical pores to convert it into the equivalent pore size distribution. A surface tension of the mercury of 0.48 N/m^2 and a contact angle of 130 ° were assumed in the calculations. Correction for density of mercury depending on temperature at measurement was considered to calculate volumes. Important to notice, that temperature at the start of the test was used to calculate the density and it was assumed for the

whole test. The temperature of the mercury was not measured directly; instead, temperature of the room during the test was used for correction.

Before the measurement campaign, I performed blank runs on all the dilatometers used. The blanks provide the system reaction on the increasing pressure. The blank run results in blank curve used to correct the penetrated mercury volume in the sample. Similarly to the raw data of the samples, blanks are expressed in volume versus pressure data. To consider the temperature effect due to pressurization, the blanks were performed at the same pressurization speed as used for samples, same for decrease of the pressure. Decrease of pressure, i.e. extrusion, was performed at 50% higher speed than intrusion.

To quantify the differences in the pore size distribution between the different mortars before and after thermal loading, besides the total porosity also the breakthrough pore radius is analyzed. The breakthrough pore radius represents the minimum radius of pores that are percolated through the whole microstructure[112] and it has been related to transport properties of cementitious materials[113]. The breakthrough radius is found as the radius at which a sudden increase in intruded mercury volume is observed and it can be conveniently identified as the first peak on the differential pore size distribution. Results are summarized in section 3.3.

Effect of temperature on transport properties

Spalling of concrete is related to mass transfer properties in concrete structures, alongside transfer of temperature and liquids, phenomena of moisture clog is caused by condensation of water vapor when large amount cannot be transferred through concrete matrix fast enough and vapor accumulates in pores causing pressure increase, that leads to condensation. All the mixes from Table 2.2 were tested for gas transport properties using oxygen diffusion method[114,115]. In interlaboratory study[114], comparison between oxygen diffusion and oxygen permeability was presented.

The oxygen diffusivity was measured using an instrument originally developed by Lawrence [116]. The test device is designed to work based on difference in the gas concentration across the sample. The test uses oxygen on one side of the sample and nitrogen on the other. The gases are kept at constant temperature and pressure, and the system is assumed to be in a steady state condition. To ensure similar conditions for different samples, the whole setup is in the room with controlled climatic conditions, 20 ± 0.3 °C. Oxygen and nitrogen were chosen as the gases used in this test mainly because they are practically inert with respect to the hydration products [117]. The oxygen diffusion setups is described in detail elsewhere [114–117]. The result of these measurements is an oxygen diffusion coefficient DO2 [m^2/s]. To compare different samples after thermal treatment and a general trend, the raw data is processed and presented as relative residual oxygen diffusion, whereas a reference value (1) I chose the oxygen diffusion coefficient of corresponding mix at virgin state, at nominal age of 28 days.

For the oxygen diffusion measurements, 150 × 150 × 150 mm^3 cubes were cast, demolded at the age of 1 day and stored until the age of 28 days at >95 %RH and 20 ± 0.3 °C. Subsequently, cylindrical samples for oxygen diffusion were prepared from the cubes by wet drilling, cutting and grinding. Diameter of all cylindrical samples was 100 mm, thickness of HPC_16mm samples was 50 mm, and thickness of all the other samples of mortar mixes from Table 2.2 was 20 mm, to ensure at least 3 times aggregate size. Drilling was performed perpendicular to the direction of casting and the surfaces (approximately the outermost 10 mm

in contact with the molds) were discarded. In most tests, two specimens per conditioning were tested. The exception is HPC_16mm, for which only one specimen of 50 mm thickness for each thermal load condition was tested.

After wet cutting and grinding, all samples were stored at 36 ± 3 % RH and 20 ± 0.3 °C for 1 week. For samples without thermal loading, oven drying at 50 °C for 7 days followed. On the other samples, thermal loading was performed at maximum temperatures of 120 °C, 200 °C, 400 °C and 600 °C for 8 hours with free cooling down in the furnace. The heating rate to reach the maximal temperature was 16 °C/min. To obtain a uniform distribution of temperature on all surfaces, all specimens were standing free in the furnace, with sufficient space between them for air to circulate (see Figure 3.4). After thermal loading/drying and before the O_2 diffusion measurements, all specimens were kept for 1 day in a desiccator at 20 °C over silica gel.

Figure 3.4 Positioning of samples in the furnace for Oxygen diffusion

As thermal loading of samples could cause explosive spalling, samples treated at 400 °C and 600 °C temperatures were placed in a massive metal container to prevent possible damage to the oven [118] caused by explosive spalling. Result of explosive spalling of one of the HPC+SAP samples thermally treated at 600 °C is seen in Figure 3.5. As result, only one sample of HPC+SAP at this load step was tested for oxygen diffusion.

Figure 3.5 Spalling of HPC+SAP sample as result of thermal treatment at 600°C

For HPC_16mm samples loaded at 600°C, cracks between large aggregates and mortar matrix were visually observed, but no spalling occurred. Effect of these cracks is presented and discussed in 3.3 and 3.4 parts of this thesis.

Dynamic vapor sorption

The desorption isotherm was measured with a Dynamic Vapor Sorption analyser (DVS) only on the HPC-ref mortar. The device allows continuous monitoring of the mass changes in samples exposed to either changing RH or changing temperature by means of a high-precision microbalance of accuracy 10 μg from which the sample holder is suspended. The material in the chamber is exposed to changing RH in a controlled flow of a mixture of dry nitrogen and water vapor. The RH is controlled with accuracy ± 1% by means of a dew point analyzer and the temperature with accuracy of ± 0.1 °C by means of Peltier elements. DVS of HPC was tested in two environmental regimes, at 20 °C and 40 °C, starting at 50 %RH and climbing to 100 %RH and back to 50 %RH. First cycle was performed at 40 °C and followed with the same RH regimes at 20 °C. Obtained results are presented below in Part 3.3.

Coefficient of thermal expansion

Thermal expansion of HPC-ref mix was measured with thermal expansion dilatometer. Both, the sample and reference material for correction of thermal expansion were placed in dilatometer. Change of length was recorded from 50 °C to maximal temperature of 980 °C with cooling down to 200 °C.

Expansion and shrinkage behavior was observed, and data is presented with correction for expansion of the system for main HPC-ref matrix in Part 3.3. This data gives basic overview of main HPC-ref matrix used in this study.

3.3.RESULTS

Mechanical properties

Figure 3.6 and Figure 3.7 present data of elastic properties of studied mortars after certain treatment. One can see the missing data for HPC-ref and HPC_SAP samples treated at 600 °C, Figure 3.7. This is due to the actual spalling of the samples, making measurements of static Young's modulus following EN 12390-13 impossible. Where available, the error bars represent a standard deviation.

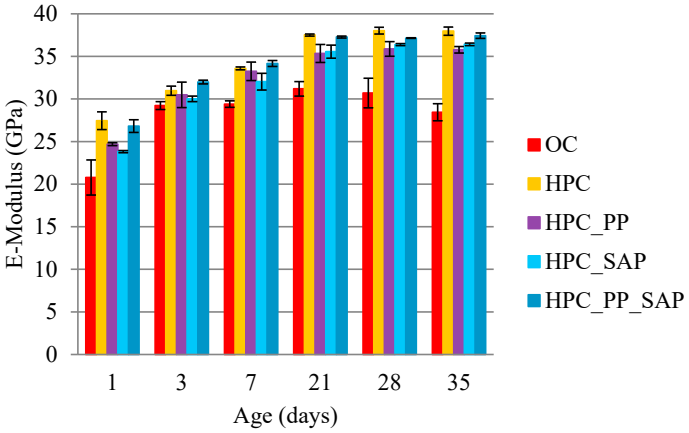

Figure 3.6 Evolution of E-Modulus over time (samples stored at 20 °C with no thermal loading)

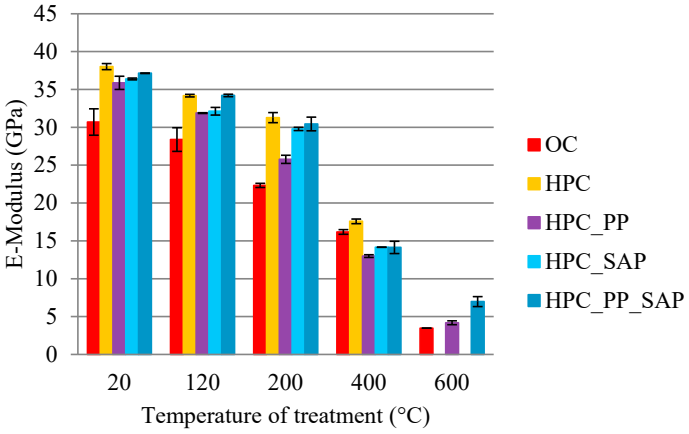

Figure 3.7 Evolution of E-Modulus of samples at age of 28 days due to thermal loads

The following two figures (Figure 3.8 and Figure 3.9) presents result of compressive strength that was measured as well on very same samples as static Young's modulus. Here, on

Figure 3.9, the data for HPC samples treated at 600 °C is available, while it was missing for Young's modulus in the figure above. This is due to the fact, that despite the actual spalling, the size of the sample needed to perform compressive strength measurement is smaller than for static Youngs modulus. And despite spalling, number of pieces were larger than $40 \times 40 \times 40$ mm^3, having the full cross section to perform the test.

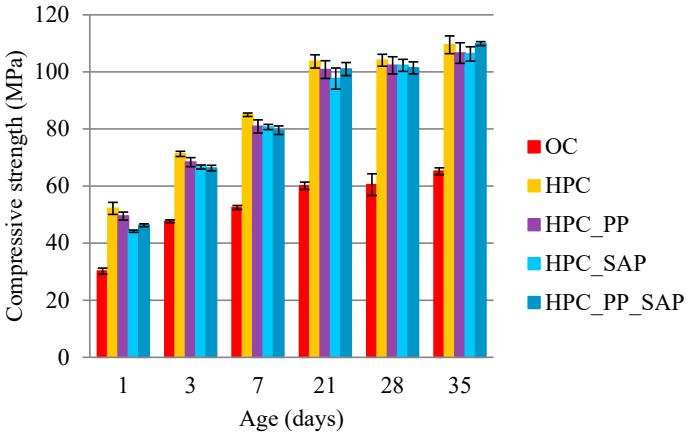

Figure 3.8 Evolution of compressive strength over time

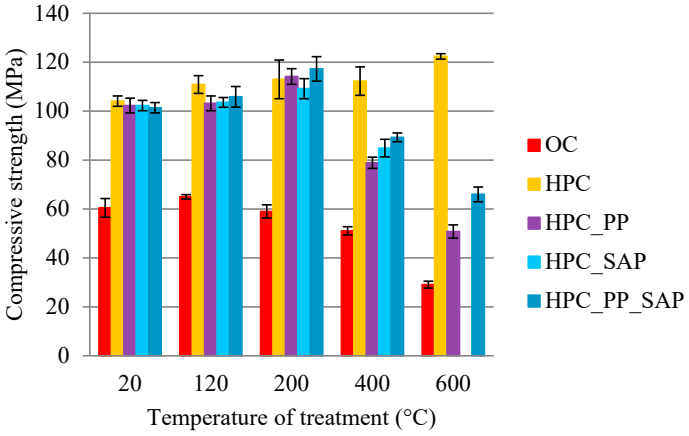

Figure 3.9 Evolution of compressive strength of samples at age of 28 days due to thermal loads

Results of flexural strength are presented below in Figure 3.10 and Figure 3.11, for non-treated and thermally treated samples respectively. The reason for missing data in Figure 3.11 is discussed above.

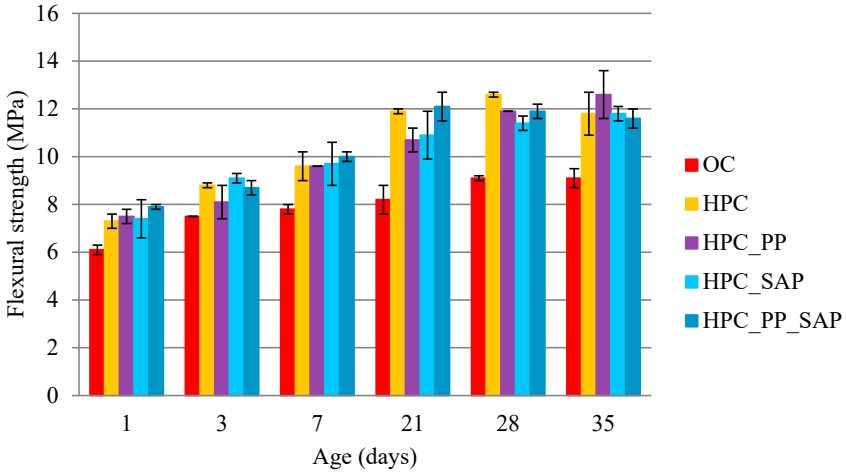

Figure 3.10 Evolution of flexural strength over time

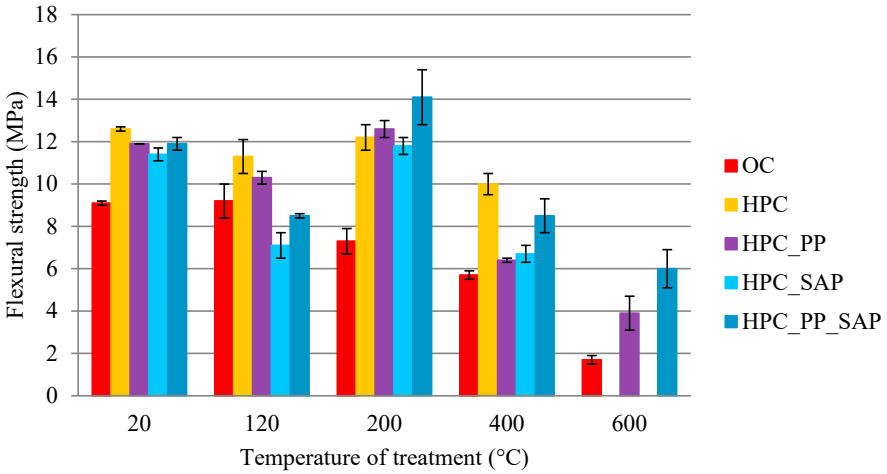

Figure 3.11 Evolution of flexural strength of samples at age of 28 days due to thermal loads

As it is seen from Figure 3.6, Figure 3.8 and Figure 3.10, mechanical properties of mortar samples are increasing for all the mixtures over time due to ongoing hydration, It can be noticed, that the evolution of mechanical properties in time for all HPC mixes is rather similar, indicating uniformity of HPC matrix in all HPC mortar mix variations. Similarly, decrease of Young's modulus of samples that were exposed to designed protocol of thermal loading that is seen on Figure 3.7 is related to loss of water.

One of the highlights are the missing data points in Figure 3.7, Figure 3.9 and Figure 3.11, as the corresponding samples spalled. However, from the three HPC samples that spalled, two chunks were large enough and with undamaged sides to perform compression tests. Despite the severe spalling, the leftovers showed the highest compressive strength throughout this measurement campaign. The small deviation in compressive strength of severe damaged HPC samples is likely to be related to only two samples available out of six normally used to measure compressive strength.

Thermogravimetric Analysis

In this part, results of TGA are presented in two ways: i) as general TGA curves for all 5 mixes where mass loss curves are a function of temperature and and ii) as mass loss after thermal loads. The focus is on mass loss, as it indicates amount of moisture available at each step of thermal load. As a rough assumption, the mass loss before 600 °C is related to dehydration and loss of physically bound water, while mass loss above 600 °C is mainly due to decarbonation of carbonate phases (mainly calcium carbonate).

The TGA results of all 5 mixes at the age of 28 days are presented in Figure 3.12.

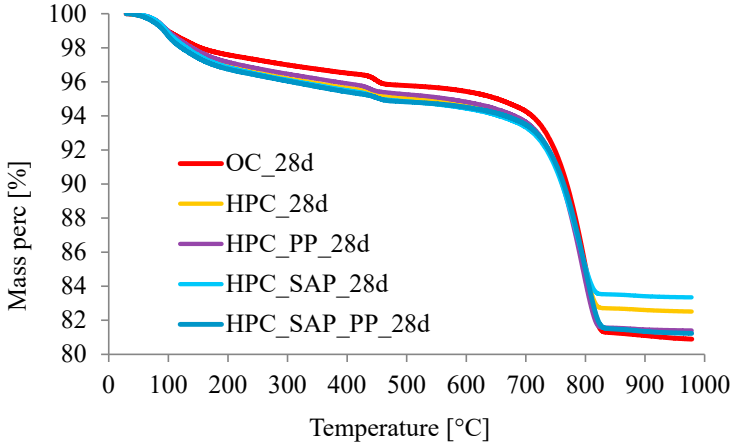

Figure 3.12. TGA results of all the mixes at 28 days of age (samples cured at 20 °C without thermal loads).

Here we assume, that no changes of carbonate phases takes place during thermal loading of chunks at 120 °C, 200 °C, 400 °C, 600 °C and crop scale bar of temperature axis down to 600 °C, while we are mostly interested in amount of H_2O available in the samples after thermal treatment and if rehydration of cement takes place. Once again, it is important to notice, that data is presented for samples at residual state after two cycles of solvent exchange.

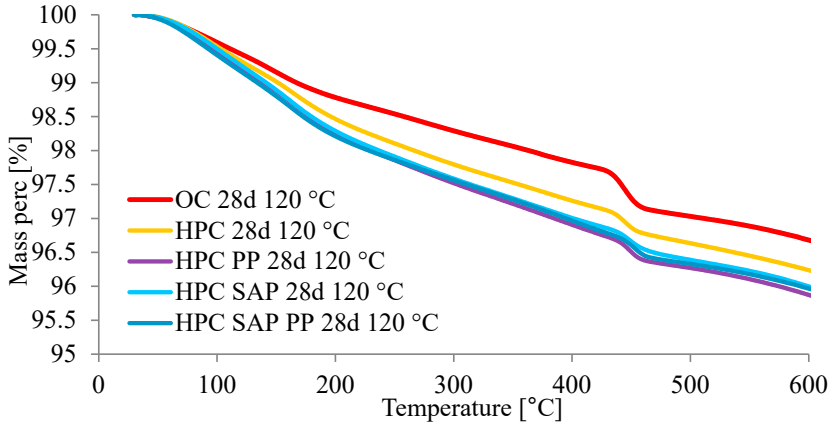

Figure 3.13. TGA results of all the mixes at 28 days of age after treatment at 120 °C, the residual state.

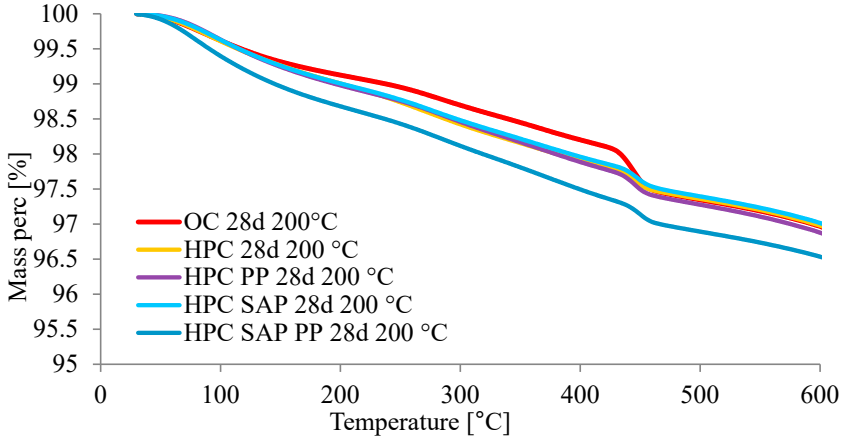

Figure 3.14. TGA results of all the mixes at 28 days of age after treatment at 200 °C, the residual state.

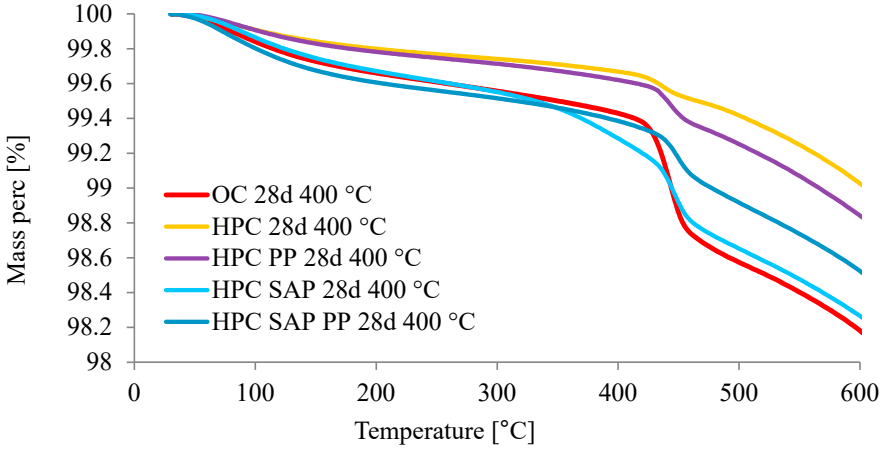

Figure 3.15. TGA results of all the mixes at 28 days of age after treatment at 400 °C, the residual state.

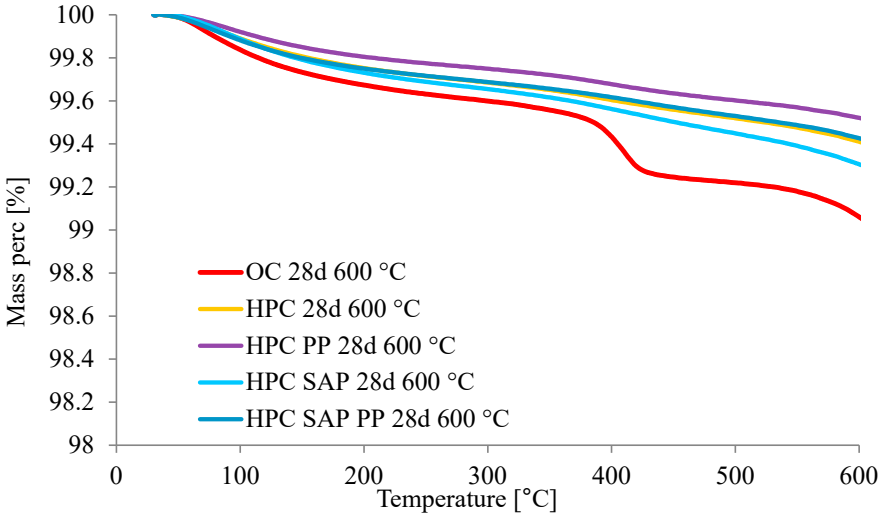

Figure 3.16. TGA results of all the mixes at 28 days of age after treatment at 600 °C, the residual state.

Mercury Intrusion Porosimetry

General type of data obtained with MIP is shown below on example of OC sample at 28 days of hydration, see Figure 3.17. Physical difference between 1st cycle and the 2nd cycle is discussed in details by Kaufmann[110]. Straightforward numerical value of the method provides the total porosity of the sample in percentage or mm^3/g; while shape of the curve does not give us the pore size distribution[109,110,119,120], it still provides a valuable information on breakthrough radius.

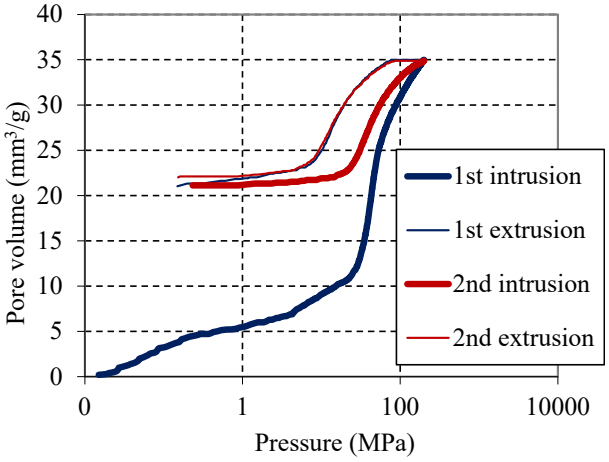

Figure 3.17. Results of two cycle MIP for OC sample at 28 days without thermal treatment.

The raw data of pressure applied with corresponding volume of mercury intruded into pores is processed with Washburn equation[111] and one can plot results as seen on Figure 3.18.

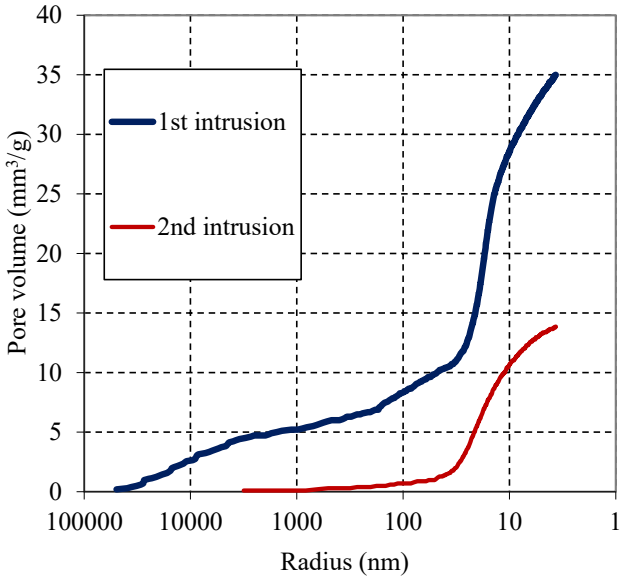

Figure 3.18. Cumulative pore volume of OC at 28 days, available through a certain pore radius.

Derivative of the data presented in Figure 3.18 visualizes the breakthrough radius through which large portion of pore volume is available, thus this radius is a threshold for transport properties and example of derivative curve for OC sample at 28 days if presented in Figure 3.19.

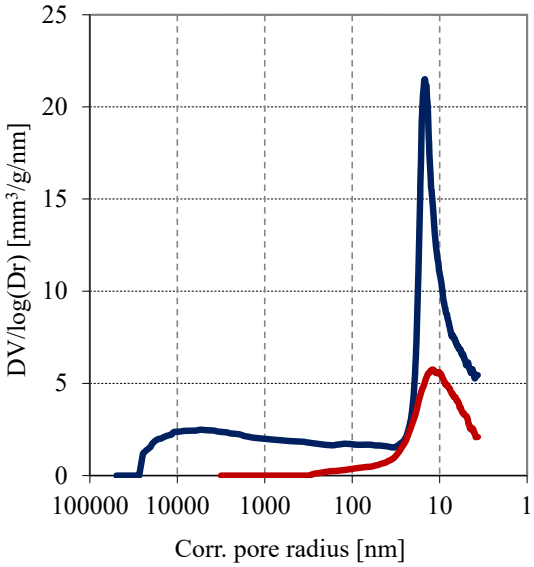

Figure 3.19. Derivative curve of porosity, OC 28 days of age.

Results presented below summarizes the peak values of the processed data similar to the plots of Figure 3.18 and Figure 3.19 for all the samples, while general intrusion curve of the 1st cycle and evolution of porosity for each set of samples are presented in Appendix 1 (evolution of porosity due to hydration) and Appendix 2 (evolution of porosity due to high temperatures). Evolution of total porosity and breakthrough radius over time, from time of mixing to stop of hydration at 3, 7 and 28 days of age (Figure 3.20 and Figure 3.21 correspondingly). Figure 3.22 and Figure 3.23 present changes of total porosity and breakthrough radius for samples exposed to thermal loads of up to 600 °C at the age of 28 days.

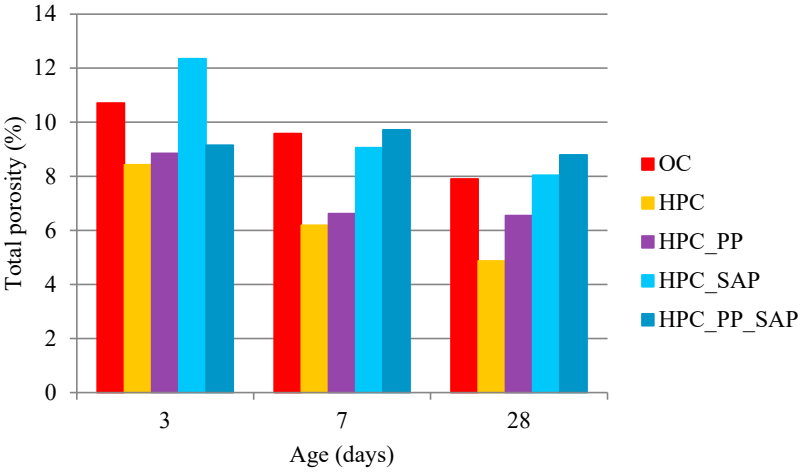

Figure 3.20. Evolution of porosity due to hydration.

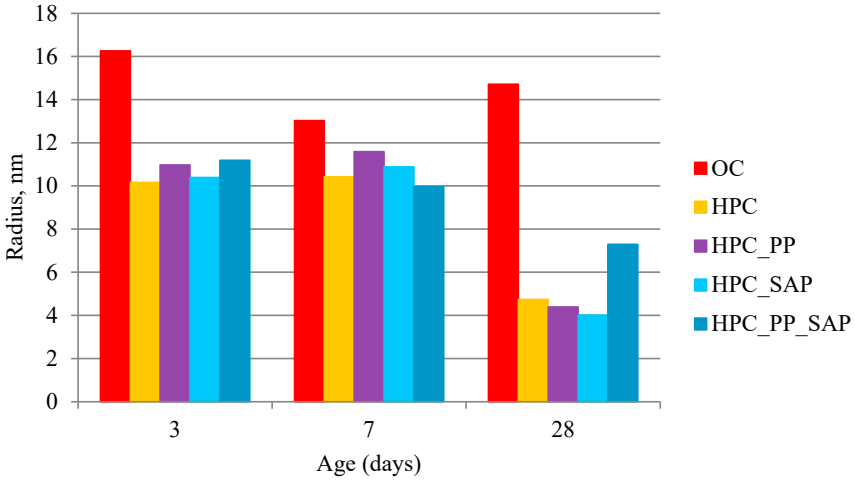

Figure 3.21. Evolution of breakthrough radius due to hydration.

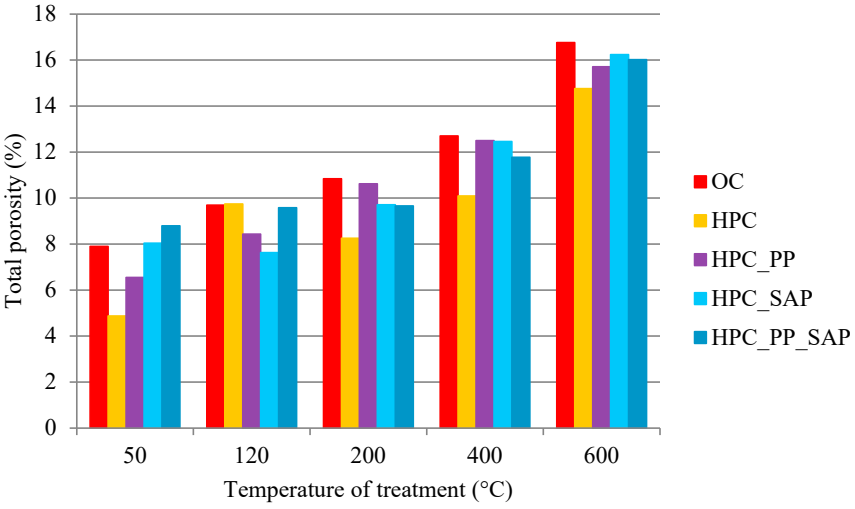

Figure 3.22. Evolution of porosity at 28 days of age due to thermal loads.

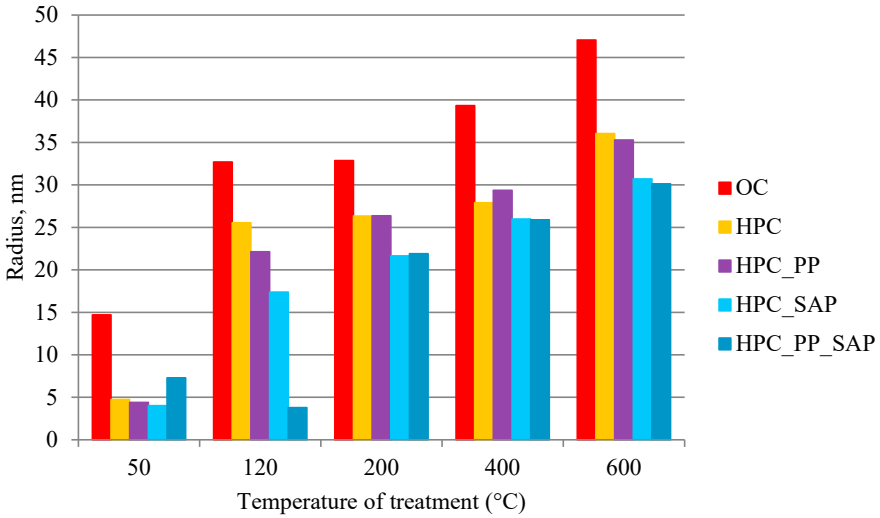

Figure 3.23. Evolution of breakthrough radius at 28 days of age due to thermal loads.

Oxygen diffusion

Results of oxygen diffusion are presented in Table 3.1 as relative residual oxygen diffusion. Results of oxygen diffusion for samples with PP fibers and large aggregates, treated at 600 °C, did not allowed to keep constant pressure from both sides of the sample, thou resulting in enormously low measured values. This can be both associated to severe cracking, as it was observed for samples with the large aggregates, or, high interconnectivity of the cracks and fibers, that might be the reason in the case of samples with PP treated at 600 °C.

Table 3.1.

Relative residual oxygen diffusion.

Mix type	Temperature, °C				
	50	120	200	400	600
OC	1.00	1.38	1.51	1.86	1.28
HPC	1.00	3.17	20.76	122.21	56.60
HPC+PP	1.00	1.63	4.51	0.73	*0.11*
HPC+SAP	1.00	2.42	14.23	44.49	11.53
HPC+PP+SAP	1.00	3.50	7.70	0.74	0.55
HPC-16mm	1.00	3.32	8.86	7.58	*0.10*

Dynamic vapor sorption

Results of dynamic vapor sorption for the reference HPC mortar matrix are presented below in Figure 3.24.

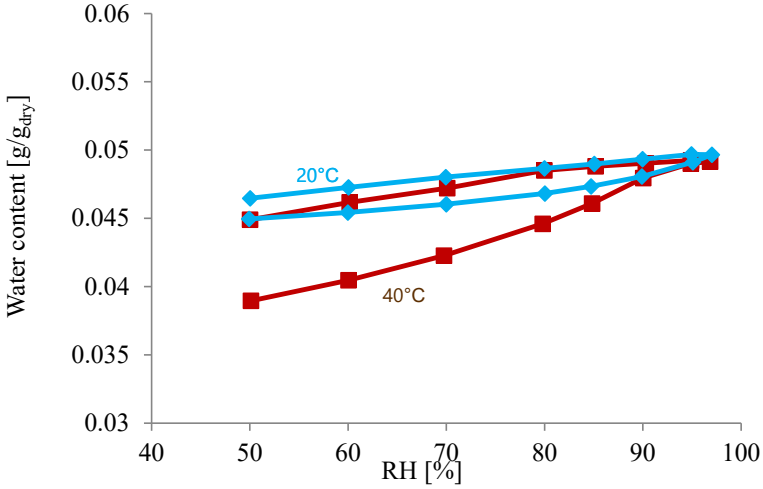

Figure 3.24. DVS results of HPC matrix.

Thermal expansion

The curve of thermal expansion of HPC main matrix is presented in Figure 3.25.

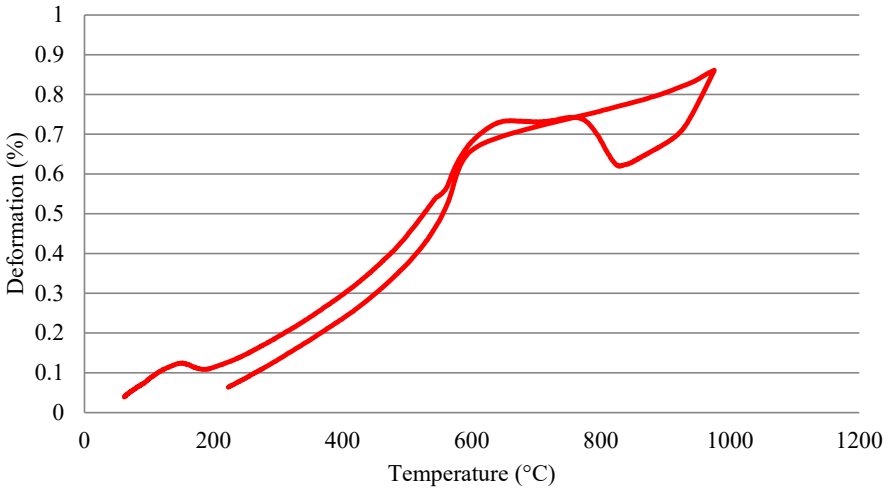

Figure 3.25. Thermal expansion of HPC mortar.

3.4. DISCUSSION

Complex and unified data on residual state of material after exposure to elevated temperatures is presented in this part. Evolution of mechanical properties over time is observed for all the mixes. While for all HPC type samples increase of Young's modulus, compressive and flexural strength is observed, the average value of Young's modulus for OC samples seems to decrease; however the error bars (standard deviation) are overlapping for samples at 28 and 35 days (see Figure 3.6).

Decrease of static Young's modulus for thermally treated samples is very clear and follows the data summarized from the literature. This has to do not only with the actual thermal damage at high temperatures, but also with drying and empty pores even at the temperatures of 120 °C and 200 °C At the same time, in line with literature (see Figure 1.3) an increase of average value of compressive strength is reported in Figure 3.9. The actual increase of residual static Young's modulus in this range of temperatures is reported by Zheng et al.[43] for Reactive Powder Concrete samples with steel fibers.

The residual mechanical properties measured in this study (see Figure 3.7, Figure 3.9 and Figure 3.11) are in a good agreement with the literature overview (see Figure 1.9, Figure 1.3 and Figure 1.6 correspondingly).

The HPC samples for mechanical properties that spalled during thermal loading to 600 °C might have experienced a higher general damage; however, local damage of small pieces that were still eligible to perform compressive strength measurements on the same shape and at the same conditions showed twice as high compressive strength then those HPC+PP and HPC+PP+SAP samples that did not spalled at 600 °C.

The evolution of pore system is described by Figure 3.20 and Figure 3.21, the data is mainly dominated by presence of SAP and PP fibers, especially for samples with SAP at 3 days of age.

While relative residual total porosity of mixes studied in this Thesis in general is in a good agreement with literature data, see Figure 3.26. where the total porosity from Figure 3.22 is presented as relative residual total porosity and plotted over literature data from Figure 1.12.

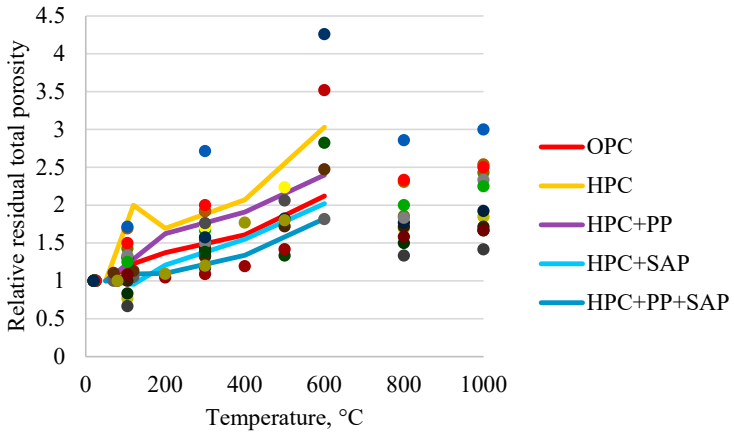

Figure 3.26. Comparison of relative residual total porosity with data from literature.

The breakthrough radius of HPC type mixes increases up to 6 - 7 times at 600 °C comparing to thermally non-treated samples, while same changes for OC samples are around × 3 the initial value (see Figure 3.23). This indicates higher thermal damage done to High Performance concrete compared to Ordinary Concrete.

As breakthrough radius represents necks/entrances of the ink-bottle pores and can be considered a proxy of gas and liquid transport properties, the MIP data is supported by the actual measurements of transport properties via Oxygen diffusion method (see Table 3.1). The increase in relative residual diffusion coefficient for HPC matrixes is higher at any step of

thermal loads. The data below 1 at 600 °C temperature is due to high thermal damage of HPC_16mm sample where the actual cracks were observed and pervious HPC+PP+SAP sample, where at this temperature level both SAP and PP are burned out and complex system of connected empty volumes is created, that helps vapor to escape[69]. On the other hand, in this particular case, the Oxygen diffusion equipment cannot equalize gas pressure on both sides of the sample, thus values of gas diffusion are underestimated for severe damaged samples. The actual thermal damage and severe cracking, especially around large aggregates, that is observed visually for HPC_16mm sample after treatment at 600 °C, from point of view of the diffusion measurements, looks similar to the combined effect of SAP and PP, which creates percolated network of channels. While eventually in both cases this should release the pore pressure and relaxation of thermal stress is expected to happen, the nature of these two events is different. The PP+SAP mix is designed to increase the permeability in the case of high temperatures, while the increased permeability of HPC_16mm samples is the result of thermal damage that can be unpredictable and result in spalling.

The DVS data indicates hydroscopic behavior of HPC matrix with low w/b ratio, where the absorbed moisture contributes to further hydration, as some cement is left unhydrated in HPC, as seen from TGA data of thermally non-treated specimens (see Figure 3.12). While the general hydroscopic behavior seen from TGA data, e.g. Figure 3.13, Figure 3.14, Figure 3.15 and Figure 3.16, indicates the rehydration of thermally treated samples. As in all cases, after cooling the samples down to residual state followed by solvent exchange procedure to prepare samples for TGA, the mass loss was observed in the temperature regions that the samples were already exposed to. Another explanation to the mass loss during TGA measurements in the temperature regions that the samples were already exposed to by thermal treatment in the oven is the scale effect. The moisture was trapped in the small chunks, and the time of treatment was not sufficient for moisture to escape. This was observed and measured on the HPC+SAP sample treated at 120 °C and used to determine mechanical properties. The cross-section of the sample after 3-point bending test was presented before, see Figure 3.2. The difference in the moisture content can be seen and the supporting TGA results are presented in Figure 3.3. While the double thickness of the drying front is comparable to the size of the chunks used to prepare TGA samples, the volume of the sample available for the moisture to escape is significantly smaller. This can lead to moisture being trapped inside the chunks, as temperature of environment and outer regions of the chunks is smaller during most part of the thermal loading procedure. Moisture that is free water is later removed by solvent exchange method. Thereby, the concept of water migration to the core of the sample as the only difference between inner and outer part of the sample is eliminated by sample preparation procedure for TGA. The high moisture content and pore pressure are expected to affect the dehydration of crystals. This is another explanation for the presence of bonded water in TGA samples even despite the small size of each chunk of material.

The heating rate is one of the parameters that affects dehydration. The dehydration degree of the samples with low heating rate is higher than of those that had a higher heating rate[121], as first group of samples would have more time to dehydrate, as the loading procedure is longer. As for this study, the rate of thermal loading for mortar samples was lower than in the actual TGA test and the samples spent more time at the maximal temperature. Thus, the residual chemically bonded water is associated with rehydration and/or scale effect.

The spalling effect of dense rocks is due to thermal stresses, as material expands, while thermal load of pure cement paste should lead to shrinkage due to dehydration. This complex behavior is seen on curve of thermal expansion of HPC sample (see Figure 3.25); where before the ultimate thermal expansion at temperatures above 200 °C, shrinkage is observed between 150 °C and 200 °C. The thermal expansion of the sample that starts around 600 °C is an expansive phase transition of quartz.

To conclude, the changes in microstructure of the studied mixes under the designed conditions are in good agreement with literature date. The experimental matrix represents a broad set of concrete properties under well-controlled, unified conditions. The standard deviation of obtained mechanical properties is low; thus, the measurements are repeatable.

The rare case of spalling of HPC samples for mechanical testing when after release of the stresses few pieces were large enough to perform an actual testing on not damaged $40 \times 40 \times 40$ mm^3 volume brings new insights. The pre-spalling state of material might have superior mechanical properties comparing to one where the stresses are released uniformly due to having higher porosity, polymer fibers or SAP.

4. NONDESTRUCTIVE EVALUATION OF CONCRETE EXPOSED TO HIGH TEMPERATURES

4.1. APPLICATION OF NEUTRON RADIOGRAPHY TO CONCRETE

To understand the complex mechanisms underlying explosive fire spalling, it is paramount to follow the moisture distribution in concrete during exposure to high temperature, quantitatively and non-destructively, in real time[122]. An effective method to measure water distribution in concrete is neutron radiography[123]. In concrete, aggregates and anhydrous cement weakly interact with neutrons, while hydration products and water-filled capillary pores have the largest interaction (mainly neutron scattering), leading to strong attenuation of an incident neutron beam. The application of neutron radiography to study water transport in cementitious materials subjected to high temperatures was already suggested in [124]; this idea, however, has been followed only recently[125,126]. Weber et al.[125] performed neutron radiography on small mortar slabs (dimensions 80 × 80 × 10 mm^3) standing on a heating element and heated up to 600 °C in 15 min. In order to obtain 1-D temperature and moisture fields, the specimens were insulated against moisture and heat loss using aluminum foil and glass foam, except from the bottom and top edges. Temperature profiles were measured via embedded thermocouples and quantitative moisture profiles were obtained by means of neutron radiography[125]. Research described in this part of the thesis is a development of Weber at al.[125] study, eventually resulting in number of papers[69,80,106,127–129].

As complex measurements of temperature and pressure fronts would result in number of wires, pressure tubes, sensors and heating element itself, alongside with probability of explosive spalling, first measurements were performed on setup with sample fixed in one position and enclosed in a metallic (aluminium) protective box to protect the imaging apparatus from a possible debris and exhaust the fumes from the sample and insulation. In this way, obtaining 2D datasets as sequence of neutron radiography images over time/heating process was possible. Next, gaining experience in designing safe 2D experiments, it was possible to move to 3D Neutron tomographies, where sample and heating element would rotate[80,127–129]. This research campaign resulted in both first ever visualized explosive spalling of concrete in 2D[69] and in 3D[129]. I took part and produced all the specimens for two independent neutron imaging sessions, NEUTRA beamline[69,106] at Paul Scherrer Institute (Villigen, Switzerland) and at NeXT D50 beamline[80,127–129] at Institute Laue-Langevin (Grenoble, France), the mix compositions used are identical, produced with the same equipment and mixing protocol. The datasets complement each other, and the microstructural study is presented in this Thesis.

Design of experiments

As concerns pore pressure, several authors have directly performed measurements in concrete specimens subjected to thermal transients (see for instance[4,8,105,130]). This was generally performed by embedding thin stainless-steel pipes provided with external electronic pressure sensors. Possible alternatives[131] come from the adoption of a porous sensing head (to measure the mean pressure of larger paste volumes) and filling the pipe with thermally stable silicon oil (to prevent moisture leakage and minimize the compressible gas volume). Pressure sensors were cast at different distances from the heated surface of concrete and the pressure

was measured together with the temperature[130,131]. Consistent results were generally obtained in different test conditions (concrete grade, moisture content, heating rate) and values as high as 4–5 MPa were reported in the case of HPC[131], while lower values were reported for normal-strength concrete[8]. For a better understanding of spalling mechanisms, the results of pore pressure measurements should be directly compared with the moisture profiles inside the sample during thermal loading, which might reveal the formation of moisture clogs. First attempts in this direction have been recently made by combining proton-spin relaxation NMR and pressure sensors[132]. Juarez Trujillo et al.[133] compared experimentally measured pore pressure with results of simulations, the experimental results were considerably lower than the simulated. This shapes the complexity of the actual pore pressure measurements during thermal heating.

In this study, neutron radiography was applied to investigate the water distribution in mortar samples heated from one side up to 550 °C. The samples were mortar slabs with dimensions of $25 \times 100 \times 100$ mm^3 standing on a heating plate, with the 100×100 mm^2 face exposed to the neutron beam (Figure 4.1b). In addition, the temperature distribution within the samples was obtained by means of a series of thermocouples and the vapor pressure at two different locations was measured via pressure sensors, same as used by Felicetti and Lo Monte[134]. In total, 16 tests were performed on mortar samples at different ages and with different compositions. Results presented here regard two types of high performance mortar. The first sample was a mortar with SAP, which is expected to be prone to explosive spalling due to high moisture content (see[66,102]), while the second sample was a mortar with a combination of SAP and PP-fibers, where the risk of spalling should be reduced[95].

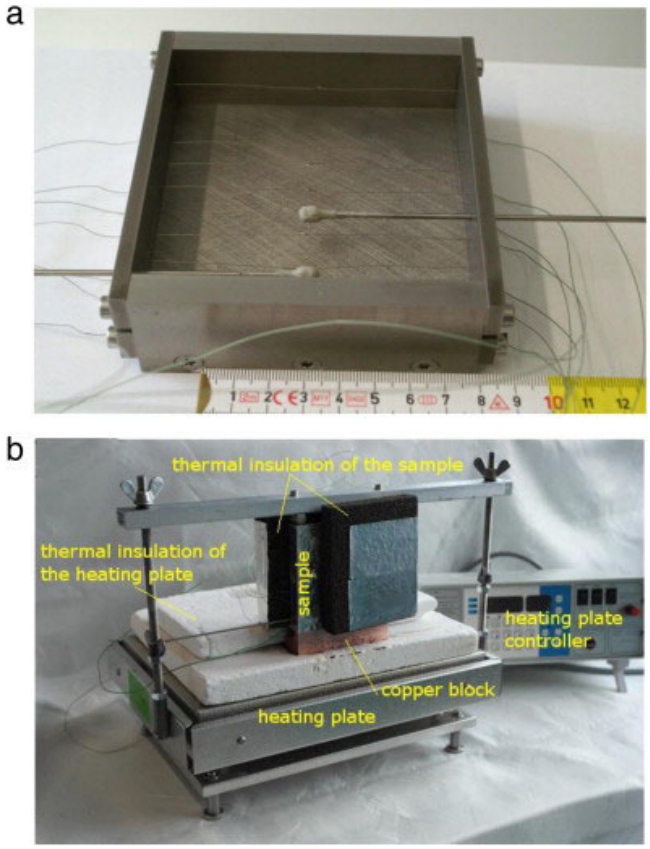

Figure 4.1 a) Mold fitted with thermocouples and two pressure sensors; b) arrangement of the sample during the test. The sample is moisture-sealed using high-temperature resistant adhesive aluminum foil and thermally insulated by means of black glass foam (partially stripped for the demonstration). The sample is placed on a copper block that allows the heat to conduct from the heating plate (the remaining surface of the plate is covered by white ceramic insulation plates). Note that during neutron radiography manometers were fixed at the ends of the capillary tubes and the sample was placed inside a thin aluminum box to protect the neutron detector from spalling debris[69].

The cross-section of the samples was chosen to fit into the field of view of the neutron beam, which was 150 × 150 mm^2. Thin samples are preferred because they do not induce too large neutron attenuation, thus avoiding the need of long exposure time of the camera to achieve a satisfactory signal-to-noise ratio, and limit artifacts due to sample scattering. At the same time, the samples needed to be thick enough compared to aggregate size, especially to accommodate the pressure sensor heads, which were embedded in the samples during casting. Moreover, thick samples should allow minimizing the boundary effects on the moisture profile along the plate thickness (direction perpendicular to the observed plane). Based on these constraints, mortar samples with dimensions of 100 × 100 × 25 mm^3 were cast.

High-performance mortars with w/b equal to 0.34 were mixed using a 5-l Hobart mixer (the mix composition is presented in Table 2.2). The binder was Portland cement CEM I 52.5R blended with undensified silica fume at a mass proportion of 4:1. Here, the results for two

mortars are presented: with addition of SAP (denoted as SAP) and with addition of SAP and PP-fibers (denoted as PP + SAP).

Dry solution-polymerized SAP of sizes 63–125 μm were added to the mixture in the amount of 0.33% by weight of binder. The SAP is saturated with pore fluid and form water reservoirs in the fresh mortar. After internal curing has taken place in the initial days of hydration[135,136], voids of 100–200 μm size, partially filled with hydration products (mainly calcium hydroxide), remain in the mortar[97].

In the PP + SAP mortar, PP fibers of 3 mm length and 30 μm diameter were added in the amount of 0.34% by mass of binder (corresponding to 2 kg per m^3 of mortar). Polycarboxylate ether-based superplasticizer was used to improve the workability of the mixtures. The mortars contained 60% by volume of alluvial sand (sandstone, limestone, dolomites and metamorphic rocks) with grains up to 4 mm. Same mortar mixes as described earlier in Table 2.2.

Firstly, thermocouples and capillary tubes were fitted to the molds (Figure 4.1a) and then the mortar was carefully cast into the mold, placed on a vibration table. The samples were next covered with plastic sheets and placed at 20 ± 0.3 °C and > 95% RH. After demolding at 1 day, the samples were sealed in plastic bags and stored at 20 ± 0.3 °C and 95 ± 3% RH until the age of about 3 weeks (18 days and 22 days for PP + SAP and SAP sample, respectively), when the tests were carried out. Seven thermocouples (type K, Ø = 0.2 mm, all welded) were embedded directly into the samples during casting (Figure 4.1a). The nominal position of the thermocouples was 5, 15, 25, 45, 55, 65, and 95 mm from the heated side. The actual position of the thermocouples was determined by performing X-ray radiography on the samples immediately before the test (Figure 4.3a).

The pore pressure measurements were performed by means of capillary steel pipes (Ø = 2 mm) with heads made of sintered metal fitted on their ends (Ø = 5 mm) (Figure 4.1a). Before casting, the heads were dipped in dense cement paste in order to avoid penetration of fluid cement paste during casting. The nominal position of the sensors was 10 and 35 mm from the heated side. Immediately before the tests, the pipes were filled with silicone oil and one additional thermocouple was inserted into each pipe.

The arrangement of the sample on the heating block is presented in Figure 4.1b. Before heating, the samples were insulated against moisture and heat loss. Aluminum foil (almost transparent to neutrons) provided with high-temperature silicone adhesive was applied on all faces except the bottom (heated) face to avoid vapor loss. In general, insulation with aluminum foil from moisture loss is a common solution for concrete. Often it is used to seal concrete samples for autogenous shrinkage measurements. Recently, we used it to prevent loss of moisture from the sides of the samples during another beam-time at PSI, at ICON beamline, investigating effect of cracks on drying of concrete[137]. The aluminum foil prevents the sample from drying out, but it does not provide a tight sealing that would allow for a large pressure build-up. The sides of the sample were then thermally insulated using a 20 mm-thick glass foam layer which was finally wrapped with aluminum tape to hold it in position. The manometers were then mounted onto the ends of the capillary tubes, and the sample was placed on the heating device (a programmable heating plate). During neutron radiography, the sample had to be positioned close to the scintillator, while the heating plate needed to be kept away from the field of view. Furthermore, the goal was to heat only the bottom of the sample and to limit the heating of the sides by convection. In order to meet these constraints, a copper element was interposed as heat conductor between the sample and the heating plate. This element had its

bottom face laid directly on the heating plate, and the dimensions of the top face fitted just to accommodate the sample. This arrangement allowed placing the ceramic insulation plates all around the copper conductor and minimizing the heating of the sample sides and of the surrounding neutron imaging facilities. The temperature of the copper block below the sample was measured by means of a thermocouple. The sample was then fixed on the heating plate/copper block with an aluminum frame pressing on its top edge (see also Figure 4.3b). Finally, in order to protect the surroundings (especially the detector) from spalling debris, the sample was contained within an aluminum box with a 1 mm-thick wall. The heating plate was programmed to reach 550 °C in 12 min and hold the temperature for the following 2 h.

Neutron radiography was performed at the NEUtron Transmission RAdiography (NEUTRA) beamline of the Paul Scherrer Institute (PSI) in Villigen, Switzerland. This beamline is fed by the Swiss Neutron Spallation Source (SINQ) and is operated with neutrons within a thermal spectrum characterized by a Maxwell-like probability density function, with a most probable energy level of about 25 meV[123]. The detector setup used consists of a 100 μm thick 6Li doped ZnS screen imaged by a fast readout sCMOS system (Andor Neo). The sample face was fixed at a distance of 55 ± 1 mm from the scintillator. The field of view had a size of 124 × 147 mm2 with a nominal pixel size of 57.5 × 57.5 μm2. The exposure time for a single image was 14 s and the total image acquisition time was about 18 s, providing an image frame rate of about 3.5 frames per minute.

The intensities measured in the neutron radiography are related to absorption and scattering of neutrons by the sample. The attenuation of the intensity I follows the exponential law of radiation attenuation (Beer–Lambert law):

Equation 4.1

$$I(x,y) = I_0(x,y)e^{-\int \Sigma(x,y,z)dz}$$

where I_0 is the intensity of the incident neutron beam and Σ is the effective attenuation cross-section, which depends on the sample material.

We assume that the material basically consists of water in free or chemically bound form and of dry components (anhydrous cement, aggregates), each characterized by an equivalent thickness. We further assume that the change of attenuation due to vaporization of hydrogen from SAP and PP-fibers should be negligible, based on the very low concentration of the polymers in the mortars compared to their water content. The attenuation can then be written as

Equation 4.2

$$I(x,y) = I_0(x,y)e^{-\Sigma_w d_w(x,y)-\Sigma_c d_c(x,y)}$$

where Σ_w and Σ_c are the effective attenuation cross-sections of water and of dry components (binder, aggregates, polymers, etc.), respectively, and d_w and d_c are the corresponding equivalent thicknesses.

The neutron beam transmission coefficient T is then

Equation 4.3

$$T(x,y) = \frac{I(x,y)}{I_0(x,y)} = e^{-\Sigma_w d_w(x,y)-\Sigma_c d_c(x,y)}$$

Assuming that only the water content changes during the experiment, the variation of the equivalent water thickness $\Delta d_w = d_w(x, y, t) - d_w(x, y, t_0)$ is determined as:

Equation 4.4

$$\Delta d_w(x,y,z) = \frac{1}{\sum_w} \ln \frac{T(x,y,t)}{T(x,y,t_0)}$$

Before calculating the equivalent water thickness, the recorded images have to be corrected for camera electronic noise (dark current correction), backscattering of neutrons (black body correction), and spatial and temporal inhomogeneities of the neutron beam or of the scintillator screen (flat field correction), see[138].

Other effects such as sample scattering and beam hardening have been accounted for by calibrating the whole measuring setup with the effective attenuation cross-sections of water. To this end, an aluminum container with twelve water steps (thickness from 1 to 12 mm) placed in the neutron beam direction has been analyzed (see also[137,138]). By using Equation 4.4 with the empty container as the initial state and the filled container as the final state, the curve labeled "uncorrected" in Figure 4.2a was obtained, assuming a constant cross-section for water equal to $\Sigma_w = 0.35\ \text{mm}^{-1}$. For the correction, the cross-section has been calculated using Equation 4.4 and taking for Δd_w the geometric water thickness. As shown in Figure 4.2b, the cross-section changes linearly with the water thickness. By using this variable cross-section, the corrected curve for the water steps can be constructed as shown in Figure 4.2b. Note that the original, i.e. assuming no water loss from the sample, water thickness calculated from mix design, where roughly 20% of sample volume is occupied by water (see Table 2.2), is 5 mm in the mortar samples considered here (to remind, thickness of the sample – 25 mm). Alternatively, a simulation of the sample scattering has been proposed for the scattering correction[138]. However, based on the simple 2-D geometry of this experiments, and considering also the complex simulation procedure[138], a simple scheme based on measurements on water steps was considered sufficient for correcting the sample scattering and beam hardening artifacts.

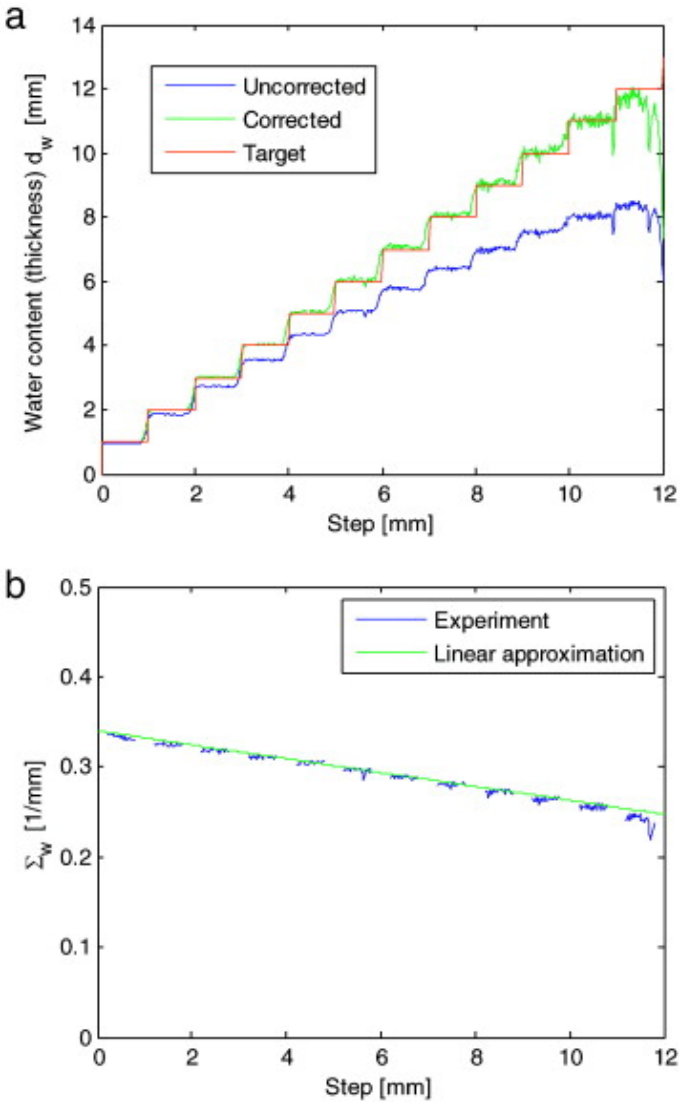

Figure 4.2 Variable macroscopic cross-section accounting for sample scattering and beam hardening: a) corrected and uncorrected water contents in the water steps; b) calculated cross-section of water. The equivalent thickness of water in the mortar samples at the start of testing is equal to 5 mm[69].

Before heating tests and neutron imaging took place, X-ray radiographies of all samples were acquired in order to determine precisely the positions of thermocouples and pressure sensors. This was possible thanks to the additional X-ray tube and detector available at the NEUTRA imaging facility. A voltage of 100 kV was applied to accelerate the electrons and the current of the electron beam was 15 mA.

Results and discussion

Figure 4.3a shows an X-ray radiograph of the sample that was acquired in order to determine the exact position of the thermocouples and of the pressure sensor heads. Figure 4.3b shows an exemplary neutron radiography image in which the drying front in the PP + SAP sample after 24 min of heating is evident. Some boundary effects are visible near the vertical edges of the sample, due to imperfect insulation that led to faster drying. This effect can be attributed to both thermal insulation and moisture insulation. In order to exclude these boundary effects in the evaluation of the moisture profiles (see Figure 4.6), only the region indicated by the rectangular frame in Figure 4.3b was considered for averaging the moisture content changes.

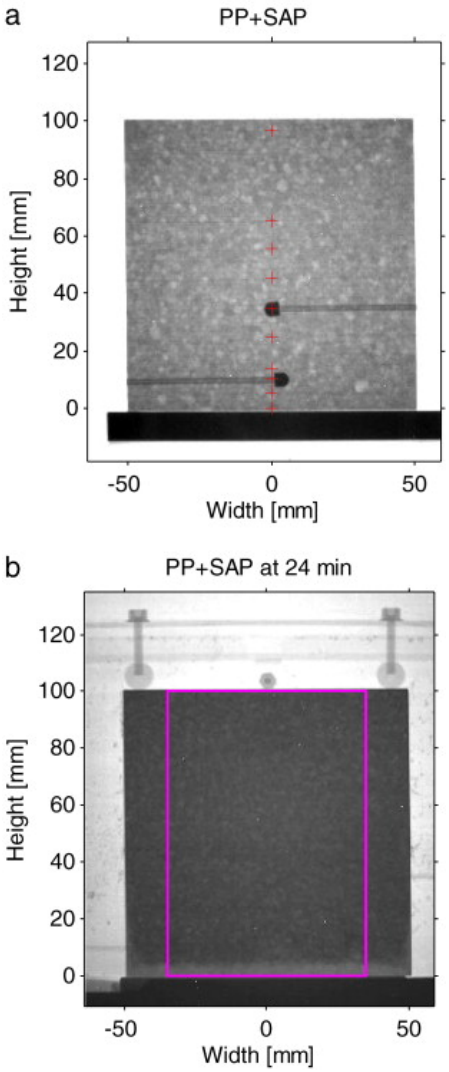

Figure 4.3 a) X-ray raw radiography image showing the position of the thin thermocouples (indicated with crosses) and of the pressure sensor heads, b) neutron raw radiography image after 24 min of heating. The drying front is clearly visible. The rectangular contour in Figure 4.3b indicates the averaging region for obtaining the moisture profile (Figure 4.6). The gray levels refer to beam intensity[69].

As could be expected based on the findings presented in[95], the addition of both SAP and PP-fibers allowed avoiding spalling. On the other hand, spalling occurred after 24 min of heating in the sample with SAP only (Figure 4.4). Spalling took the form of a large crack parallel to the heated surface along the whole length of the slab at a height of about 6 mm (corresponding to the position of the drying front, see Figure 4.4, Figure 4.6b).

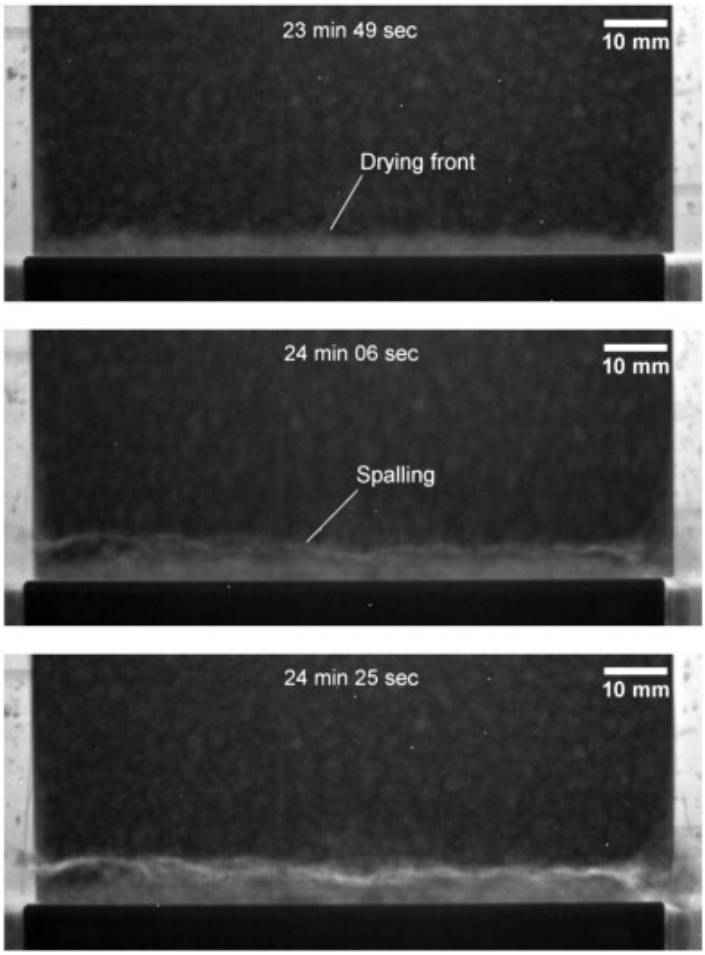

Figure 4.4 Sequence of raw neutron radiographs (cropped bottom part of the sample) showing drying and spalling in the SAP mortar. Time 23:49: just before spalling, the dried region is visible in brighter gray values. Time 24:06: the spalling crack appears first as a fine line and widens in the successive radiographs. The gray levels refer to beam intensity[69].

The temperature profile was determined by fitting spline curves (Figure 4.5) to the readings of the embedded thermocouples, whose locations were determined via X-ray radiography (Figure 4.3a). Note that the temperature at the height of 0 mm was assumed equal to the temperature of the copper block on which the sample was placed. Only the lower 35 mm near the heated surface is shown. There is no marked difference between the temperature profiles in the two samples, albeit the spatial resolution of the thermocouples is not fine enough for a precise assessment.

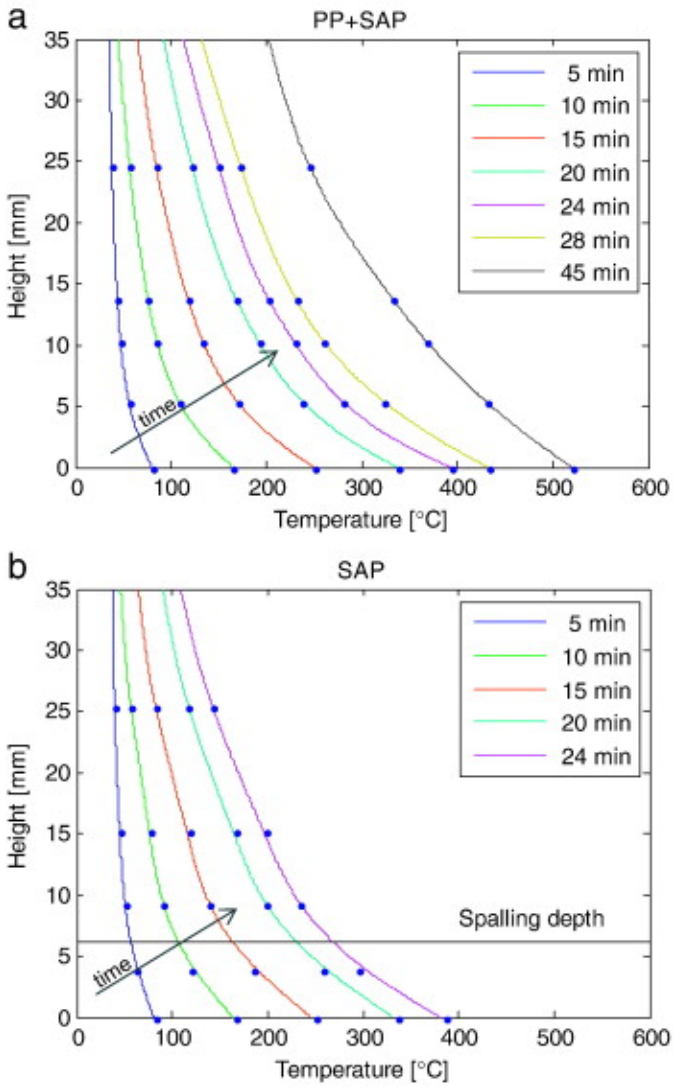

Figure 4.5 Temperature profiles of lower 35 mm of the mortar slab: a) PP + SAP sample (no spalling), and b) SAP sample (spalling occurred after 24 min at 6 mm height)[69].

The water loss profiles (expressed as equivalent water thickness[139,140]) are shown in Figure 4.6. The mixing water occupied approximately 20 % of the mortar volume (see Table 2.2), which for a sample thickness of 25 mm corresponds to an initial equivalent water thickness of 5 mm. The water being the difference between the moisture content at time t and at t_0 (start of heating) was calculated with Equation 4.4. The profiles were obtained by averaging at each height the change in moisture content along the horizontal line enclosed by the region indicated in Figure 4.3b. The profiles feature a plateau corresponding to a sudden change in slope where the water loss changes rapidly from almost zero to a large negative value over a small height. The approximate position (height) of the plateau therefore indicates the drying front, where a

large portion of free and chemically bound water disappears by vaporization and dehydration, respectively. Since the drying takes place in a certain narrow region, the plateau is not perfectly horizontal but extends over a certain height.

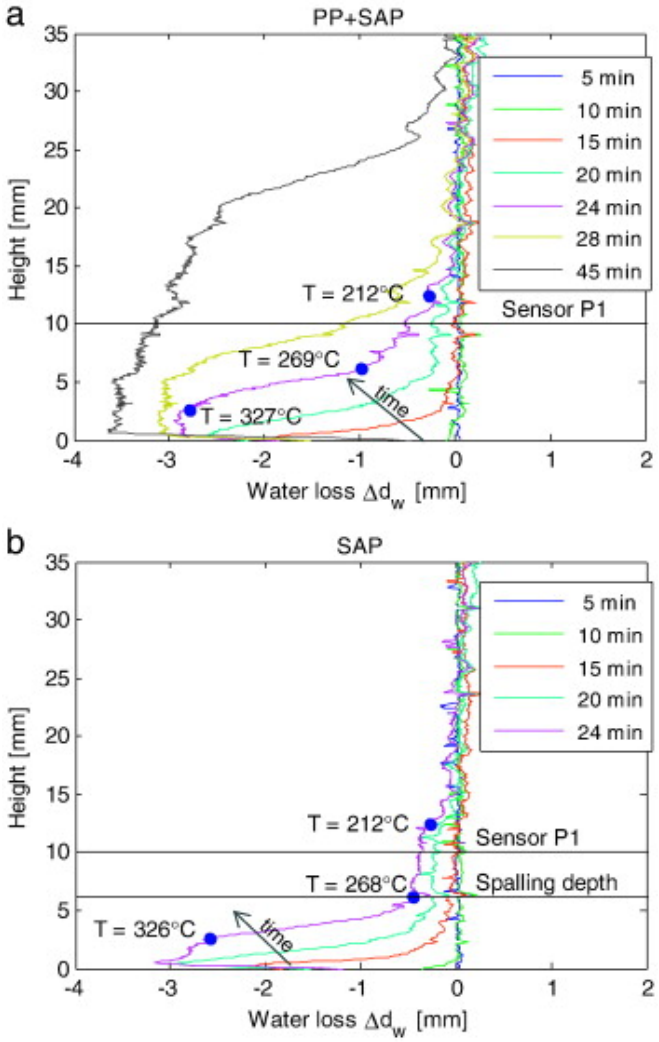

Figure 4.6 Water loss profiles (expressed as equivalent thickness) of the lower 35 mm of the mortar slab (note that the profiles were measured for the whole height of the sample): a) PP + SAP sample (no spalling); b) SAP sample (spalling occurred after 24 min at 6 mm height). Estimated temperatures at 24 min are indicated for characteristic points of the profile[69].

No moisture accumulation ahead of the drying front is evident in Figure 4.6, in contrast to the first pilot tests[125]. Moreira et al.[71] observed accumulation of moisture ahead of the drying fronts depending on the heating rate. Here the drying front moved faster in the sample with PP + SAP compared to the sample with SAP only and did not show any sharp change in slope. This is likely due to the increase of permeability occurring when PP-fibers melt and form channels through which the vapor can be evacuated[87,93]. On the other hand, a sharp change in the water loss is visible in the SAP sample in correspondence with the position of spalling,

Figure 4.6b. Knowing that dehydration consumes energy, the moisture profiles allow inferring that the temperature profiles are also smoother and thermal stresses should be reduced when PP-fibers are added. The moisture profiles can therefore complement the temperature measurements that were not obtained with sufficient spatial resolution in this experiment.

The pore pressure measured by the pressure sensors (placed at 10 and 35 mm from the heated face) is shown in Figure 4.7 as a function of time. The pressure peak is expected to be correlated to the drying front, where water loss proceeds at the highest rate. This is confirmed by the water loss profiles in the PP + SAP sample. It can be seen in Figure 4.6a, that the drying front (understood as the region where the moisture change profile shows a plateau) reaches the position of the first pressure sensor (located at 10 mm from the heated side) at about the same time when the maximum value of pressure is measured (compare the change of slope of the 28-min profile at approximately 10 mm height in Figure 4.6a with the occurrence of the pressure peak at that time at the 10 mm position in Figure 4.7a).

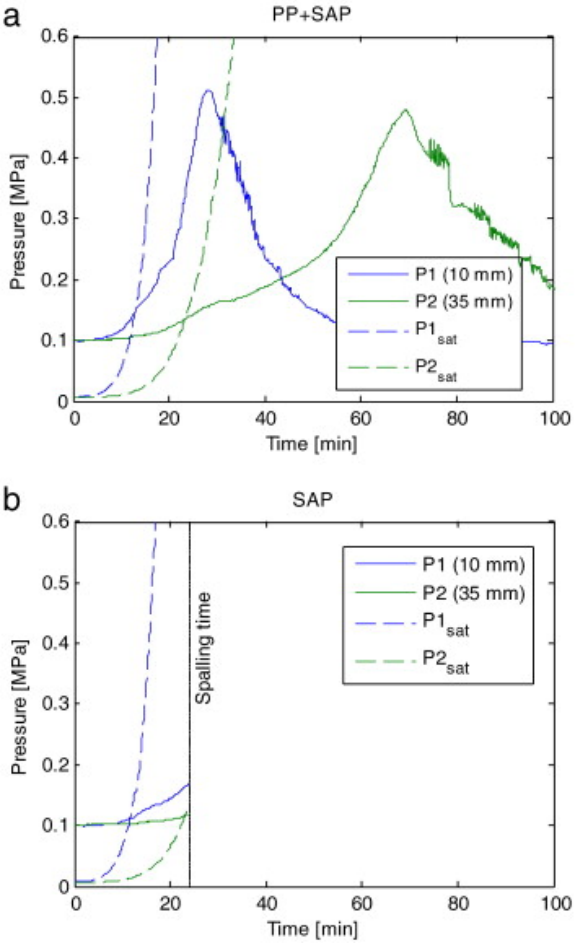

Figure 4.7 Pore pressure measured by the two sensors P1 and P2 (nominal distance from the heated side indicated): a) PP + SAP sample (no spalling); b) SAP sample (spalling occurred after 24 min at 6 mm height). Vapor saturation pressure curves (calculated on the basis of the temperature measured in correspondence of the sensors) are also reported[69].

The pressure in the sample with no PP-fibers (Figure 4.7a) is shown only up to the spalling event, since afterwards it is greatly influenced by the pressure release through the spalling crack. But even up to the spalling event, the pressure increases less than in the sample with PP-fibers (Figure 4.7a). This is consistent with the slower evolution of the drying front in the sample with no PP-fibers (Figure 4.6b), which suggests a slower advancement of the pressure peak and thus a larger distance from the pressure sensor at a given time (similar results were found by Kalifa et al.[105]). Before the pressure peak could reach the first sensor, spalling took place at a lower position in the SAP sample. Once spalling occurred, the pressure could suddenly be released through the spalling crack and the heat transfer between the copper block and the sample became less effective.

Figure 4.7 shows also the vapor saturation pressure curve as a function of time, at the location of each pressure sensor. Unlike in [4,8], the pressure does not appear to follow the equilibrium vapor pressure.

4.1.1. Summary/Conclusions

Neutron radiography has been performed on mortar slabs exposed to heating up to 550 °C, simultaneously monitoring temperature and pore pressure. The results obtained on two mortars with the same water-to-binder ratio equal to 0.34 are presented, the former with PP-fibers and SAP and the latter with SAP only. Since the addition of SAP leads to high moisture contents, the risk of spalling is expected to increase with respect to HPC without internal curing. Spalling occurred in the mortar with SAP only in correspondence of the drying front at a temperature of approximately 260 °C. On the contrary, no spalling took place in the PP + SAP mortar. Thanks to the combined measurements of temperature, pore pressure and moisture distribution, the behavior of the mortars during heating has been investigated comprehensively. This approach is expected to provide new insight in the study of fire spalling mechanisms.

No considerable difference could be observed regarding temperature profiles between the two samples (with and without PP-fibers). The positioning of thermocouples, however, allows for only limited resolution of the temperature profiles; nevertheless, this gap can be bridged by the simultaneous measurement of the moisture profile by means of neutron radiography. Smoother moisture profiles could be observed for the mortar with PP-fibers, suggesting in this case also a less steep variation of the temperature. This could significantly reduce thermal stress and pressure concentration and thus spalling risk. The smoother moisture profile and the faster movement of the drying front are most likely due to increased permeability occurring thanks to PP-fibers melting. In the sample with SAP only, the moisture profiles experience a sharp change in slope, indicating a clear drying front, in correspondence of which spalling occurred.

The comparison between the moisture profiles and the pressure development allows inferring that the peak pressure occurs within the drying front. Thus, the more localized and more slowly advancing drying front observed in the sample without PP-fibers supports also a narrower pressure peak, which develops closer to the heated face.

4.2. EVALUATION OF THERMALLY INDUCED DAMAGE WITH ULTRASOUNDS

4.2.1. Samples and protocol

The aim of this part was to characterize thermal cracking in normal (OC) and high performance (HPC) concretes by means of ultrasonic (US) non-destructive methods, both linear and non-linear. Two linear methods Pulse Velocity (PV) and Resonance Ultrasonic Spectroscopy (RUS) and nonlinear ultrasonic technique Nonlinear Resonant Ultrasound Spectroscopy (NRUS). Additionally, the US methods were aided with X-ray Tomographies that are described in part 4.3 of this thesis were used. Measurements were performed on all mortar mixes from Table 2.2 of this thesis: OC, HPC-ref, HPC+PP, HPC+SAP, HPC+PP+SAP respectively. Two cylindrical mortar specimens of 100 mm in length and 25 mm in diameter were used for each mix composition. These three US measurement techniques were performed on very same samples before thermal loading (virgin state) and after, thus enabling them to exclude variations caused by location of aggregates if physically different samples of the same mix were used.

After casting, specimens were stored at >95 %RH and 20 ± 0.3 °C climatic chamber and demoulded at one day. Then specimens were moved to 90 %RH and 20 ± 0.3 °C room till 28 days of age to ensure good curing. After reaching 28 days of age, samples were moved to climatic chamber with 36% RH and 20 ± 0.3 °C to decrease influence of high moisture on propagation of ultrasonic waves for 2 months. Then first set of US measurements and XTM were performed on the samples prior to thermal loading. Next, thermal loading was carried out. For thermal loading, 4 temperatures were used:

T1 – 120°C
T2 – 200°C
T3 – 400°C
T4 – 600°C

Heating rate of 16.2°C/min was chosen to agree with rest of the tests with thermal loading. The maximal temperature was held for 8 hours, followed by free cooling down in the furnace for approximately 8 hours.

Mass and geometry were measured before and after thermal loading. X-rays tomography was performed directly after thermal loading when samples cooled down. Before US measurements, samples were kept in 36% RH room, as before the thermal loading. This procedure allowed to measure changes in waves propagation caused by decomposition and cracking of samples, while minimizing the effect of different moisture levels.

Both qualitative and quantitative analysis of the signal are commonly reported in the literature and are also presented in this study as a reference to my results.

4.2.2. Methods

Ultrasound pulse velocity (UPV)

To obtain speed of propagation of ultrasound waves, samples were placed between two transducers; grease was applied on the contact surface of the samples and transducers to facilitate wave propagation on the interface. The positioning of the sample is presented in

Figure 4.8. The Panametrics® Model 5058PR High Voltage pulser-receiver was used for excitation of the signal. Pulse voltage was equal to 200V. Direct connection of the triggers between source and receiver cards was used to set time-zero. The time of flight was defined as a first upcoming sinusoidal peak that is distinguishable from the noise[141], this allows to decrease the operator bias in interpretation of results. An example of UPV received signal for HPC-T1-1 sample before thermal treatment is given in Figure 4.9.

Figure 4.8. Positioning of HPC sample between two transducers for UPV measurements.

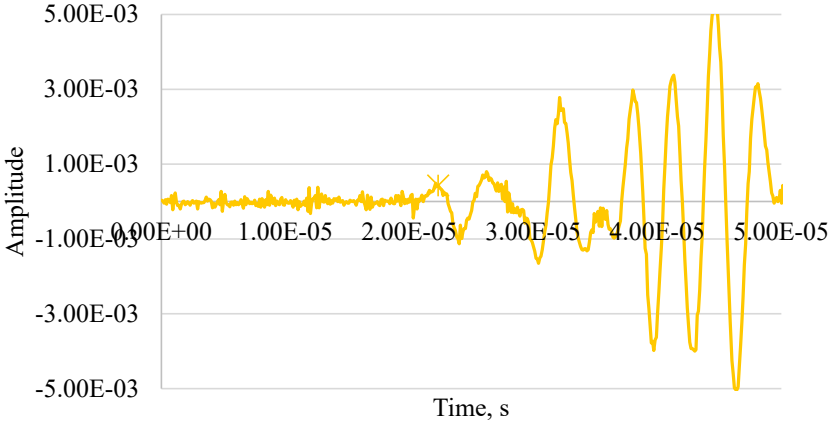

Figure 4.9. Example of HPC-T1-1 UPV signal, sample before thermal loads.

As the final results of UPV are expressed as speed (in km/s) the length of the elongated samples needed to be determined. This was done with a precision of 0.005 mm using a caliper.

Resonance ultrasound spectroscopy (RUS)

The input values of the analysis are sample geometry and density. After exciting the sample at a large frequency range, one can extract the resonance peaks (experimentally measured values for the input) corresponding to various eigenmodes of vibration. Then, based on the

experimental and input values, an inversion algorithm provides the full elastic tensor of the sample[142]. Payan[142] describes in details investigation of thermal damage by means of non-destructive US technics.

Frequency range from 1 kHz to 100 kHz with interval of 10 Hz was chosen. Drive amplitude was equal to 250 Vpp (Volts peak-to-peak), ring-up time was equal to 10 ms. Mass and dimensions of the samples were recorded before the measurements. An exemplary RUS spectrum for the HPC sample without thermal loading is given below in Figure 4.10.

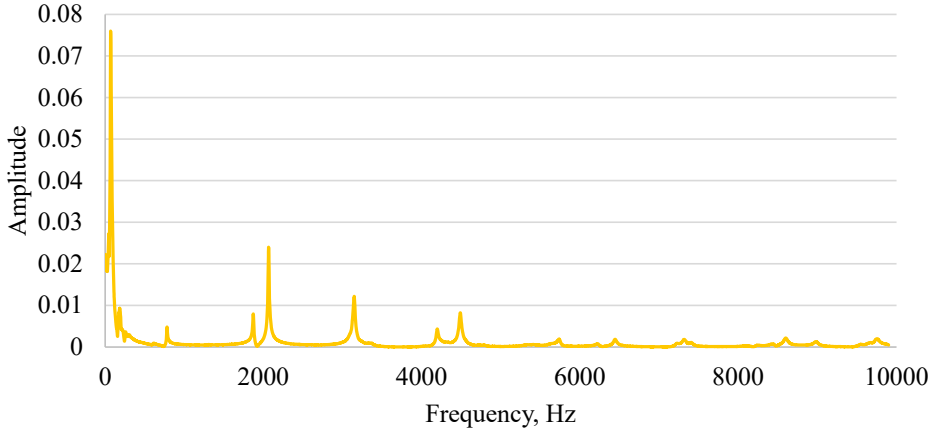

Figure 4.10. Example of RUS signal, HPC without thermal loading.

RITA software developed in LANL is used for hardware control, recording of the signal and initial analysis, e.g. detection of the peak values. The peak finder function of RITA was used in both RUS and NRUS methods to locate peak position. As peak finding algorithm, I used parabolic peak finder with restricted fitting range to decrease computational time and automatize post processing of the data, limiting the output file to 1 single peak. The obtained peak value (in this method we are interested only in a peak location and not its height) is processed according to ASTM C215-14, as an input peak values I chose the first highest amplitude mode, e .g. at about 2000 Hz for a sample shown in Figure 4.10. The very first high values is the resonance of the system, those are to ignore. Second and third signal peaks can increase precision of evaluation of the damage, this data is collected but will not be quantified here. For the simplification, I assume 1D longitudinal resonance, where resonance wavelength is strictly two times the length of the sample.

Nonlinear Resonance Ultrasound Spectroscopy (NRUS)

For nonlinear RUS studies, a transducer able to drive the sample at high amplitude is needed. The laser vibrometer records the velocity at the center of the free end of the sample. The RITA software developed at LANL has been employed for data acquisition and analysis. It allows generating signals at various amplitudes and frequencies, and analyzing the resonance curves Surface vibration measurements performed with a laser vibrometer Polytec OFV-505 laser head, Polytec OFV-5000 controller with VD-02 analog decoder.

Measurement errors and low precision are among the key points to solve in order to broadly apply nonlinear methods to practical problems and increase their sensitivity of detection of subtle variations in microdamage[143]. Three main problems while performing NRUS measurements can be distinguish:

- poor contact between sample and transducer;
- conditioning effect due to the actual measurement, e.g. previous excitation;
- changes of temperature during the test caused by excitation of the sample.

Effect of poor contact can be observed at high amplitudes, when the resonance peak significantly shifts to lower frequencies without increasing resonance amplitude, at the same time reapeted resonance frequency at the lowest strain level does not match the initial reference curve.

To minimize conditioning effect the initial reference resonance curve was performed at low drive amplitude (3 Vpp), than the excitation level was increased (+5 Vpp) and a new resonance curve was obtained. Then the initial resonance reference curve was repeated at the lowest drive amplitude (3 Vpp), this procedure was repeated with the step of increasing drive amplitude equal to 5 Vpp. Protocol of drive amplitudes: [3 Vpp, 8 Vpp, 3 Vpp, 13 Vpp, 3 Vpp, …, 88Vpp], 34 in total, 17 references and 17 increased amplitudes. To further minimize conditioning and memory effect, a delay of 3 seconds between each drive level tests was used, this is known as Haupert[143] protocol.

To account for error caused by changes of temperature during the test, temperature of the sample was measured in contactless way using an infrared thermocamera with a resolution of 0.1°C.

Frequency step of 2Hz was used for samples prior to thermal loading and 1Hz for thermally loaded samples.

To connect the transducers to the samples phenyl salicylate was used. The samples and transducers were placed on a foam block to avoid contact nonlinearity. To check linearity of the system a dummy cylindrical sample made of acrylic glass of the same size as samples studied was tested in NRUS mode. General curves obtained with RITA program are presented below in Figure 4.11.

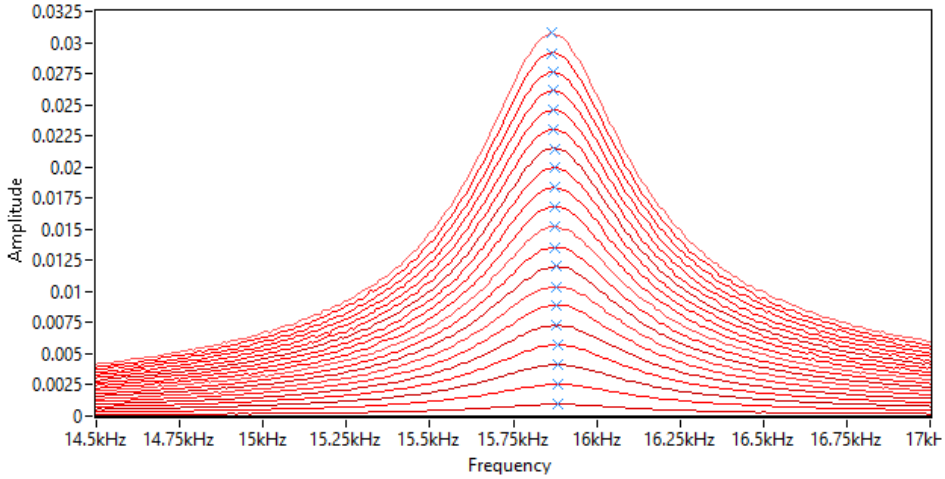

Figure 4.11. Linearity of the experimental system checked with a dummy acrylic glass sample.

The actual peak values from Figure 4.11 are reported in Table 4.1.

Table 4.1. Peak values of SIMONRUS carried out on a dummy acrylic glass sample.

Frequency - Saved Peaks	Amplitude - Saved Peaks
15.8829kHz	0.000944044
15.8826kHz	0.00254417
15.8823kHz	0.00409649
15.8816kHz	0.00566475
15.8805kHz	0.00724382
15.8806kHz	0.00887571
15.8783kHz	0.010391
15.8781kHz	0.0119959
15.8762kHz	0.0135661
15.876kHz	0.0151994
15.875kHz	0.0167995
15.8745kHz	0.018329
15.8735kHz	0.0199179
15.8729kHz	0.0214836
15.8721kHz	0.0230226
15.8713kHz	0.0245624
15.8707kHz	0.0261518
15.8702kHz	0.0276047
15.8678kHz	0.0291458
15.867kHz	0.0307357

During the NRUS, measurements temperature of the sample and transducer was measured with infrared thermocameras (see Figure 4.12) to account for a possible shift of the resonance frequency and amplitude due to temperature changes caused by the measurement protocol.

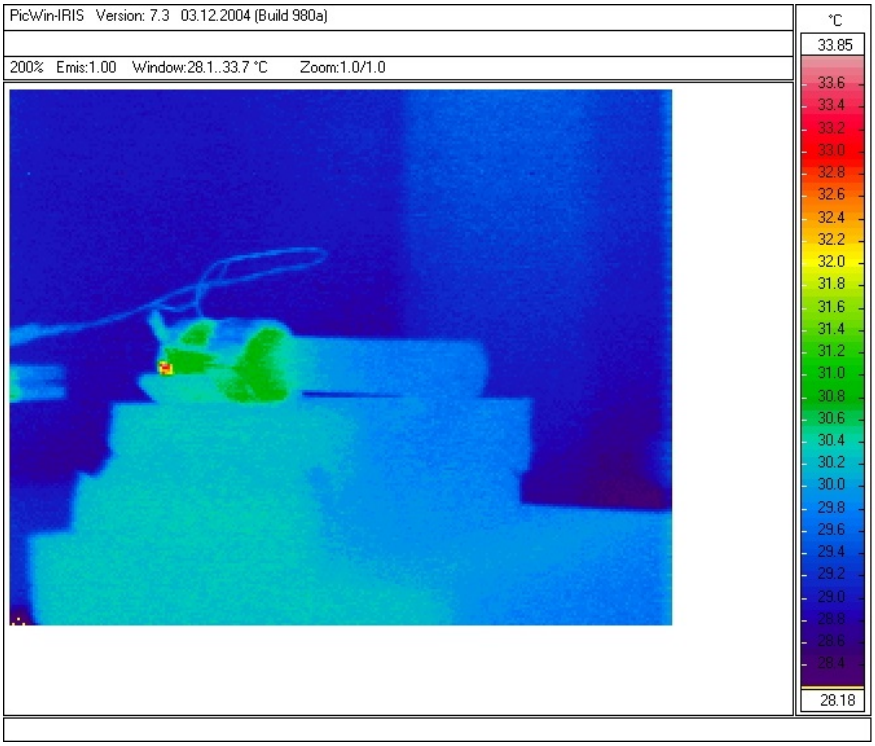

Figure 4.12. Temperature control with IR cameras.

The nonlinear parameter can be extracted from obtained NRUS data, as it describes the slope of the line that connects peaks of the same resonance mode at different drive amplitudes and can be calculated from Equation 4.5.

Equation 4.5

$$\frac{f - f_0}{f_0} = \alpha \Delta \varepsilon$$

Where f and f_0 are the current linear resonance frequency and the first resonance frequency at low amplitudes, correspondingly. α is a parameter of non-linearity. Higher alpha means higher nonlinearity and is a proxy of higher damage.

Location of the peaks with corresponding amplitude and frequency values were calculated in RITA software. Applying Peak Finder algorithms, the fitting range was restricted to 0.5 kHz around the resonance peak, no threshold applied and the width parameters for thermally not treated samples was set at 10. To process the datasets of thermally treated samples at 400 °C and 600 °C I chose higher values when needed, e.g. 15-30, to be able to find one single peak at the right location and to exclude manual picking of the data. The output values, similar to ones presented in Table 4.1 are used to calculate the coefficient of non-linearity α, from the model of regression function (see Equation 4.6):

Equation 4.6

$$y = a \times x^b$$

Where y is the absolute value of the resonance frequency change and x is the resonance amplitude; a is the actual α coefficient we are calculating and parameter b describes the fitting

principle, that can be either 1 (for mostly linear relation between change of relative frequency shift vs. relative amplitude shift) or 2 (for the changes that one can describe with parabolic function). More complex fitting parameters are possible, they describe the dependence within one single sample measurement, however, most likely if one uses a function as power law exponent, the final power law's constants α will not be comparable, as different power laws were used. Corresponding power law's exponents and constants were calculated based on both fitting models for all the datasets and exponent $b = 1$ had a better fit in 52 out of 56 cases.

Table 4.2.

Approximation of power law's parameters to choose best fitting model.

Mix	Designation	Temperature of treatment, °C	Before thermal treatment		After thermal treatment	
			b	a	b	a
OC	T1-1	120	2.451859	180	1.113329	1102
	T1-2	120	1.333118	327	1.15059	717
	T2-1	200	1.048812	271	0.965553	1364
	T2-2	200	1.310225	249	0.977656	1190
	T3-1	400	1.024295	337	0.776711	3330
	T3-2	400	1.192412	337	0.943739	4459
	T4-1	600	0.929019	395	0.772599	5318
	T4-2	600	0.952773	307	0.822697	5891
HPC	T1-1	120	1.117296	1236	1.721739	1412
	T1-2	120	1.15152	791	1.328289	641
	T2-1	200	0.847247	1634	0.634082	2279
	T2-2	200	1.291874	842	1.138795	999
	T3-1	400	1.1447252	1114	0.978224	3278
	T3-2	400	1.100626	1486	1.020237	3021
	T4-1	600	1.315689	1065	0.828933	5526
	T4-2	600	1.152024	553	0.806673	6112
HPC+PP	T1	120	1.521544	418	1.274551	682
	T2	200	0.96819	453	1.077768	1183
	T3	400	1.192818	675	0.840342	3383
	T4	600	1.244147	288	1.022934	15638
HPC+SAP	T1	120	2.457501	1578	1.131792	635
	T2	200	1.195648	289	1.115227	1041
	T3	400	0.933711	1012	0.808626	3690
	T4	600	1.174571	634	0.782958	5467
HPC+PP+SAP	T1	120	1.652599	366	1.293876	476
	T2	200	1.253527	617	1.1623	1181
	T3	400	0.942416	473	0.886294	3482
	T4	600	1.12996	663	0.785482	5515

Qualitative results of SIMONRUS analysis are presented below, but the choice of single fitting parameters allows quantitative analysis of the data. Example of the choice of power law's exponent is provided below in Figure 4.13.

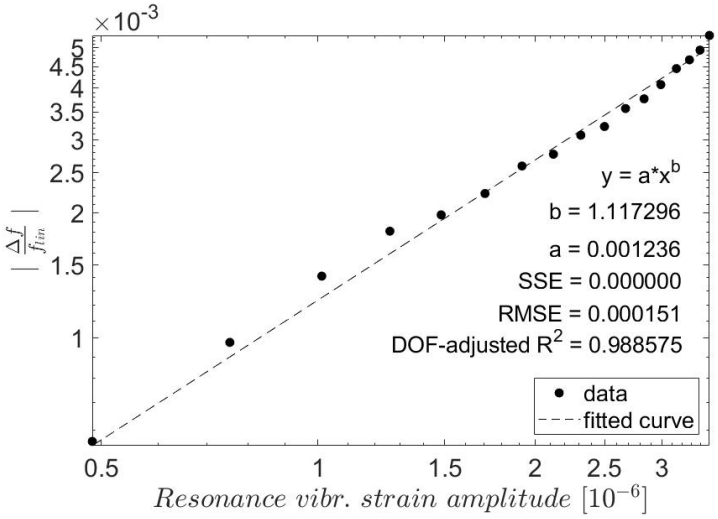

Figure 4.13. Best fitting parameters, example of HPC-T1-1 before thermal treatment.

Best fit of the power law's exponent b is $b = 1.117296$, thus, a linear model with $b = 1$ can provide quantitative analysis of the thermal damage for most of the datasets (see Table 4.2), including HPC-T1-1 before thermal treatment (see Figure 4.13). Running the numbers for very same dataset with fixed exponent $b = 1$, the following results of fitting are obtained (see Figure 4.14), including the comparable α coefficient for quantitative analysis.

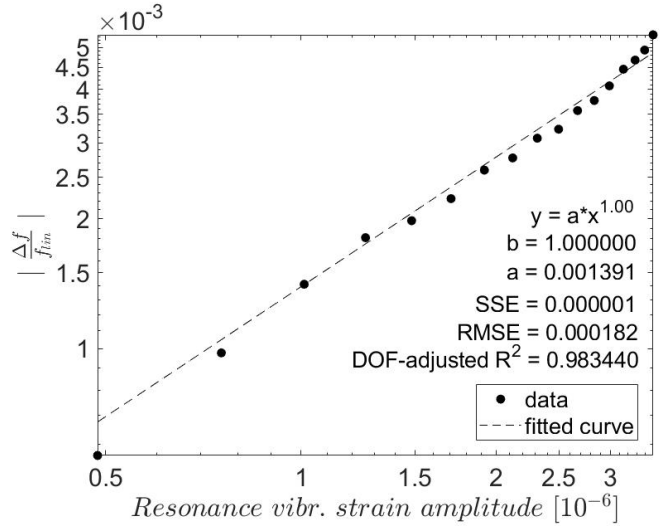

Figure 4.14. Power law fitting model with a fixed exponent b=1, Example of HPC-T1-1 before thermal treatment.

4.2.3. Results

Ultrasound pulse velocity

In Figure 4.15, the effect of thermal treatment on ultrasonic pulse velocity is presented. Often used interpretation[144] of UPV is as summarized in Table 4.3.

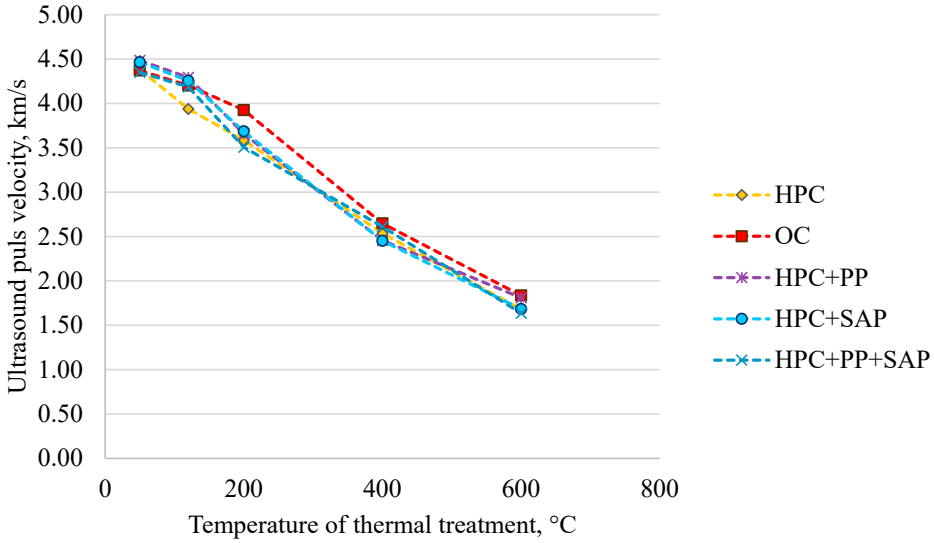

Figure 4.15. Effect of thermal treatment on ultrasound pulse velocity.

Table 4.3.

Classification of concrete quality based on the UPV values

UPV, km/s	Interpretation of quality
above 4.0	Very good quality of concrete
3.5-4.0	Good quality of concrete, extra air and higher porosity are possible
3.0-3.5	Quality of concrete is satisfying, but loss of integrity is suspected
below 3.0	Poor quality of concrete, loos of integrity exists

Resonance Ultrasound Spectroscopy

Qualitative analysis of RUS signal with RITA software gives a general resonance peaks. Shift of longitudinal resonance frequency to the left can be seen below in Figure 4.16. Here I plot a limited signal frequency range for the sake of visualization of the data. The height (amplitude) of the peaks is not representative of a qualitative change within material; it is mostly related to boundary conditions, e.g. contact between samples and transduced.

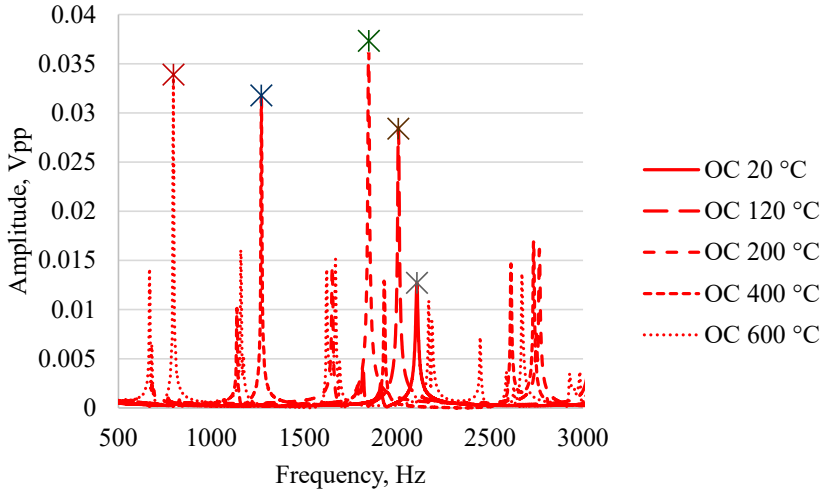

Figure 4.16. RUS signal of thermally treated OC samples.

A general RUS data for HPC, similarly to OC (see Figure 4.16 above) indicates a decrease of resonance frequency, e.g. shift to the left (see Figure 4.17) after thermal loading.

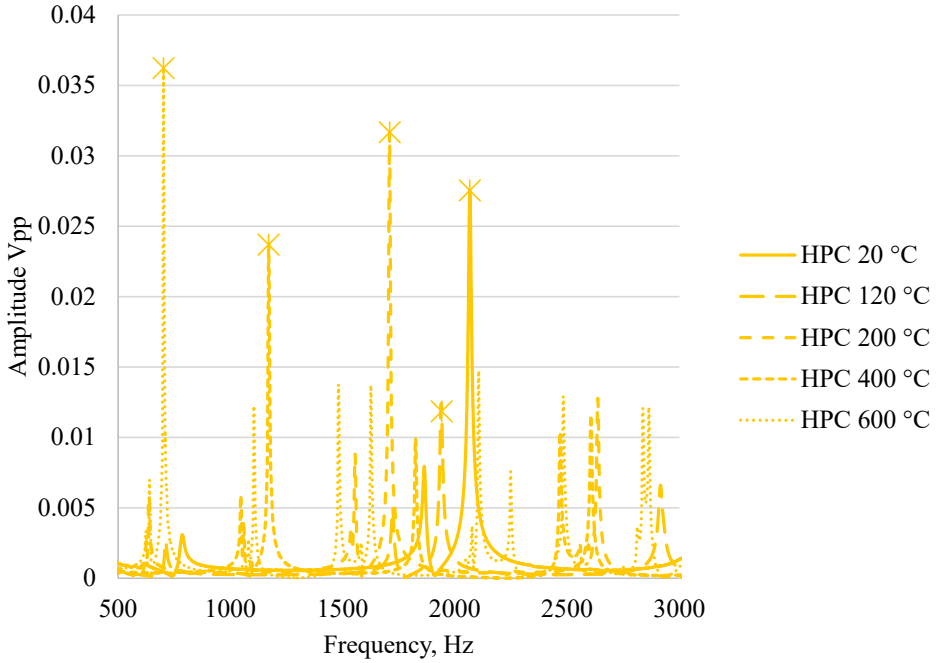

Figure 4.17. RUS signal of thermally treated HPC samples.

RUS results of OC and HPC presented above are plotted for one single sample at each range of temperature. An evolution of residual dynamic Young's modulus for all the samples is

presented below in Figure 4.18. All the samples without thermal load have dynamic modulus in the range of 40 - 44 GPa.

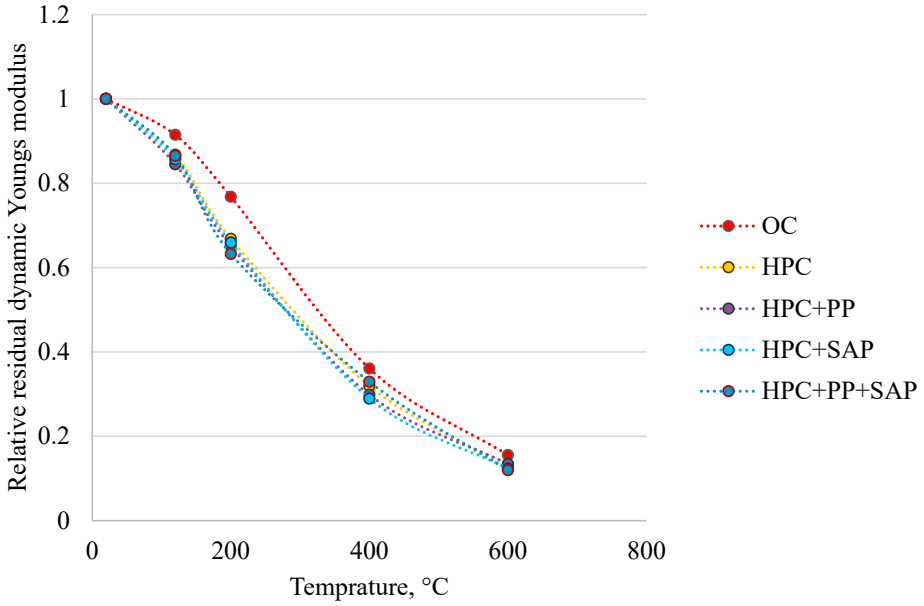

Figure 4.18. Relative residual dynamic Young's modulus.

Nonlinear Resonance Spectroscopy

The linearity of the non-loaded samples is presented below in a single figure (see Figure 4.19), as all the NRUS signals of the samples from the same mix are averaged in a single curve. The linearity of the system is described by sample of acrylic glass. Relative changes of amplitude and relative shift of resonance frequency are calculated from the very first low amplitude signal, the rest 16 low amplitudes are used only to remove effect of conditioning according to Haupert[143] protocol and are not presented here. The higher slope is associated to more linear and uniform sample, while as slope drops, this is a sign of non-linearity and micro damage of the sample. As seen from Figure 4.19, the most uniform sample is the reference of the system, the sample of the same geometry as the samples studied, made of acrylic glass. The less linear is the HPC sample, this is addressed in the following discussions.

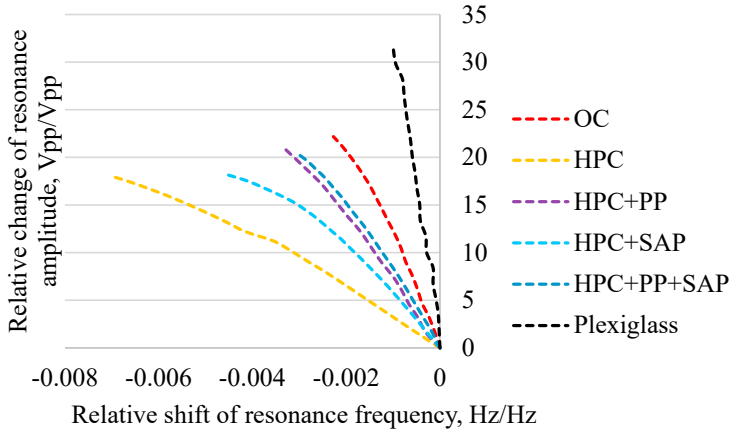

Figure 4.19. Linearity of non-treated samples.

The set of figures below describes linearity of samples after thermal treatment, the data for non-treated samples of OC and HPC are averaged from 8 samples, for other three mixes virgin linearity is an average of 4 samples. Results after thermal treatment are average of two samples for OC and OPC, and results of one single sample for other three mixes. Linearity of the system is described by sample made of acrylic glass, as for the reference.

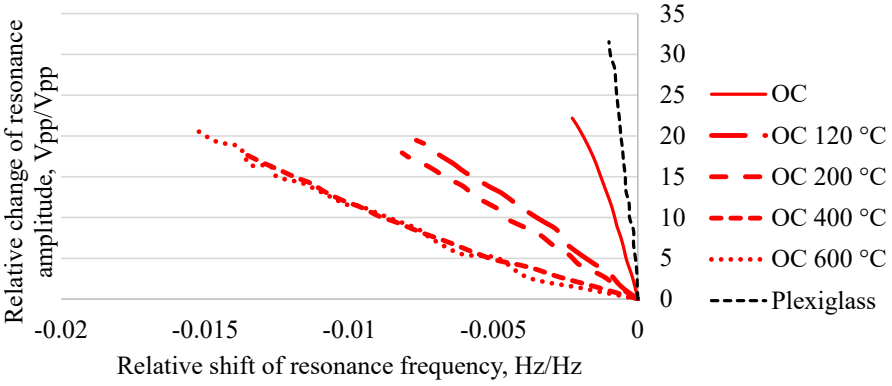

Figure 4.20. Linearity of thermally treated OC samples.

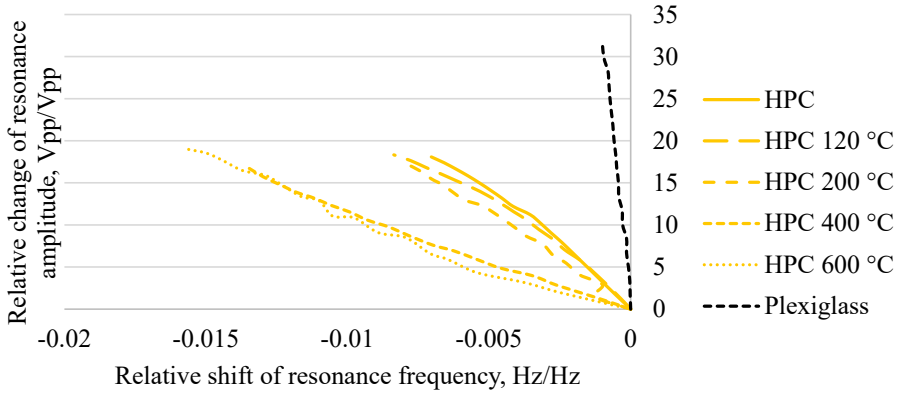

Figure 4.21. Linearity of thermally treated HPC samples.

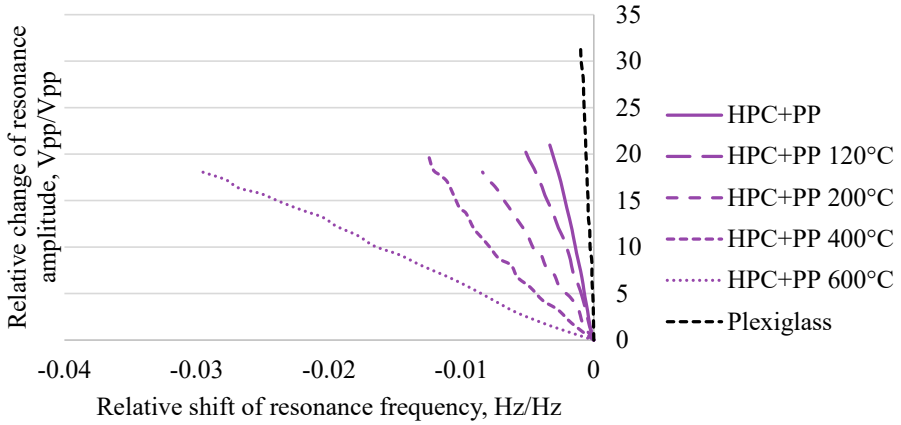

Figure 4.22. Linearity of thermally treated HPC+PP samples.

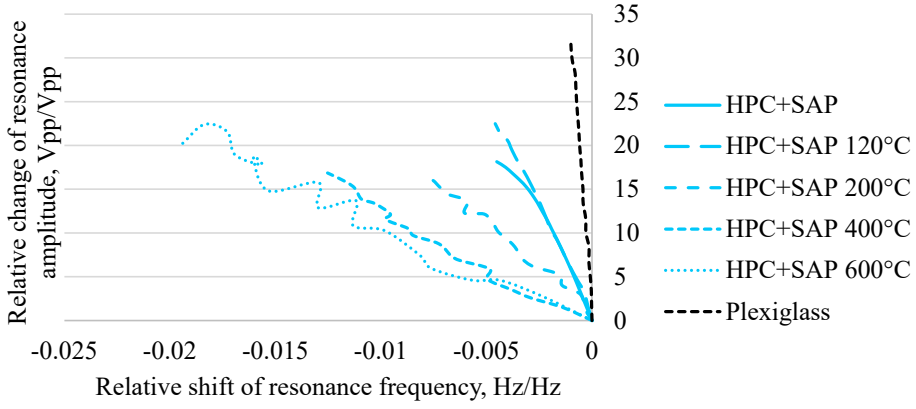

Figure 4.23. Linearity of thermally treated HPC+SAP samples.

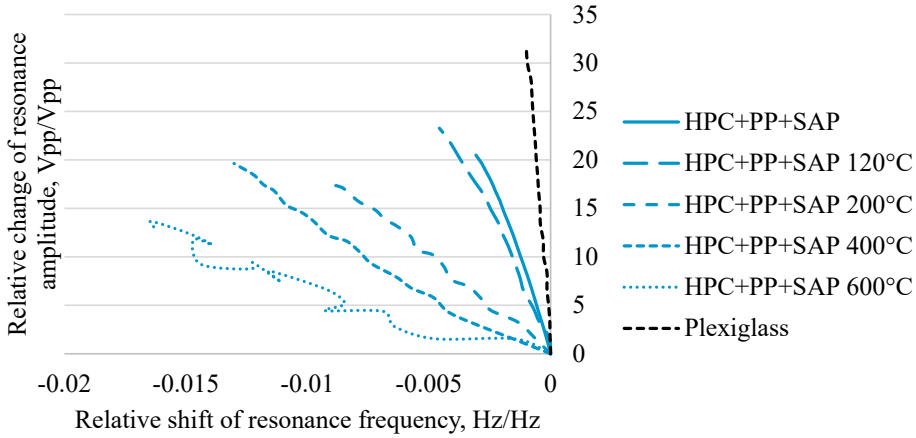

Figure 4.24. Linearity of thermally treated HPC+PP+SAP samples.

The curvature of the lines that corresponds to samples with SAP and treated at 600 °C in Figure 4.23 and Figure 4.24 can be readily explained by Figure 4.25. Where the "noise" of the output signal indicates inhomogeneity of the material rather than unstable laser beam. Settings of the peak finder in RITA program were set to find one peak in a wide frequency region to decrease manual and subjective adjustments and keep the same processing workflow.

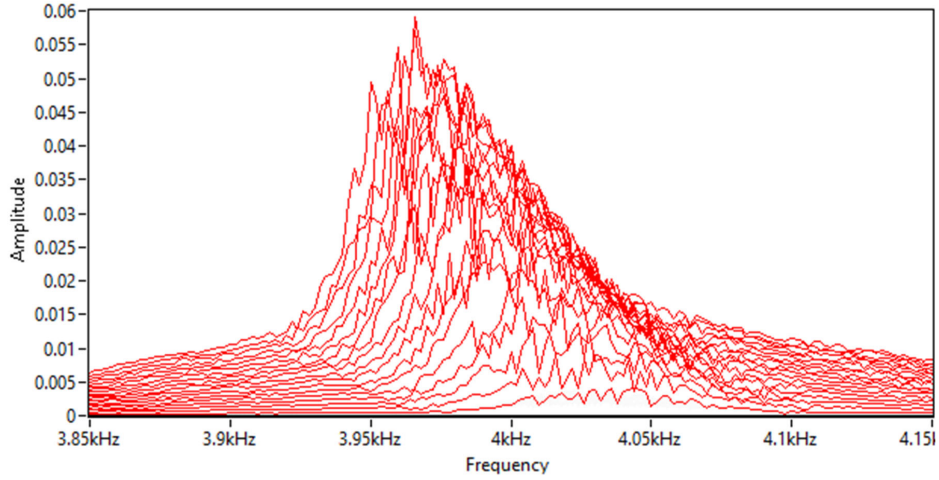

Figure 4.25. Output signal of HPC+PP+SAP sample after treatment at 600 °C.

The resulted peak values were used to calculate the non-linearity coefficient and to give a quantitative evaluation of changes due to thermal load. The obtained α values are summarized in Table 4.4. It can be seen that with increasing temperature of thermal loads the non-linearity increases, indicating damage of the sample. The higher is α values, the more damage the sample has.

Table 4.4.

Changes of non-linearity coefficient α at high temperatures.

Mixes	Temperature of treatment				
	20 °C	120 °C	200 °C	400 °C	600 °C
OC	364.7	1089.5	1222.5	3380.0	4680.0
HPC	1216.1	967.0	1279.0	3142.5	5007.0
HPC+PP	601.8	964.0	1321.0	2824.0	15706.0
HPC+SAP	698.7	762.0	1228.0	2979.0	4505.0
HPC+PP+SAP	656.3	707.0	1468.0	3079.0	4590.0

4.2.4. Discussion

Experimental data obtained in this study are plotted as relative residual UPV and compared to the literature data presented in Part 1.2 of this study (see Figure 4.26).

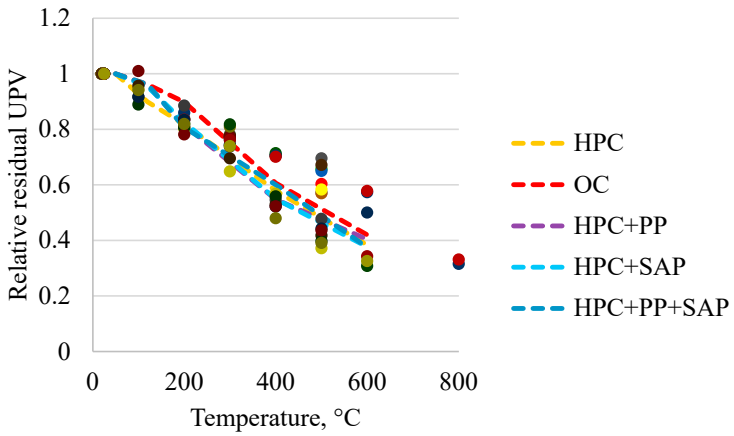

Figure 4.26. Comparison of experimental UPV data with literature.

Experimental data follows the general trend seen in literature, indicating deterioration of the elastic properties of concrete at high temperatures. The initial UPV of all 5 mixes is in the range 4.35 to 4.5 km/s, that is about 10% lower than the samples studied by Sultan[27], Eidan[29] and Kim[31], however, still corresponds to a concrete of a very good quality (see Table 4.3). The explanation for a lower initial UPV values will follow in part 4.3.4.

Presence of empty volumes initially created by SAP are not affecting the evolution of residual UPV significantly, here one could compare those artificially created cavities with ultra-light aerogel incorporations. The study of residual UPV of concrete exposed to high temperatures was done by Ma et al[145]., they exposed concrete samples to temperatures up to 1000 °C and found similar results. The relative decrease in UPV on residual state of samples after exposure to 600 °C was lower, however, here one must mention, that their reference mix had compressive strength of about 40 MPa and initial UPV of about 4 km/s.

To follow the data, one must consider that UPV is a linear function of Young's modulus. The decrease of UPV over temperatures seems linear, e.g. decrease of Young's modulus;

however, different processes are behind this decrease. The initial decrease at temperatures below 100 °C should mostly be due to direct loss of moisture, and no significant thermal damage is expected. At the range 100-200 °C two types of changes takes place, both decomposition of hydration products (e.g. ettringite) and possibly formation of new hydration products in ITZ zone. Dehydration process is more global and affects the whole sample, while solidification in ITZ zone is local and affects UPV less than a dehydration of a straight pass for the US through the paste. To visualize the local effects, nonlinear US methods like SIMONRUS (Single Mode Nonlinear Resonance Ultrasound Spectroscopy) are of interest.

Results of RUS indicates a uniform decrease of dynamic Young's modulus (see Figure 4.18) similar to static Young's modulus (Figure 3.7). However, compared to study of static modulus, no samples experienced explosive spalling, and all were available for measurements.

Very limited data on evaluation of nonlinearity of the thermally damaged concrete samples can be found in the literature, temperature change during the measurements is a known source of measurement error[143], and thus performance of the hot test is a challenge. Application of nonlinear ultrasound methods can be carried out on the samples in a residual state, the general range of obtained α is in a good agreement with literature data, where Payan et al.[142] reported α value for samples treated at 120 °C as 1204 and 966 for OC and HPC respectivelly. The corresponding values in this study are 1089.5 and 967, respectively.

The α value of plain HPC mixes is two times higher than for the HPC with addition of PP, SAP or both. The lower non-linearity for the samples with SAP without thermal loading can be due to the internal curing provided by SAP which allowed to minimize the shrinkage-induced damage while the results of thermally treated cylinders are very similar between the different mixes[66,97,146,147]. The shrinkage-induced damage can explain lower α values of OC, where initial w/c ratio at 0.5 lead to lower autogenous shrinkage and hence less shrinkage cracking. At the same time, for the samples with PP fibers the non-linearity may be lower before the thermal loading thanks to the bridging effect of PP fibers over the cracks. To prove this hypothesis, further detailed shrinkage measurements are of interest, where one has to distinguish damage induced by different types of processes, e.g. autogenous shrinkage, drying shrinkage and thermal damage. Hot SIMONRUS tests are of a high interest and high complexity. On the other hand, thermal loading up to 400 °C led to similar non-linearity values for all mixes.

No effect of temperature fluctuation during NRUS measurements was observed by means of infrared thermal camera, this can be attributed both to sample size, low driving amplitudes and use of Haupert protocol[143].

Combining the outcomes of the three US methods, we can see the different states that samples are undergoing due to thermal loads. For both linear US techniques, we see uniform decrease of UPV and dynamic Young's modulus for all 5 mixes at temperature step from 20 °C to 120 °C, while this is not the case for SIMONRUS measurements (see Table 4.4), where OC samples experience the high rise in nonlinearity, up to 3 times from the initial state. HPC mix has even decreased in nonlinearity. One hypothesis that could explain this reduction of non-linearity is the healing of the cracks originally generated by autogenous shrinkage in a self-healing process. Such rehydration process could be accelerated by the increased temperature and fed by the water that became available from the ettringite decomposed partially already below 100 °C. A similar mechanism likely took place in HPC+PP samples and the linearity of both groups of specimens is very similar at 120 °C. This extends to the next two sample groups,

where HPC+SAP and HPC+PP+SAP samples have lover nonlinearity than HPC at 20 °C due to expected lower shrinkage thanks to the internal curing delivered by the SAP and possibly also the bridging effect of the PP fibers. As the initial shrinkage-induced microcracking is lower in these samples compared to the pure HPC samples, no significant self-healing effect could be observed at the temperature up to 120 °C. The effect of PP fibers can be also deduced from the differences between HPC+SAP and HPC+PP+SAP mixes, as nonlinearity for sample with PP fibers is lower than for one without at both temperatures, i.e. bridging of the cracks with PP fibers.

Regarding the sharp rise of non-linearity of OC samples mentioned above, this has more to do with initial state of the OC samples, where due to higher w/b ratio, the paste of OC is much more porous and cement hydration is of a higher level, e.g. less cement left unhydrated and is available for hydration at higher temperatures. The total porosity and break through radius of OC samples over temperatures has steady increase, this was observed before and is presented in Figure 3.22 and Figure 3.23 above.

This difference in sensitivity of linear and nonlinear US methods comes from the fundamental features of the two methods: the linear methods are sensible for the macro cracking and thus macro changes, while nonlinear methods allow to resolve fine micro cracks and changes in the structure.

These results are very promising and highlight the power of combined linear and nonlinear US methods to evaluate thermal damage of concrete. However, deeper investigation of shrinkage induced cracking, healing of the cracks and changes in ITZ zone at the lower (up to 200 °C) temperatures are of interest.

Besides the investigation of micro damage by means of US techniques, the close to linear correlation between the residual UPV and temperature the samples were exposed to is observed. This has a high practical application to post factum determines the actual temperature of concrete structure during a fire event. Where the UPV measurements can be performed on potentially damaged parts of the structure and the part of structure of the same concrete mix, which had no exposure to fire. This comparison of residual UPV would provide both information on the potential scale of damage and would map the area that was exposed to high temperatures, indicating the "hot spots" of the event.

Supplementary, the cores can be taken for mechanical tests, as the results of static Elastic modulus, in general, follow the linear trend versus temperatures of exposure. The result of compressive strength shows less of a linear trend.

4.2.5. Summary/Conclusions

Combination of linear and nonlinear US methods is very perspective to access thermal damage of concrete structures.

At the lower temperatures or a very short-term thermal exposure, local changes of solid HPC matrix can increase linearity of the material, thus almost providing a beneficial effect.

Practical application of UPV measurements can mislead the user, as drop in UPV does not directly mean the drop of mechanical properties. The decrease of residual UPV over temperatures up to 200 °C must be associated both with decrease of the moisture content in samples and micro cracking. The decrease of moisture is seen as well from static and dynamic elastic modulus (to note, as dynamic elastic modulus is measured with RUS method, it is

directly affected by decrease of UPV as well). However, the increase of porosity is not following the same trend as not-bounded water is removed with solvent exchange protocol and only the residual state of microstructure is measured. The compressive strength of HPC mortars meanwhile is increasing over moderate temperatures.

The obtained NRUS data supports the hypothesis of further hydration at ITZ zones and healing of micro cracks induced originally by autogenous shrinkage during hardening and/or drying shrinkage at temperatures up to 200 °C.

4.3. EVALUATION OF THERMALLY INDUCED DAMAGE WITH µCT

4.3.1. Samples and protocol

Physically the same samples were used for µCT study of thermally induced damage as for US campaign, however, no duplicates for each range of temperatures unlike for US-measurements.

4.3.2. Methods

Full rotation protocol with steps of 0.5° and 721 radiographs in total were recorded for each µCT dataset. Distance from source to detector set at 1016 mm with detector size 1024 × 1024 pixels and conical beam source. Current of 140 uA and voltage of 70 kV were used for samples before thermal treatment; corresponding values for thermally loaded samples were 140 uA and 100 kV. Dataset with pixel size of 0.02659 mm and the same distance between slices was recorded, resulting in voxel size of 18.8×10^{-6} mm. Because of the different contrast obtained for the different samples, respectively, the voxel values in the datasets could not be used for any quantification. Yet, the qualitative comparison was possible, in which the brighter regions generally correspond to higher density, and the darkest regions correspond to air/voids.

Empa's Image Analysis Platform was used for reconstruction, registration and processing of the data. Octopus software was used for reconstruction, while 2D registration and different plugins including rendering of 3D View were done in Fiji/ImageJ. The calculations were performed on 8-bit images, dividing material compounds into a clusters based on grey levels. Similar approach was used to study interface between opalinus clay and concrete[148]. To simplify calculations due to effect of conical beam on the first and last reconstructed slices, the actual data presented below is calculated from the middle part of the samples, at 800 slices out of 1024 initial slices available. Same 800 slices are used in 3D visualizations of air, with first 100 slices kept as original concrete material, for the rest 700 slices aggregates and paste are removed and maximal 8-bit value of 255 assigned to all air related pixels (all pixels with value below 95 after adjusting brightness to level voltage of the source), including those in first 100 slices.

Most of the thermal damage was observed in sub-pixel scale, thus opportunity of quantitative reliable 3D rendering of cracks was limited. However, qualitative analysis of obtained data is discussed below.

4.3.3. Results

Processing of post- and pre- thermally treated μCT data allows us to observe qualitative changes and thermal cracking at different temperature steps. It is important to notice, that every μCT of thermally loaded sample has a μCT data of very same sample before thermal loading, so the actual damage can be visualized.

The following points should be stressed here. Aspect ratio of cylindrical specimens used for US measurements and μCT is very different from samples used for other tests. While Ø 25 × 100 mm cylindrical specimens seem to have similar aspect ratio as prismatic samples used in this study, the positioning of the samples during casting was different: the μCT were cast vertically along the rotation axis of the sample, while the prismatic samples for mechanical properties were tested with the longest dimension horizontal. This means that the path for air to escape the samples during casting/vibtaion is much longer for cylindrical samples than for prismatic samplesand hence the former ones may be more porous. To exclude influence of newly created cracks and displacement, air content is calculated from reconstructed non-treated specimens, as volume of large air voids (darker than a certain gray level threshold value) only, and is summarized below in Table 4.5. Example of volumetric distribution of air bubbles in OC and HPC is given below in Figure 4.27 and Figure 4.28 respectively.

Table 4.5.

Volumetric content of voids, calculated from μCT.

Mix	Volume of voids, %
OC	2.47
HPC	4.42
HPC+PP	3.31
HPC+SAP	5.11
HPC+PP+SAP	5.1

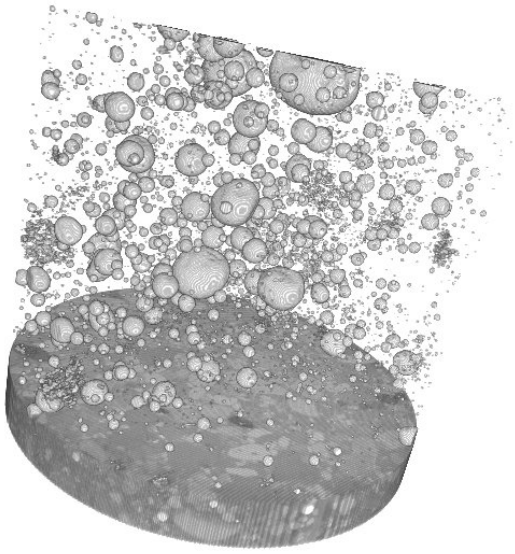

Figure 4.27. Visualization of air bubbles for OC T1-1 sample before thermal treatment.

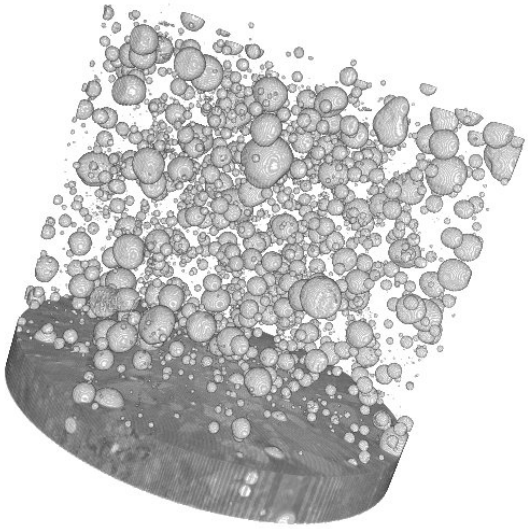

Figure 4.28. Visualization of air bubbles for HPC T1-1 sample before thermal treatment.

It has to be noted, that volumetric content of voids presented above does not directly mean the air content, as some small air bubbles might not be resolved or visualized after reconstruction, registration and correction for beam hardening artefacts, as voxel size is below 18.8×10^{-6} mm^3. Further, in the samples that contained SAP, the voids generated in the original SAP areas (after the SAP released water) could not be distinguished from the entrapped air pores. For those mixes, calculated volume of voids includes both air bubbles and SAP particles and/or voids created by SAP particles. Additionally, to gray level thresholds applied at relatively high level (1 to 95 in 8-bit gray scale), possible noise was removed in Fiji/ImageJ with Despeckle function (Process – Noise – Despeckle).

The qualitative evaluation of thermal damage of HPC samples at 120 °C, 200 °C, 400 °C and 600 °C is presented below in Figure 4.29, Figure 4.30, Figure 4.31 and Figure 4.32 respectively, for a chosen single same slice of the tomograms obtained on the same samples before and after thermal treatment. The images were registered (i.e. aligned in the same position) by comparing their characteristic features, mainly large pores. Effect of SAP presence on thermal damage is presented in Figure 4.33 and Figure 4.34 at maximal temperature of 600 °C.

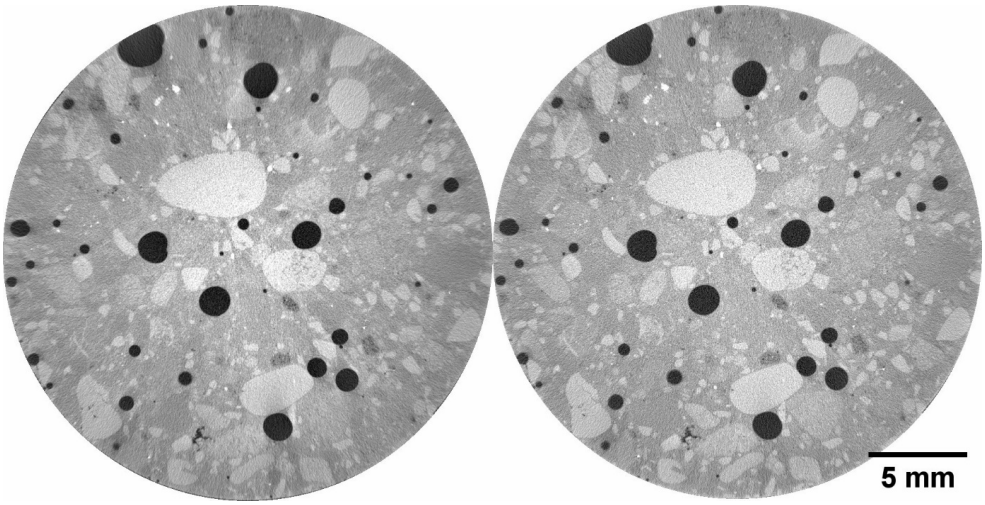

Figure 4.29. Thermal damage of HPC at 120 °C. Left - before thermal load, right - after thermal load.

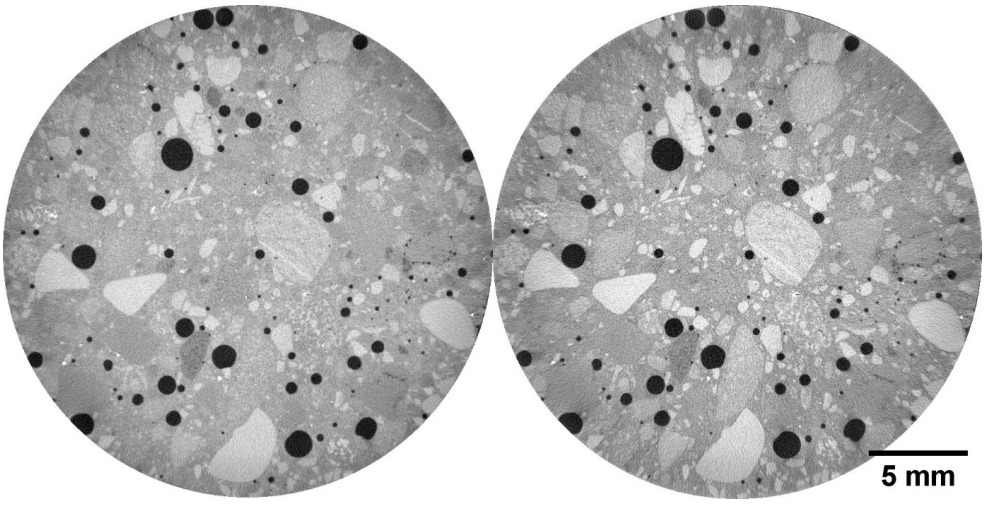

Figure 4.30. Thermal damage of HPC at 200 °C. Left - before thermal load, right - after thermal load.

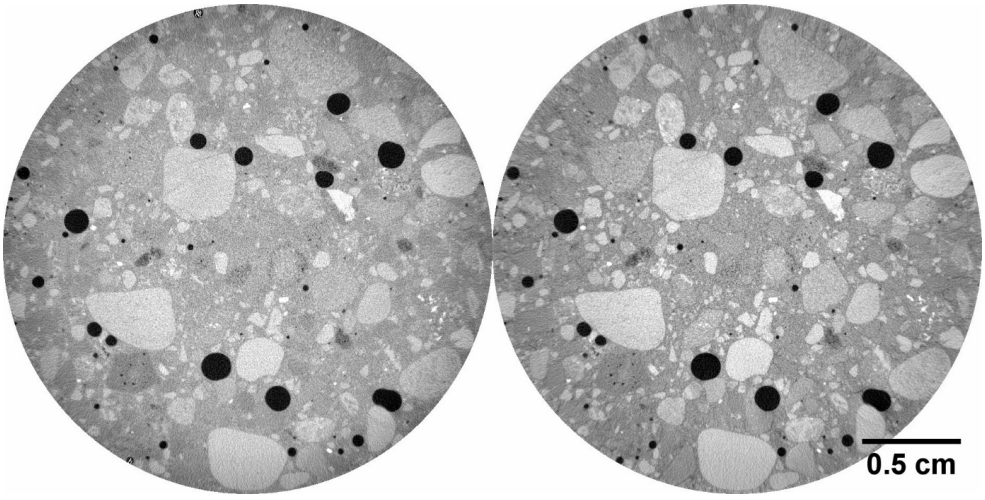

Figure 4.31. Thermal damage of HPC at 400 °C. Left - before thermal load, right - after thermal load.

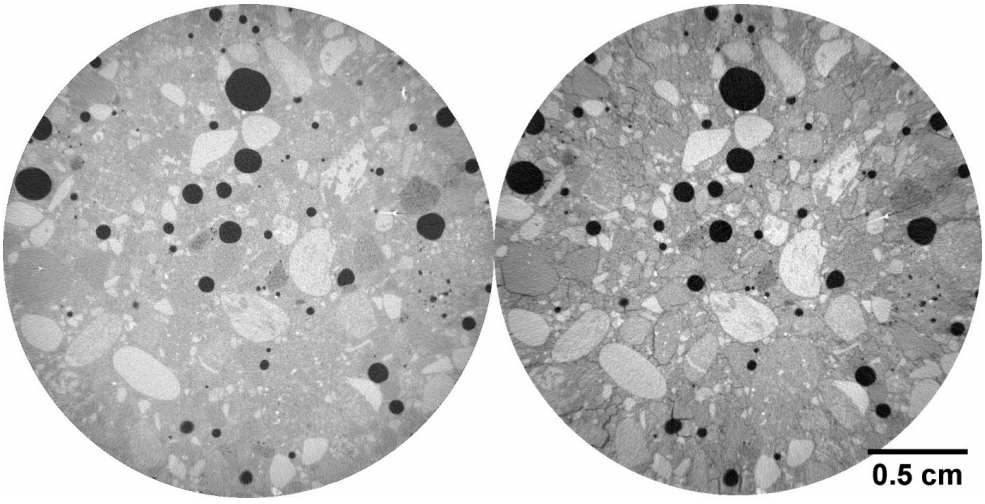

Figure 4.32. Thermal damage of HPC at 600 °C. Left - before thermal load, right - after thermal load.

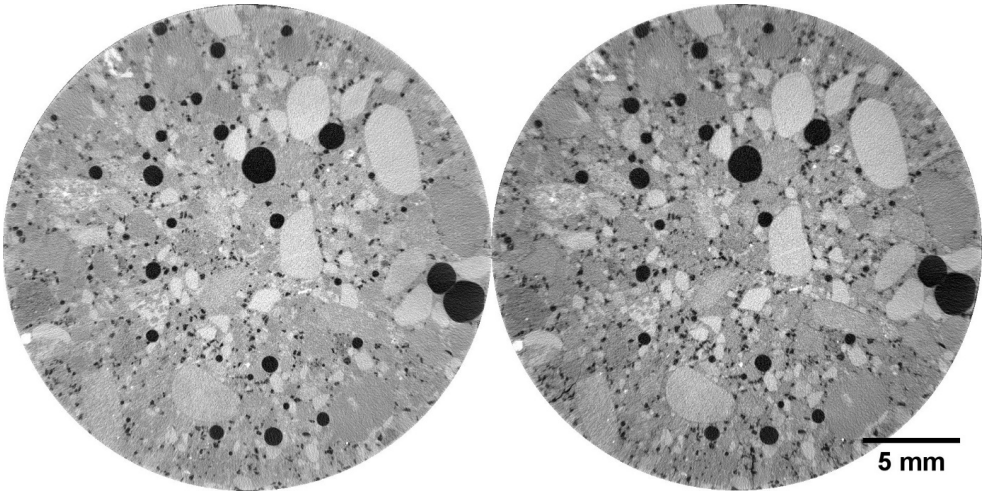

Figure 4.33. Thermal damage of HPC+SAP at 600 °C. Left - before thermal load, right - after thermal load.

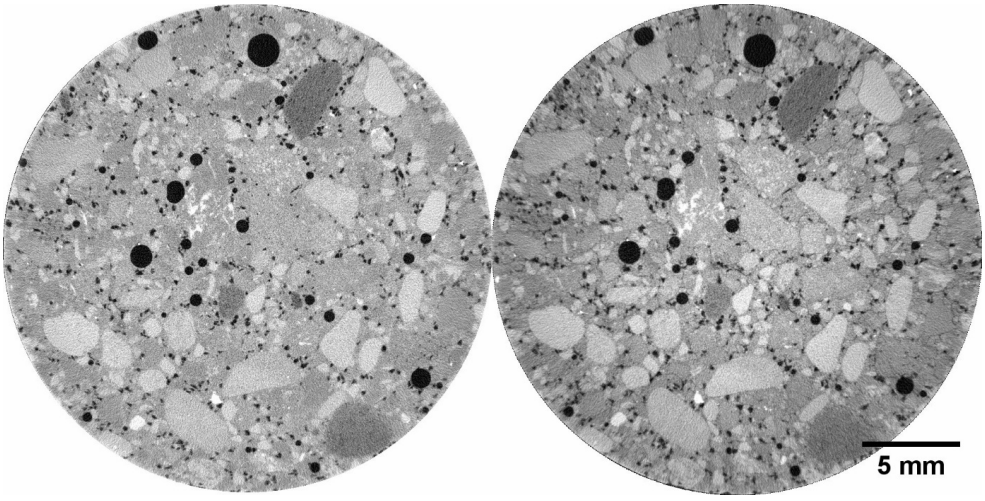

Figure 4.34. Thermal damage of HPC+PP+SAP at 600 °C. Left - before thermal load, right - after thermal load.

4.3.4. Discussion

X-ray tomography allows visualizing thermal damage of all the specimens at each temperature range. As for the main HPC matrix, one can see first cracks at 400 °C (Figure 4.31) and severe damage at 600 °C (Figure 4.32). Alluvial aggregates one can divide in denser ones and less dense ones by the gray level, at 400 °C first damage of HPC appears with very few radial cracks starting from the surface, and the less dense alluvial aggregates are more visible than at virgin state. At 600 °C severe damage is observed for HPC samples with no SAP or PP added. Figure 4.32 shows significant radial cracks starting from the surface and cracks around less bright aggregates, e.g. less dense aggregates, while no cracks observed around denser

aggregates. Radial cracks starting from the surface can be related to the shape of the sample, while cracks around softer aggregates are very persistent.

Figure 4.32, Figure 4.33 and Figure 4.34 clearly visualize positive effect of SAP on limiting thermal cracking, few radial cracks can still be seen in Figure 4.33, while addition of PP fibers eliminates radial cracks at all, as seen in Figure 4.34. Very good and uniform distribution of SAP particles is observed for both mixes with SAP.

Very similar volume of voids in HPC+SAP and HPC+SAP+PP mixes and uniform distribution of voids created by SAP confirms quality of mix design where drop in workability due to addition of PP fibers to SAP mix is compensated by almost double amount of superplasticizer.

Unfortunately, resolution of μCT data does not allow to visualize possible cracks caused by autogenous or drying shrinkage, so μCT data cannot support the hypothesis healing of the cracks and changes in ITZ that is put forward based on US NRUS data, and more detailed study is of a high interest.

Crack formation only around aggregates with a lower brightness/density observed by means of μCT is an interesting observation, as denser aggregates should increase the spalling, while the actual damage here is observed around less dense aggregates. This can be both attributed to thermal expansion of aggregates of different density and quality of ITZ zone. At the same time, the cracks around less dense aggregates contribute to permeability of the matrix, thus the channels created allows to release the pressure and decrease the probability of the explosive spalling due to high temperatures. In opposite, as cracks are not formed around denser aggregates, the permeability of the matrix does not increase in the same way. This explains why mixes with the denser aggregates are more prone to explosive spalling. The more detailed study of transformations in ITZ zone due to thermal loads are of a high interest.

Comparison of gray scale values before and after the thermal loads to access the changes in the matrix due to high temperatures cannot provide absolute values, as different Voltage settings were used for thermally treated and non-treated samples. However, here we can compare the gray levels of paste and aggregates that before thermal treatment had very similar 8-bit gray values, while after thermal treatment, the surrounding paste was relatively darker then the low-density aggregates, thus, indicating increased porosity of the paste, if one assumes that aggregates did not changed.

4.3.5. Summary/Conclusion

Nondestructive test methods, like X-ray tomography, are of a high value in qualitative analysis of the state of material. This allows to visualize the damage and to localize the initial damage, both volume and temperature/time vise.

No obvious cracks observed at temperatures 120 °C and 200 °C, while at 600 °C HPC experienced severe cracking.

The obtained μCT data highlights positive effect of SAP and PP on restriction of thermal damage of concrete, where very limited cracking is observed for samples with SAP and PP, comparing to plain HPC samples.

5. CONCLUSIONS

Both literature review and study of properties of mortars after thermal loads indicate possible increase of mechanical properties at temperatures around 200 °C, a general decrease above 400 °C and deteoration of residual compressive strength for samples loaded above 800°C. As for the case of samples tested here, the highest increase in compressive strength after thermal treatment was achieved for HPC samples at 600 °C and it was +17.58 %, however, the sample itself experienced spalling and this indicates only the potential of material. The highest increase in bending strength was for HPC+PP+SAP samples after 200 °C treatment, that resulted at +18.49 %. The highest relative deterioration of compressive and flexural strength was recorded for OC samples at 600 °C, -51.90 % and -81.32 % respectively. It is here to mark that samples with only PP fibers added experienced higher drop in strength than HPC samples (-50.34 % compressive and -67.23 % flexural), however when SAP was introduced to the mixture, the relative decrease in strength was more moderate (-34.91 % compressive and - 49.58 % flexural), but could lead to a spalling at high temperatures due to higher water content, that correlates with Neutron Radiography study.

The total porosity and breakthrough radius measured by means of MIP both showed increase over temperatures of loading. The total porosity for OC samples after thermal loading at 600 °C increased 2.12 times, while for HPC sample the total porosity increased 3.03 times, indicating higher damage. Important, that the smallest increase after thermal loading to 600 °C had HPC+PP+SAP samples.

This data is supported by general increase of residual transport properties measured by means of oxygen diffusion. The highest increase of transport properties based on oxygen diffusion was observed for HPC samples at 400 °C temperature, it increased 122.21 times, that indicates the damage. At higher temperatures the damage was even more significant, as the equipment went out of range and the state of samples often could not be expressed numerically.

Spalling is likely to occure for HPC mixes exposed to high temperatures. Pressure generated by water vapour and thermal stress combined can lead to explosive spalling. It is important to keep in mind that explosive spalling is not a property of material but complex combination of factors that lead to certain behavior of structure experiencing thermal loads.

Neutron radiography has been performed on mortar slabs exposed to heating up to 550 °C, simultaneously monitoring temperature and pore pressure. The results obtained on two mortars with the same water-to-binder ratio equal to 0.34 are presented, the former with PP-fibers and SAP and the latter with SAP only. Since the addition of SAP leads to high moisture contents, the risk of spalling is expected to increase with respect to HPC without internal curing. Spalling occurred in the mortar with SAP only in correspondence of the drying front at a temperature of approximately 260 °C. On the contrary, no spalling took place in the PP + SAP mortar. Thanks to the combined measurements of temperature, pore pressure and moisture distribution, the behavior of the mortars during heating has been investigated comprehensively. This approach provides new insight in the study of fire spalling mechanisms.

The comparison between the moisture profiles and the pressure development allows inferring that the peak pressure occurs within the drying front. Thus, the more localized and more slowly advancing drying front observed in the sample without PP-fibers supports also a narrower pressure peak, which develops closer to the heated face.

Sufficient thermal insulation and aluminum shielding can protect scintillator from high temperatures and spalling of concrete placed just few centimeters away from it, as the close distance is required for better resolution. The experiments described in this thesis set a path for further studies of spalling by means of neutron radiography.

The non-destructive US methods indicated a clear decrease of residual Young's modulus at each step of thermal loads. With only 15.53 % of dynamic Youngs modulus left for OC samples, 13.12 % for HPC samples, HPC+PP - 14.09 %, HPC+SAP - 12,32 %, HPC+PP+SAP - 11,94 %. While analysis of NRUS data support the idea of local healing of shrinkage cracks for HPC and HPC+PP samples and solidification of ITZ zone.

The important practical conclusion of this work is the linear trend observed for residual UPV over the increase of temperatures. The clear, close to linear, decline of residual UPV allows comparing conditions of structure at different points to draw conclusions on maximal temperature the structural elements were exposed to.

The qualitative data obtained by x-ray μCT besides the cracking in general visualizes that cracks are more likely to form around softer aggregates than denser ones.

The work presented here is the first effort to combine number of non-destructive methods to evaluate damage in concrete due to high temperatures, that made consistently and on uniform set of samples.

6. REFERENCES

1. Damtoft, J. S., Lukasik, J., Herfort, D., Sorrentino, D. & Gartner, E. M. Sustainable development and climate change initiatives. *Cem. Concr. Res.* **38**, 115–127 (2008).
2. Barcelo, L., Kline, J., Walenta, G. & Gartner, E. Cement and carbon emissions. *Mater. Struct. Constr.* **47**, 1055–1065 (2014).
3. Monteiro, P. J. M., Miller, S. A. & Horvath, A. Towards sustainable concrete. *Nat. Mater.* **16**, 698–699 (2017).
4. Kalifa, P., Menneteau, F. D. & Quenard, D. Spalling and pore pressure in HPC at high temperatures. *Cem. Concr. Res.* **30**, 1915–1927 (2000).
5. Flatt, R. & Schober, I. Superplasticizers and the rheology of concrete. in *Understanding the Rheology of Concrete* 144–208 (Woodhead Publishing Limited, 2012). doi:10.1533/9780857095282.2.144
6. Neville, A. & Aïtcin, P.-C. High performance concrete- An overview. *Mater. Struct.* **31**, 111–117 (1998).
7. European Commission. *Competitiveness of the European Cement and Lime Sectors*. (2017).
8. Mindeguia, J.-C., Pimienta, P., Noumowé, A. & Kanema, M. Temperature, pore pressure and mass variation of concrete subjected to high temperature — Experimental and numerical discussion on spalling risk. *Cem. Concr. Res.* **40**, 477–487 (2010).
9. Ulm, F., Acker, P. & Levy, M. The "Chunnel" fire. II: Analysis of concrete damage. *J. Eng. Mech.* **125**, 283–289 (1999).
10. Khoury, G. A. Effect of fire on concrete and concrete structures. *Prog. Struct. Eng. Mater.* **2**, 429–447 (2000).
11. Kodur, V. Spalling in high strength concrete exposed to fire: concerns, causes, critical parameters and cures. *Adv. Technol. Struct. Eng.* 1–9 (2000).
12. Ulm, F. J., Coussy, O. & Bažant, Z. P. The 'Chunnel' fire. I: Chemoplastic softening in rapidly heated concrete. *J. Eng. Mech.* **125**, 272–281 (1999).
13. Jansson, R. Fire spalling of concrete: theoretical and experimental studies. (2013). doi:1103-4270
14. *EN 1992-1-2. Eurocode2: General rules - Structural fire design*.
15. Ingason, H., Li, Y. Z. & Lönnermark, A. Runehamar tunnel fire tests. *Fire Saf. J.* **71**, 134–149 (2015).
16. Lönnermark, A. & Ingason, H. Gas temperatures in heavy goods vehicle fires in tunnels. *Fire Saf. J.* **40**, 506–527 (2005).
17. Lönnermark, A. & Ingason, H. Fire spread and flame length in large-scale tunnel fires. *Fire Technol.* **42**, 283–302 (2006).
18. Ingason, H. & Lönnermark, A. Heat release rates from heavy goods vehicle trailer fires in tunnels. *Fire Saf. J.* **40**, 646–668 (2005).
19. ITA. *Guidelines for structural fire resistance for road tunnels*. (2004).
20. Alhawat, H., Hamid, R., Baharom, S., Azmi, M. R. & Kaish, A. B. M. A. Thermal behaviour of unloaded concrete tunnel lining through an innovative large-scale tunnel fire experimental testing setup. *Constr. Build. Mater.* **283**, 122718 (2021).
21. Leitner, A. The Fire Catastrophe in the Tauern tunnel. *Tunn. Undergr. Sp. Technol.* **16**, 217–233 (2001).
22. Dong, Y. *et al.* Experimental research on fire resistance of the reduced scale immersed

tunnel with fire in both traffic tubes. *Tunn. Undergr. Sp. Technol.* **132**, 104922 (2023).
23. Lo Monte, F., Felicetti, R. & Miah, M. J. The influence of pore pressure on fracture behaviour of Normal-Strength and High-Performance Concretes at high temperature. *Cem. Concr. Compos.* **104**, (2019).
24. Lo Monte, F. & Felicetti, R. Heated slabs under biaxial compressive loading: a test set-up for the assessment of concrete sensitivity to spalling. *Mater. Struct. Constr.* **50**, 1–12 (2017).
25. Felicetti, R. & Gambarova, P. G. Effects of High Temperature on the Residual Compressive Strength of High- Strength Siliceous Concretes. *ACI Mater. J.* **95**, (1998).
26. Canbaz, M. The effect of high temperature on reactive powder concrete. *Constr. Build. Mater.* **70**, 508–513 (2014).
27. Sultan, H. K. & Alyaseri, I. Effects of elevated temperatures on mechanical properties of reactive powder concrete elements. *Constr. Build. Mater.* **261**, 120555 (2020).
28. Alimrani, N. S. & Balazs, G. L. Synthetic fibres or fibre cocktail in terms of shear capacity of concrete after elevated temperatures. *Mech. Mater.* **148**, 103504 (2020).
29. Eidan, J., Rasoolan, I., Rezaeian, A. & Poorveis, D. Residual mechanical properties of polypropylene fiber-reinforced concrete after heating. *Constr. Build. Mater.* **198**, 195–206 (2019).
30. Abaeian, R., Behbahani, H. P. & Moslem, S. J. Effects of high temperatures on mechanical behavior of high strength concrete reinforced with high performance synthetic macro polypropylene (HPP) fibres. *Constr. Build. Mater.* **165**, 631–638 (2018).
31. Kim, Y. S., Ohmiya, Y., Kanematsu, M. & Kim, G. Y. Effect of aggregate on residual mechanical properties of heated ultra-high-strength concrete. *Mater. Struct. Constr.* **49**, 3847–3859 (2016).
32. Liu, J. C. & Tan, K. H. Fire resistance of ultra-high performance strain hardening cementitious composite: Residual mechanical properties and spalling resistance. *Cem. Concr. Compos.* **89**, 62–75 (2018).
33. Irshidat, M. R., Al-Nuaimi, N. & Rabie, M. Hybrid effect of carbon nanotubes and polypropylene microfibers on fire resistance, thermal characteristics and microstructure of cementitious composites. *Constr. Build. Mater.* **266**, 121154 (2021).
34. Beaucour, A. L. *et al.* Influence of elevated temperature on properties of radiation shielding concrete with electric arc furnace slag as coarse aggregate. *Constr. Build. Mater.* **256**, 119385 (2020).
35. Algourdin, N., Sy Hung, B., Mesticou, Z. & Si Larbi, A. Effects of high temperature on mechanical behaviour and physicochemical properties of recycled mortars and its components. *Constr. Build. Mater.* **248**, 118554 (2020).
36. Nayel, I. H., Nasr, M. S. & Abdulridha, S. Q. Impact of elevated temperature on the mechanical properties of cement mortar reinforced with rope waste fibres. *IOP Conf. Ser. Mater. Sci. Eng.* **671**, 0–10 (2020).
37. Papayianni, J. & Valiasis, T. Residual mechanical properties of heated concrete incorporating different pozzolanic materials. *Mater. Struct.* **24**, 115–121 (1991).
38. Saedi Daryan, A., Bakhtiari, M. & Ghasemi, P. An experimental study to evaluate the postfire mechanical properties of concrete specimens. *Struct. Concr.* 1–13 (2020). doi:10.1002/suco.202000011
39. Niknezhad, D., Bonnet, S., Leklou, N. & Amiri, O. Effect of thermal damage on mechanical behavior and transport properties of self-compacting concrete incorporating

polypropylene fibers. *J. Adhes. Sci. Technol.* **33**, 2535–2566 (2019).
40. Chang, Y. F., Chen, Y. H., Sheu, M. S. & Yao, G. C. Residual stress-strain relationship for concrete after exposure to high temperatures. *Cem. Concr. Res.* **36**, 1999–2005 (2006).
41. Noumowe, A. N., Clastres, P., Debicki, G. & Costaz, J. L. Transient heating effect on high strength concrete. *Nucl. Eng. Des.* **166**, 99–108 (1996).
42. Zhai, Y., Deng, Z., Li, N. & Xu, R. Study on compressive mechanical capabilities of concrete after high temperature exposure and thermo-damage constitutive model. *Constr. Build. Mater.* **68**, 777–782 (2014).
43. Zheng, W., Li, H. & Wang, Y. Compressive stress-strain relationship of steel fiber-reinforced reactive powder concrete after exposure to elevated temperatures. *Constr. Build. Mater.* **35**, 931–940 (2012).
44. Chan, Y. N., Peng, G. F. & Anson, M. Residual strength and pore structure of high-strength concrete and normal strength concrete after exposure to high temperatures. *Cem. Concr. Compos.* **21**, 23–27 (1999).
45. Phan, L. T., Lawson, J. R. & Davis, F. L. Effects of elevated temperature exposure on heating characteristics, spalling, and residual properties of high performance concrete. *Mater. Struct. Constr.* **34**, 83–91 (2001).
46. Lau, A. & Anson, M. Effect of high temperatures on high performance steel fibre reinforced concrete. *Cem. Concr. Res.* **36**, 1698–1707 (2006).
47. Choe, G., Kim, G., Gucunski, N. & Lee, S. Evaluation of the mechanical properties of 200 MPa ultra-high-strength concrete at elevated temperatures and residual strength of column. *Constr. Build. Mater.* **86**, 159–168 (2015).
48. Huang, R., Li, S., Meng, L., Jiang, D. & Li, P. Coupled Effect of Temperature and Strain Rate on Mechanical Properties of Steel Fiber-Reinforced Concrete. *Int. J. Concr. Struct. Mater.* **14**, (2020).
49. Liu, J. C. & Tan, K. H. Fire resistance of strain hardening cementitious composite with hybrid PVA and steel fibers. *Constr. Build. Mater.* **135**, 600–611 (2017).
50. Xuan, W., Chen, X., Yang, G., Dai, F. & Chen, Y. Impact behavior and microstructure of cement mortar incorporating waste carpet fibers after exposure to high temperatures. *J. Clean. Prod.* **187**, 222–236 (2018).
51. Collier, N. C. Transition and decomposition temperatures of cement phases - a collection of thermal analysis data. *Ceram. - Silikaty* **60**, 338–343 (2016).
52. Jiang, C., Fang, J., Chen, J. Y. & Gu, X. L. Modeling the instantaneous phase composition of cement pastes under elevated temperatures. *Cem. Concr. Res.* **130**, 105987 (2020).
53. Lencis, U., Udris, A. & Korjakins, A. Frost influence on the ultrasonic pulse velocity in concrete at early phases of hydration process. *Case Stud. Constr. Mater.* **15**, (2021).
54. Zheng, W., Luo, B. & Wang, Y. Stress–strain relationship of steel-fibre reinforced reactive powder concrete at elevated temperatures. *Mater. Struct. Constr.* **48**, 2299–2314 (2015).
55. Li, L. *et al.* Experimental study on dynamic compressive behavior of steel fiber reinforced concrete at elevated temperatures. *Constr. Build. Mater.* **210**, 673–684 (2019).
56. Caetano, H., Ferreira, G., Rodrigues, J. P. C. & Pimienta, P. Effect of the high temperatures on the microstructure and compressive strength of high strength fibre concretes. *Constr. Build. Mater.* **199**, 717–736 (2019).

57. Shorter, G. W. & Harmathy, T. Z. Discussion of the fire resistance of prestressed concrete beams. in *Proceedings of the Institution of Civil Engineers* 313–315 (1961).
58. Saito, H. Explosive Spalling of Prestressed Concrete in Fire. *Bull. Japan Assoc. Fire Sci. Eng.* **5**, 23–30 (1966).
59. Chen, X. T. *et al.* Experimental evidence of a moisture clog effect in cement-based materials under temperature. *Cem. Concr. Res.* **39**, 1139–1148 (2009).
60. Felicetti, R., Lo Monte, F. & Pimienta, P. A new test method to study the influence of pore pressure on fracture behaviour of concrete during heating. *Cem. Concr. Res.* **94**, 13–23 (2017).
61. Ozawa, M. & Morimoto, H. Effects of various fibres on high-temperature spalling in high-performance concrete. *Constr. Build. Mater.* **71**, 83–92 (2014).
62. Sertmehmetoglu, Y. On a Mechanism of Spalling of Concrete Under Fire Conditions. (King's College London, 1977).
63. Bažant, Z. P. Analysis of Pore Pressure, Thermal Stress and Fracture in Rapid Heated Concrete. in *International Workshop on Fire Performance of High-Strength Concrete* (eds. Phan, L. T., Carino, N. J., Duthinh, D. & Garboczi, E.) 155–164 (1998).
64. Choe, G. *et al.* Effect of moisture migration and water vapor pressure build-up with the heating rate on concrete spalling type. *Cem. Concr. Res.* **116**, 1–10 (2019).
65. Lura, P., Jensen, O. M. & Van Breugel, K. Autogenous shrinkage in high-performance cement paste: An evaluation of basic mechanisms. *Cem. Concr. Res.* **33**, 223–232 (2003).
66. Jensen, O. M. & Hansen, P. F. Water-entrained cement-based materials: II. Experimental observations. *Cem. Concr. Res.* **32**, 973–978 (2002).
67. Mechtcherine, V. *et al.* Testing superabsorbent polymer (SAP) sorption properties prior to implementation in concrete: results of a RILEM Round-Robin Test. *Mater. Struct. Constr.* **51**, (2018).
68. Liu, J. C., Tan, K. H. & Yao, Y. A new perspective on nature of fire-induced spalling in concrete. *Constr. Build. Mater.* **184**, 581–590 (2018).
69. Toropovs, N. *et al.* Real-time measurements of temperature, pressure and moisture profiles in High-Performance Concrete exposed to high temperatures during neutron radiography imaging. *Cem. Concr. Res.* **68**, 166–173 (2015).
70. Tao, J., Liu, X., Yuan, Y. & Taerwe, L. Transient strain of self-compacting concrete loaded in compression heated to 700 °C. *Mater. Struct.* **46**, 191–201 (2013).
71. Moreira, M. H., Pont, S. D., Tengattini, A. & Pandolfelli, V. C. Heating rate effect on the moisture clog while drying refractory castables: A neutron tomography perspective. *J. Am. Ceram. Soc.* 1706–1715 (2022). doi:10.1111/jace.18902
72. Xiao, Y. *et al.* Effect of microwave pretreatment on mechanical behavior of concrete and aggregate recovery. *Constr. Build. Mater.* **387**, 131647 (2023).
73. Boström, L., Wickström, U. & Adl-Zarrabi, B. Effect of specimen size and loading conditions on spalling of concrete. *FIRE Mater.* **31**, 173–186 (2007).
74. Jansson, R. & Boström, L. Factors influencing fire spalling of self compacting concrete. *Mater. Struct.* **46**, 1683–1694 (2013).
75. Meyer-Ottens, C. Zur Frage Der Abplatzungen an Bauteilen Aus Beton Bei Brandbeanspruchungen. (TU Braunshweig, 1972).
76. Du, H. & Zhang, M. Experimental investigation of thermal pore pressure in reinforced C80 high performance concrete slabs at elevated temperatures. *Constr. Build. Mater.*

260, 120451 (2020).
77. Lu, F. On the prediction of concrete spalling under fire. (ETH-Zürich, 2015).
78. Kodur, V. K. R., Cheng, F. P., Wang, T. C. & Sultan, M. A. Effect of strength and fiber reinforcement on fire resistance of high-strength concrete columns. *J. Struct. Eng.* **129**, 253–259 (2003).
79. Abdi Moghadam, M. & Izadifard, R. A. Effects of zeolite and silica fume substitution on the microstructure and mechanical properties of mortar at high temperatures. *Constr. Build. Mater.* **253**, 119206 (2020).
80. Dauti, D. *et al.* Analysis of moisture migration in concrete at high temperature through in-situ neutron tomography. *Cem. Concr. Res.* (2018). doi:10.1016/J.CEMCONRES.2018.06.010
81. Czoboly, O. *et al.* Fibers and fiber cocktails to improve fire resistance of concrete. *J. Therm. Anal. Calorim.* **128**, 1453–1461 (2017).
82. Tian, K., Ožbolt, J. & Hofmann, J. Experimental investigation of concrete edge failure for single stud anchors and anchor groups after fire exposure. *Constr. Build. Mater.* **266**, (2021).
83. Du, Y., Qi, H. H., Huang, S. S. & Richard Liew, J. Y. Experimental study on the spalling behaviour of ultra-high strength concrete in fire. *Constr. Build. Mater.* **258**, 120334 (2020).
84. Klingsch, E. W. Explosive spalling of concrete in fire. (ETH Zurich, 2014).
85. Li, Y., Yang, E. H., Zhou, A. & Liu, T. Pore pressure build-up and explosive spalling in concrete at elevated temperature: A review. *Constr. Build. Mater.* **284**, (2021).
86. Akca, A. H. & Zihnioğlu, N. Ö. High performance concrete under elevated temperatures. *Constr. Build. Mater.* **44**, 317–328 (2013).
87. Liu, X., Ye, G., De Schutter, G., Yuan, Y. & Taerwe, L. On the mechanism of polypropylene fibres in preventing fire spalling in self-compacting and high-performance cement paste. *Cem. Concr. Res.* **38**, 487–499 (2008).
88. Bing, C., Ph, D., Zhen, W. & Ning, L. Experimental Research on Properties of High-Strength Foamed Concrete. *J. Mater. Civ. Eng.* **24**, 113–118 (2012).
89. Ozawa, M., Subedi Parajuli, S., Uchida, Y. & Zhou, B. Preventive effects of polypropylene and jute fibers on spalling of UHPC at high temperatures in combination with waste porous ceramic fine aggregate as an internal curing material. *Constr. Build. Mater.* **206**, 219–225 (2019).
90. D'Aloia, L. *et al.* Improving the behavior of concrete exposed to fire by using an air entraining agent (AEA): Assessment of spalling. *MATEC Web Conf.* **6**, (2013).
91. Li, Y., Tan, K. H. & Yang, E. H. Synergistic effects of hybrid polypropylene and steel fibers on explosive spalling prevention of ultra-high performance concrete at elevated temperature. *Cem. Concr. Compos.* **96**, 174–181 (2019).
92. Park, J. J., Yoo, D. Y., Kim, S. & Kim, S. W. Benefits of synthetic fibers on the residual mechanical performance of UHPFRC after exposure to ISO standard fire. *Cem. Concr. Compos.* **104**, 103401 (2019).
93. Witek, A. & Gawin, D. Experimental and numerical study on the efficiency of the polypropylene fibers admixture in reducing pore pressure in heated concrete. *J. Build. Phys.* **38**, 121–137 (2014).
94. Ozawa, M., Uchida, S., Kamada, T. & Morimoto, H. Study of mechanisms of explosive spalling in high-strength concrete at high temperatures using acoustic emission. *Constr.*

Build. Mater. **37**, 621–628 (2012).
95. Lura, P. & Terrasi, G. Pietro. Reduction of fire spalling in high-performance concrete by means of superabsorbent polymers and polypropylene fibers: Small scale fire tests of carbon fiber reinforced plastic-prestressed self-compacting concrete. *Cem. Concr. Compos.* **49**, 36–42 (2014).
96. Zhu, P. *et al.* Study of physical properties and microstructure of aerogel-cement mortars for improving the fire safety of high-performance concrete linings in tunnels. *Cem. Concr. Compos.* **104**, (2019).
97. Justs, J., Wyrzykowski, M., Bajare, D. & Lura, P. Internal curing by superabsorbent polymers in ultra-high performance concrete. *Cem. Concr. Res.* **76**, 82–90 (2015).
98. Serrano, R., Cobo, A., Prieto, M. I. & González, M. de las N. Analysis of fire resistance of concrete with polypropylene or steel fibers. *Constr. Build. Mater.* **122**, 302–309 (2016).
99. Ding, Y., Zhang, C., Cao, M., Zhang, Y. & Azevedo, C. Influence of different fibers on the change of pore pressure of self-consolidating concrete exposed to fire. *Constr. Build. Mater.* **113**, 456–469 (2016).
100. Bentz, D. Fibers, Percolation, and Spalling of High-Performance Concrete. *ACI Mater. J.* **97**, 351–359 (2000).
101. Sideris, K. K. & Manita, P. Residual mechanical characteristics and spalling resistance of fiber reinforced self-compacting concretes exposed to elevated temperatures. *Constr. Build. Mater.* **41**, 296–302 (2013).
102. Wyrzykowski, M. & Lura, P. Controlling the coefficient of thermal expansion of cementitious materials - A new application for superabsorbent polymers. *Cem. Concr. Compos.* **35**, 49–58 (2013).
103. Mechtcherine, V. *et al.* Testing superabsorbent polymer (SAP) sorption properties prior to implementation in concrete: results of a RILEM Round-Robin Test. *Mater. Struct. Constr.* **51**, (2018).
104. Wyrzykowski, M., Igarashi, S. I., Lura, P. & Mechtcherine, V. Recommendation of RILEM TC 260-RSC: using superabsorbent polymers (SAP) to mitigate autogenous shrinkage. *Mater. Struct. Constr.* **51**, 1–7 (2018).
105. Kalifa, P., Chéné, G. & Gallé, C. High-temperature behavior of HPC with polypropylene fibers from spalling to microstructure. *Cem. Concr. Res.* **31**, 1487–1499 (2001).
106. Dauti, D. *et al.* Modeling concrete exposed to high temperature : Impact of dehydration and retention curves on moisture migration. *Int. J. Numer. Anal. Methods Geomech.* **42**, 1516–1530 (2018).
107. Zhang, J. & Scherer, G. W. Comparison of methods for arresting hydration of cement. *Cem. Concr. Res.* **41**, 1024–1036 (2011).
108. Collier, N. C., Sharp, J. H., Milestone, N. B., Hill, J. & Godfrey, I. H. The influence of water removal techniques on the composition and microstructure of hardened cement pastes. *Cem. Concr. Res.* **38**, 737–744 (2008).
109. Diamond, S. Mercury porosimetry. An inappropriate method for the measurement of pore size distributions in cement-based materials. *Cement and Concrete Research* **30**, 1517–1525 (2000).
110. Kaufmann, J., Loser, R. & Leemann, A. Analysis of cement-bonded materials by multi-cycle mercury intrusion and nitrogen sorption. *J. Colloid Interface Sci.* **336**, 730–7 (2009).

111. Washburn, E. Note on a Method of Determining the Distribution of Pore Sizes in a Porous Material. *Proc Natl Acad Sci* **7**, 115–116 (1921).
112. Winslow, D. N. & Diamond, S. A mercury porosimetry study of the porosity in Portland cement. *J. Mater.* 564–585 (1970).
113. Hearn, N. & Hooton, R. D. Sample mass and dimension effects on mercury intrusion porosimetry results. *Cem. Concr. Res.* **22**, 970–980 (1992).
114. Villani, C. *et al.* An inter lab comparison of gas transport testing procedures: Oxygen permeability and oxygen diffusivity. *Cem. Concr. Compos.* **53**, 357–366 (2014).
115. Peretti, C., Leemann, A., Loser, R. & Lura, P. Influence of different conditioning regimes on the oxygen diffusion and oxygen permeability of concrete. in *2nd International conference on microstructure related durability of cementitious composites* 1173–1181 (2012).
116. Lawrence, C. D. Transport of oxygen through concrete. in *The chemistry and chemical-related properties of cement. British ceramic society proceedings 35* (1984).
117. Torrent, R. J. A two-chamber vacuum cell for measuring the coefficient of permeability to air of the concrete cover on site. *Mater. Struct.* **25**, 358–365 (1992).
118. Xiong, M. X. & Richard Liew, J. Y. Spalling behavior and residual resistance of fibre reinforced Ultra-High performance concrete after exposure to high temperatures. *Mater. Constr.* **65**, 1–9 (2015).
119. Kaufmann, J. Pore space analysis of cement-based materials by combined Nitrogen sorption – Wood's metal impregnation and multi-cycle mercury intrusion. *Cem. Concr. Compos.* **32**, 514–522 (2010).
120. Kaufmann, J. Characterization of Pore Space of Cement-Based Materials by Combined Mercury and Wood's Metal Intrusion. *J. Am. Ceram. Soc.* **92**, 209–216 (2009).
121. Zhang, Q. & Ye, G. Dehydration kinetics of Portland cement paste at high temperature. *J. Therm. Anal. Calorim.* **110**, 153–158 (2012).
122. Der Heijden, G. H. A. V., Pel, L. & Adan, O. C. G. Fire spalling of concrete, as studied by NMR. *Cem. Concr. Res.* **42**, 265–271 (2012).
123. Lehmann, E., Vontobel, P. & Wiezel, L. Properties of the radiography facility NEUTRA at SINQ and its potential for use as European reference facility. *Nondestruct. Test. ...* 191–202 (2001).
124. Justnes, H., Bryhn-Ingebrigtsen, K. & Rosvold, G. O. Neutron radiography: an excellent method of measuring water penetration and moisture distribution in cementitious materials. *Adv. Cem. Res.* **6**, 67–72 (1994).
125. Weber, B. *et al.* Neutron radiography of heated high-performance mortar. *MATEC Web Conf.* **6**, 03004 (2013).
126. Kanematsu, M., Maruyama, I., Noguchi, T., Iikura, H. & Tsuchiya, N. Quantification of water penetration into concrete through cracks by neutron radiography. *Nucl. Instruments Methods Phys. Res. Sect. A Accel. Spectrometers, Detect. Assoc. Equip.* **605**, 154–158 (2009).
127. Dauti, D. *et al.* First results on fast neutron tomography of heated concrete. in *5th International Workshop on Concrete Spalling due to Fire Exposure* 249–258 (2017).
128. Dauti, D., Dal Pont, S., Briffaut, M. & Weber, B. Modeling of 3D moisture distribution in heated concrete: From continuum towards mesoscopic approach. *Int. J. Heat Mass Transf.* **134**, 1137–1152 (2019).
129. Dauti, D. *et al.* Some Observations on Testing Conditions of High-Temperature

Experiments on Concrete: An Insight from Neutron Tomography. *Transp. Porous Media* **132**, 299–310 (2020).
130. Jansson, R. & Boström, L. The Influence of Pressure in the Pore System on Fire Spalling of Concrete. *Fire Technol.* **46**, 217–230 (2009).
131. Bangi, M. R. & Horiguchi, T. Pore pressure development in hybrid fibre-reinforced high strength concrete at elevated temperatures. *Cem. Concr. Res.* **41**, 1150–1156 (2011).
132. Pel, L., Jaspers, S., Pereira, F., Pimienta, P. & Carré, H. Combined NMR moisture, temperature and pressure measurements during heating. *MATEC Web Conf.* **6**, (2013).
133. Juárez Trujillo, J., Castro, J. A., Innocentini, M. D. M. & Vernilli, F. Combined transient 3D simulation and experimental methods to assess a slow heat-up curve used to dry a refractory concrete. *Int. J. Therm. Sci.* **185**, (2023).
134. Felicetti, R. & Lo Monte, F. Concrete spalling: Interaction between tensile behaviour and pore pressure during heating. *MATEC Web Conf.* **6**, (2013).
135. Trtik, P. *et al.* Neutron Tomography Measurements of Water Release From Superabsorbent Polymers in Cement Paste. *Int. Conf. Mater. Sci. 64th RILEM Annu. Week Aachen-MATSCI* 1–10 (2010).
136. Wyrzykowski, M., Lura, P., Pesavento, F. & Gawin, D. Modeling of Water Migration during Internal Curing with Superabsorbent Polymers. *J. Mater. Civ. Eng.* **24**, 1006–1016 (2012).
137. Hu, Z. *et al.* A neutron radiography study on the drying of cement mortars: Effect of mixture composition and crack length. *Cem. Concr. Res.* **172**, 107245 (2023).
138. Hassanein, R., Lehmann, E. & Vontobel, P. Methods of scattering corrections for quantitative neutron radiography. *Nucl. Instruments Methods Phys. Res. Sect. A Accel. Spectrometers, Detect. Assoc. Equip.* **542**, 353–360 (2005).
139. Sedighi-Gilani, M. *et al.* Visualization and quantification of liquid water transport in softwood by means of neutron radiography. *Int. J. Heat Mass Transf.* **55**, 6211–6221 (2012).
140. Lukić, B., Tengattini, A., Dufour, F. & Briffaut, M. Visualising water vapour condensation in cracked concrete with dynamic neutron radiography. *Mater. Lett.* **283**, 1–4 (2021).
141. Pimienta, L. *et al.* Evolution in Seismic Properties During Low and Intermediate Water Saturation: Competing Mechanisms During Water Imbibition? *Geophys. Res. Lett.* **46**, 4581–4590 (2019).
142. Payan, C., Ulrich, T. J., Le Bas, P. Y., Saleh, T. & Guimaraes, M. Quantitative linear and nonlinear resonance inspection techniques and analysis for material characterization: Application to concrete thermal damage. *J. Acoust. Soc. Am.* **136**, 537–546 (2014).
143. Haupert, S. *et al.* High-accuracy acoustic detection of nonclassical component of material nonlinearity. *J. Acoust. Soc. Am.* **130**, 2654–61 (2011).
144. Khatib, J. M., Herki, B. A. & Elkordi, A. *Characteristics of concrete containing EPS. Use of Recycled Plastics in Eco-efficient Concrete* (Elsevier Ltd, 2019). doi:10.1016/b978-0-08-102676-2.00007-4
145. Ma, G. *et al.* Physical, mineralogical, thermal, and mechanical properties of aerogel-incorporated concrete exposed to elevated temperatures. *Cem. Concr. Compos.* **140**, 105089 (2023).
146. Zhong, P. *et al.* Internal curing with superabsorbent polymers of different chemical structures. *Cem. Concr. Res.* **123**, (2019).

147. Boshoff, W. *et al.* The effect of superabsorbent polymers on the mitigation of plastic shrinkage cracking of conventional concrete, results of an inter-laboratory test by RILEM TC 260-RSC. *Mater. Struct. Constr.* **53**, (2020).
148. Bernard, E., Jenni, A., Toropovs, N. & Mäder, U. Percolation experiment across a 10-year-old interface between Opalinus Clay and Portland concrete. *Cem. Concr. Res.* **170**, (2023).

APPENDIX

Results of mercury intrusion porosimetry. Evolution of porosity due to hydration.

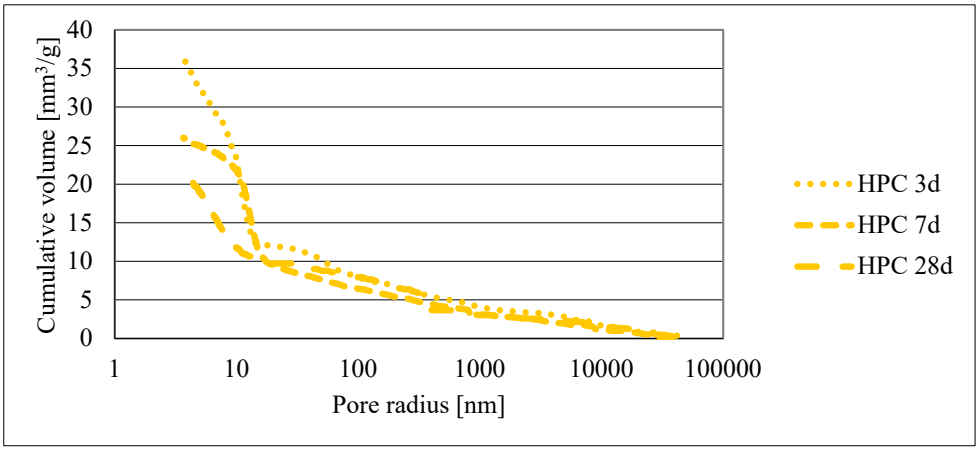

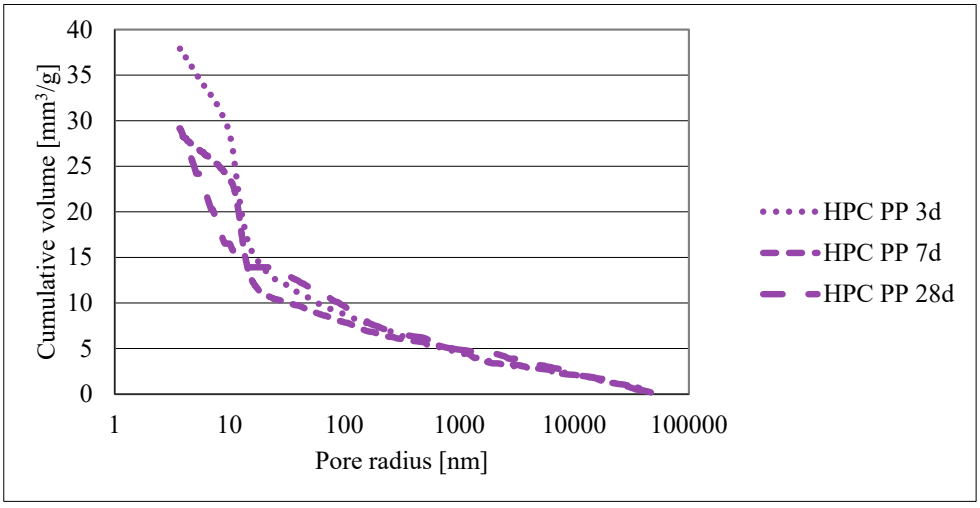

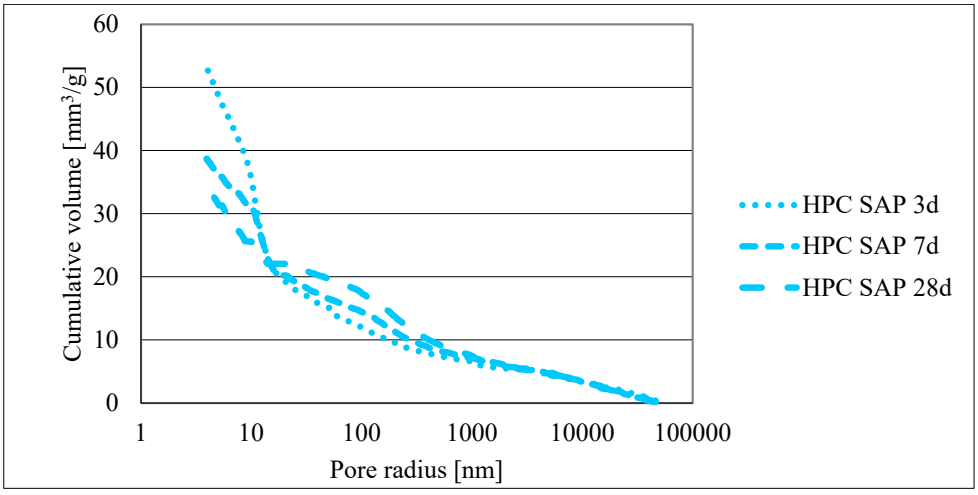

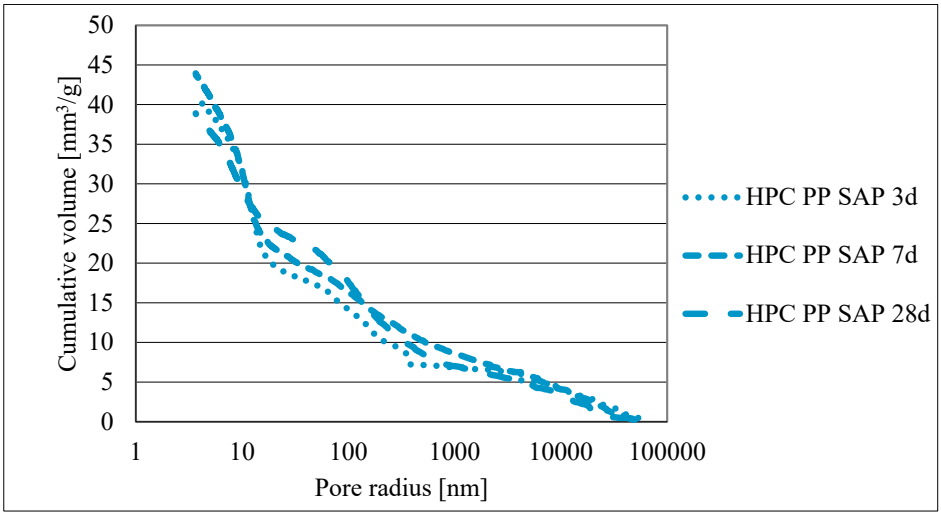
Cumulative volume [mm³/g]
50
45
40
35
30
25
20
15
10
5
0
1
10
100
1000
10000
100000
Pore radius [nm]
HPC PP SAP 3d
HPC PP SAP 7d
HPC PP SAP 28d

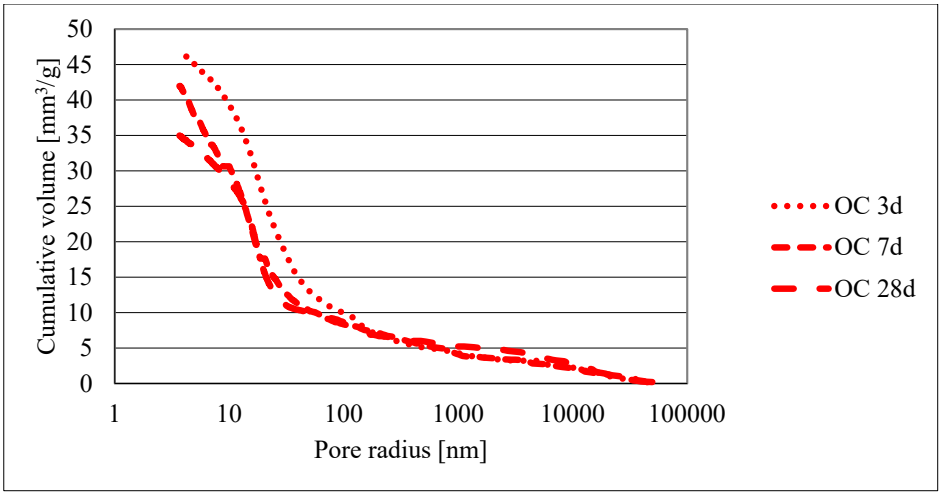
Cumulative volume [mm³/g]
50
45
40
35
30
25
20
15
10
5
0
1
10
100
1000
10000
100000
Pore radius [nm]
OC 3d
OC 7d
OC 28d

Results of mercury intrusion porosimetry. Evolution of porosity due to high temperatures.

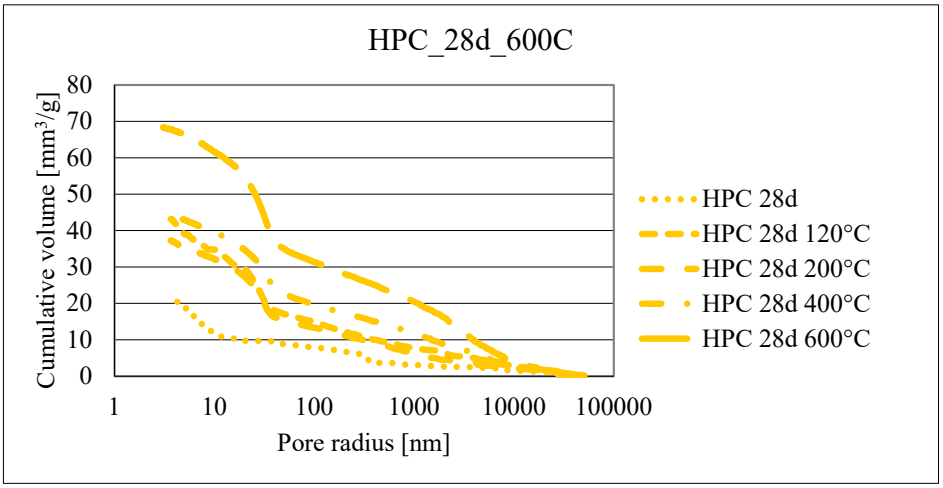

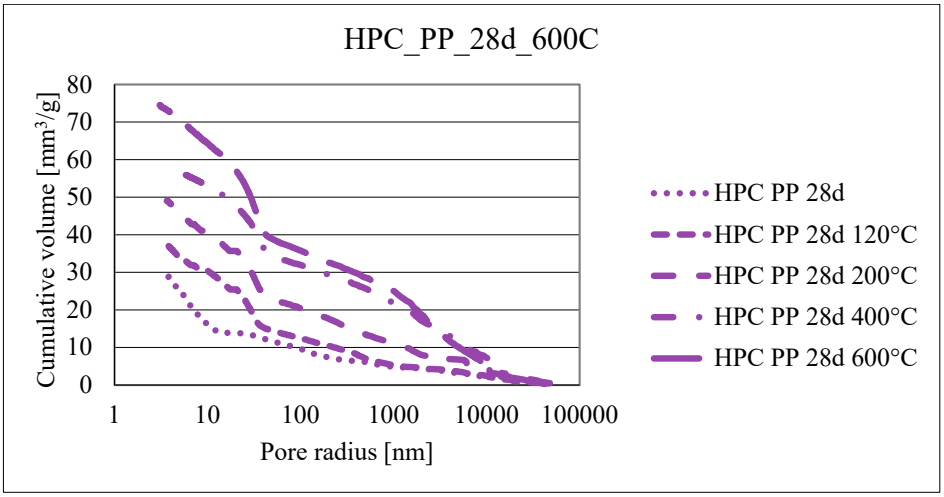

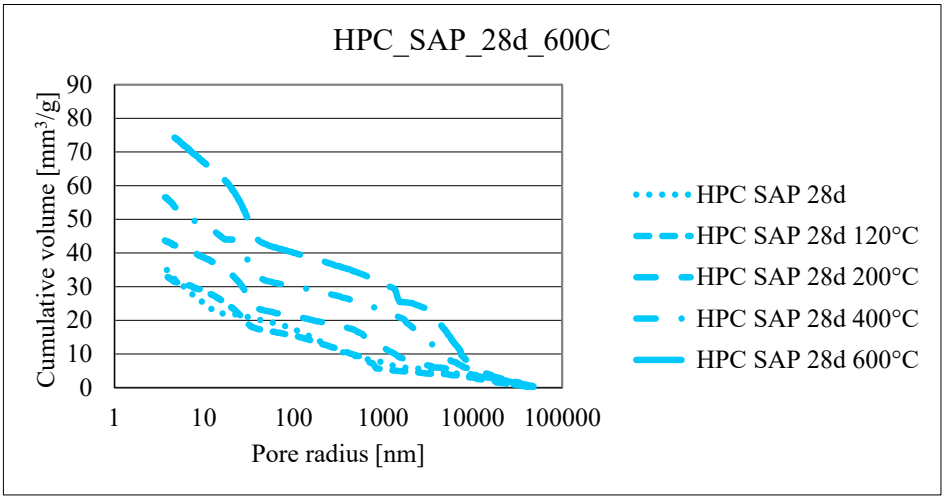

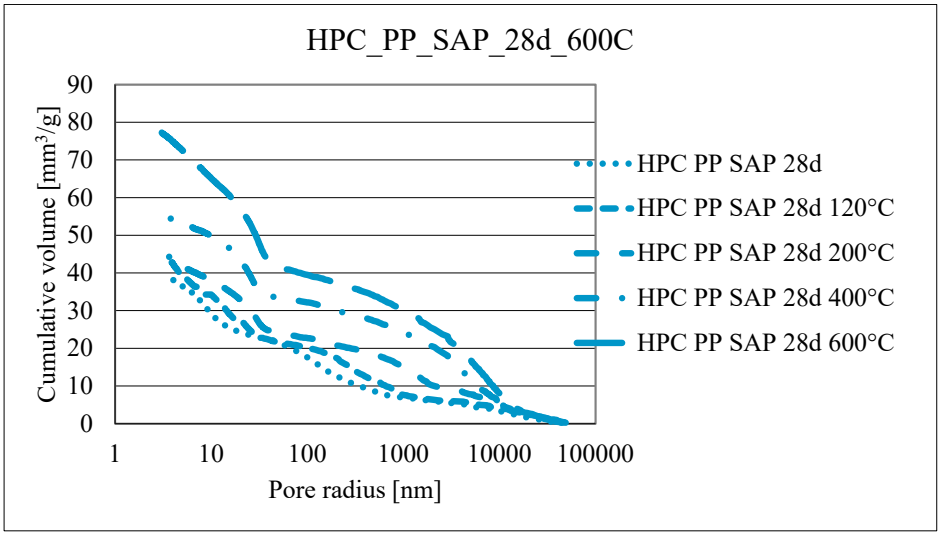
HPC_PP_SAP_28d_600C
Cumulative volume [mm³/g]
90
80
70
60
50
40
30
20
10
0
1
10
100
1000
10000
100000
Pore radius [nm]
HPC PP SAP 28d
HPC PP SAP 28d 120°C
HPC PP SAP 28d 200°C
HPC PP SAP 28d 400°C
HPC PP SAP 28d 600°C

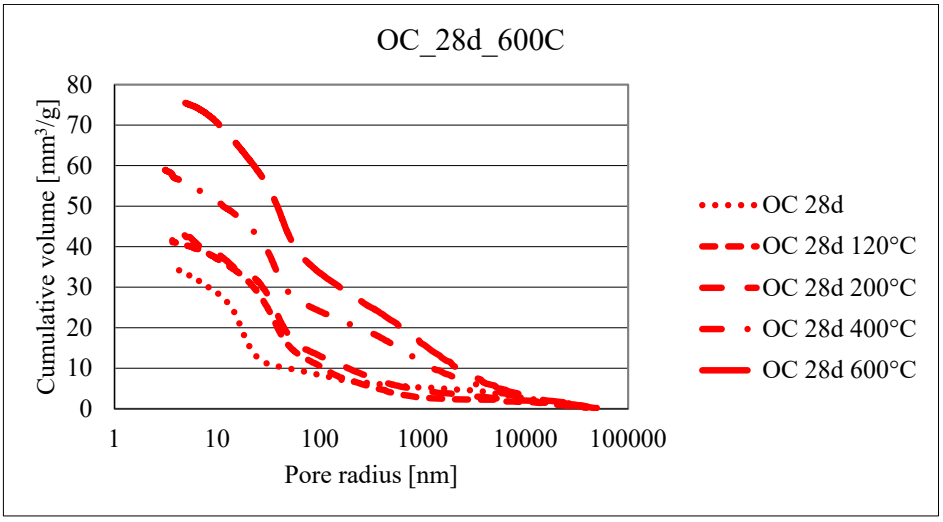
OC_28d_600C
Cumulative volume [mm³/g]
80
70
60
50
40
30
20
10
0
1
10
100
1000
10000
100000
Pore radius [nm]
OC 28d
OC 28d 120°C
OC 28d 200°C
OC 28d 400°C
OC 28d 600°C

Nikolajs Toropovs was born in 1986 in Riga. He received a Bachelor's degree in Construction Science (2007) and a Master's degree in Civil Engineering (2012) from Riga Technical University. During his studies, he worked at the Faculty of Civil Engineering of RTU. Since 2016, he has been a researcher at the Swiss Federal Laboratories for Materials Science and Technology. In 2025, he received the Swiss Building Award.